Measurement of $Z \to ee$ transverse momentum distribution in proton-proton collisions at $\sqrt{s} = 7$ TeV in the ATLAS detector

by

Hao Liu

A dissertation submitted in partial fulfillment
of the requirements for the degree of
Doctor of Philosophy
(Physics)
in The University of Michigan
2011

Doctoral Committee:

Professor Jianming Qian, Chair
Professor Homer A. Neal
Professor Rudolf P. Thun
Professor Virginia R. Young
Associate Professor Aaron Thomas Pierce

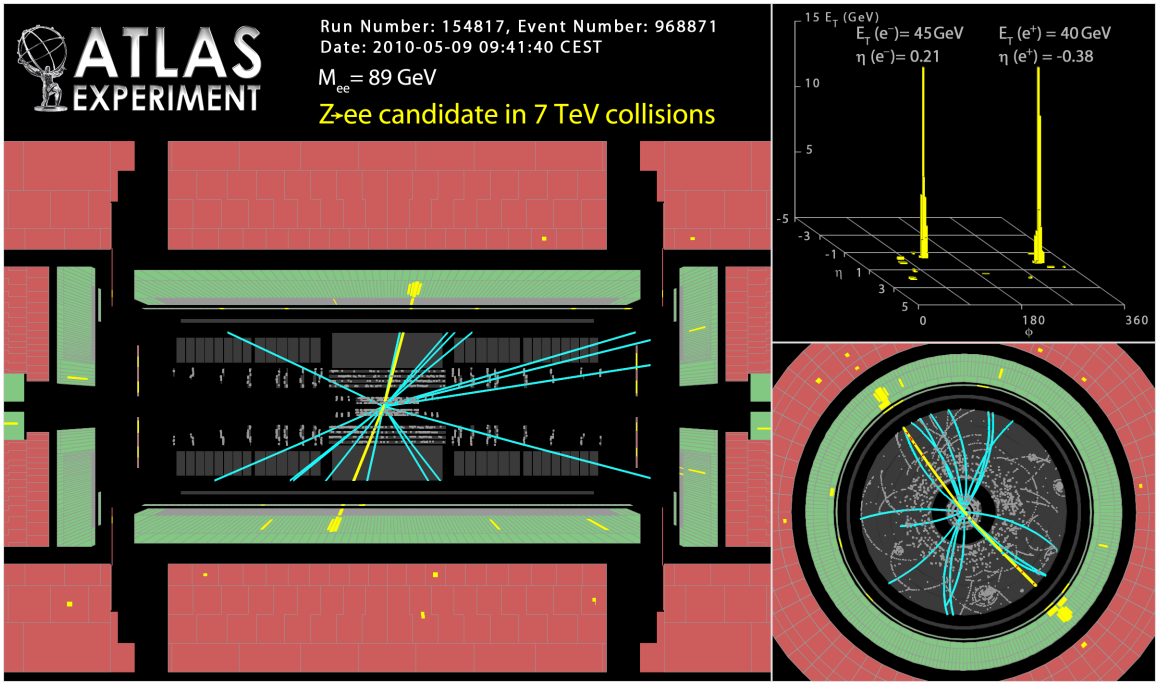

First candidate for $Z \to ee$ decay produced by the proton-proton collision at $\sqrt{s} = 7$ TeV, collected by the ATLAS detector on 9 May 2010.

For all the people

ACKNOWLEDGEMENTS

Thanks to the people who made this dissertation possible.

CONTENTS

LIST OF FIGURES

Figure

LIST OF TABLES

Table

LIST OF ABBREVIATIONS

pQCD Perturbative Quantum ChromoDynamics

QCD Quantum ChromoDynamics

MC Monte Carlo

QED Quantum Electroweak Dynamics

NLL Next-to-Leading Logarithm

NNLO Next-to-Next-to-Leading Order

NLO Next-to-Leading Order

LO Leading Order

LHC Large Hadron Collider

ATLAS A Toroid LHC ApparatuS

DY Drell-Yan

PDF Parton Distribution Function

LEP Large Electron-Positron Collider

IP interaction point

ID Inner Detector

SCT Semi-Conductor Tracker

TRT Transition Radiation Tracker

BCM Beam Conditions Monitor

HEC Hadronic Endcap Calorimeter

FCal Forward Calorimeter

TileCal Tile Calorimeter

MDT Monitored Drift Tubes

RPC Resistive Plate Chambers

TGC Thin Gap Chambers

CSC Cathode Strip Chambers

L1 Level One

L2 Level Two

EF Event Filter

HLT High Level Trigger

ROI Region Of Interest

GRL Good Runs List

LUCID LUminosity measurement using a Cherenkov Integrating Detector

VEV Vaccum Expectation Value

OTX Optical Transmitter

FEB Front-End Board

ABSTRACT

Measurement of $Z \to ee$ transverse momentum distribution in proton-proton collisions at $\sqrt{s} = 7$ TeV in the ATLAS detector

by

Hao Liu

Chair: Jianming Qian

The normalized distribution of $Z/\gamma^* \to ee$ transverse momentum[1], $\frac{1}{\sigma}\frac{\mathrm{d}\sigma}{\mathrm{d}p_T^Z}$, is measured in proton-proton collisions at center-of-mass energy $\sqrt{s} = 7$ TeV with the A Toroid LHC ApparatuS (ATLAS) detector. The results are based on a dataset corresponding to an integrated luminosity of 35 pb^{-1} collected in 2010. The major background to $Z \to ee$ is from Quantum ChromoDynamics (QCD) processes and is studied by data-driven methods. A bin-by-bin unfolding method is used to correct for the detector acceptance and efficiency which is cross-checked with a regularized matrix unfolding method. A complete analysis of both theoretical and experimental uncertainties is also presented. The theoretical uncertainties arise from Quantum Electroweak Dynamics (QED) and QCD corrections, which are estimated using Monte Carlo (MC) simulations. The experimental uncertainties arise from multiple sources with dominant ones being the electron identification, electron energy scale, and energy resolution. The measurement is compared to predictions of various MC event generators. The prediction of re-summed QCD combined with fixed order Perturbative

[1]In the following, Z stands for Z/γ^*, i.e. Z including small γ^* and $\gamma^* - Z$ interference contributions.

Quantum ChromoDynamics (pQCD) calculations is found to be in good agreement with data.

CHAPTER I

Introduction

At the Large Hadron Collider (LHC), the Z boson, one of the propagators of the electroweak interaction with the mass $m_Z = 91.2$ GeV, is produced abundantly in proton-proton collisions at $\sqrt{s} = 7$ TeV at an approximate rate of 1000 Z per pb^{-1} integrated luminosity. Of these, 3.36% decay to an electron-positron pair. The large dataset of Z bosons in the electron decay channel enables precise measurements of the transverse momentum spectrum, p_T^Z . In the high transverse momentum regime with p_T^Z values larger than half of the mass of the Z boson, $m_Z/2$, the production is dominated by the radiation of additional hard partons prior to the Z boson decay and can be calculated by pQCD theory. However, in the low transverse momentum regime with p_T^Z values less than 5 GeV, the production is dominated by soft real and virtual gluon emissions. The calculation is not perturbative, and a soft-gluon resummation is mandated [4, 5].

The Z boson transverse momentum study allows the validation of both resummed and perturbative QCD calculations. A precise knowledge of the Z boson transverse momentum is also crucial for precision electroweak measurements, such as the measurement of the W boson mass [6].

This thesis presents a measurement of the normalized $Z \to ee$ transverse momentum (p_T^Z) distribution in proton-proton collisions at $\sqrt{s} = 7$ TeV with a dataset cor-

responding to an integrated luminosity of 35 pb^{-1} collected by the ATLAS detector. The normalized transverse momentum distribution is independent of the luminosity and many systematic uncertainties cancel.

The structure of the thesis is as follows: Chapter 2 is a brief review of the Standard Model and Z boson production in proton-proton collisions; Chapter 3 gives an overview of the LHC machine and describes the ATLAS detector in detail; Chapter 4 summarizes algorithms of electron reconstruction, identification and trigger and measurements of the electron efficiency and energy in 2010; Chapter 5 presents the collected data, Monte Carlo simulations and distributions of the di-electron transverse momentum (p_T^{ee}); Chapter 6 studies backgrounds of the $Z \to ee$ process after the final selection; Chapter 7 presents strategies and results of the extraction of p_T^Z from p_T^{ee}; Chapter 8 evaluates potential uncertainties of p_T^Z measurements; Chapter 9 is the summary of measurements of p_T^Z.

CHAPTER II

Standard Model

The Standard Model of particle physics has been very successful in describing fundamental particles and their interactions. This chapter introduces the Standard Model and Z boson production in proton-proton collisions. Section 2.1 begins with the summary of particles and interactions in the Standard Model. Section 2.2 starts with the electromagnetic theory which is the first complete theory of the interaction of electric charges. Then theories of electroweak, Higgs mechanism and strong interactions are discussed in Section 2.3, 2.4 and 2.5, respectively. Section 2.6 presents the Z boson production in the LHC. Section 2.7 summarizes the Monte Carlo generators used in this thesis to study p_T^Z .

2.1 Particles and Interactions in the Standard Model

There are four fundamental interactions in nature: gravitational, electromagnetic, weak, and the strong interactions. The latter three interactions are successfully described by the Standard Model. The electromagnetic and weak interactions are unified into an electroweak theory in the Standard Model.

There are two kinds of fundamental particles in the Standard Model: fermions and bosons. Fermions are spin 1/2 particles and obey Fermi-Dirac statistics. They are the constituents of matter. Bosons have integer spins and obey Bose-Einstein

statistics. They are responsible for mediating forces between particles. The quantum field theory is used to formulates the behavior of fermions and bosons. Matter and antimatter are mostly treated equally within the Standard Model except for some rare particle decays [7].

The fermions in the Standard Model are categorized as leptons and quarks based on whether they participate in the strong interaction. Leptons and quarks are grouped into three generations or families. Leptons only respond to the electroweak interaction, with the spin of 1/2 and the charge of 0[1] or -1. Quarks have both electroweak and strong interactions with the spin of 1/2 and the charge of $-1/3$ or $2/3$. The nature of the strong force is that the quarks are confined to form hadrons instead of isolated particles. There are two categories of hadrons according to the number of their constituent quarks: mesons ($q\bar{q}$, where q represents a quark and $\bar{q}$ an anti-quark) and baryons (qqq or $\bar{q}\bar{q}\bar{q}$). In the QCD theory, each quark carries three different colors. However, the leptons and hadrons are colorless. Fermions can also be categorized into left-handed and right-handed components according to their helicities. The helicity of a particle is the direction of its spin relative to its momentum; particles with spin in the same direction as their momentum are called right-handed, and otherwise they are called left-handed. All the fermions have both left-handed and right-handed partners except for neutrinos. The right-handed neutrinos are not yet discovered so far. Each fermion has an anti-particle partner which has the same quantum numbers except for the opposite charge.

There are three types of bosons with the spin of 1 in the Standard Model, corresponding to three different interactions. The photon is the massless mediator for the electromagnetic interaction. W^+, W^- and Z bosons are massive mediators in the weak interaction with the charge of $+1$, -1 and 0, respectively. The 8 massless gluons are mediators of the strong interaction which carry different colors and form an octet

[1]Without specification, the charge unit in this thesis is e.

of vector bosons.

The quantum numbers of fermions and bosons are summarized in Table 2.1.

Fermions				Spin	Charge
Leptons	ν_e	ν_μ	ν_τ	1/2	0
	e	μ	τ	1/2	-1
Quarks	u	c	t	1/2	2/3
	d	s	b	1/2	-1/3
Bosons				Spin	Charge
Electromagnetic	γ			1	0
Weak	$W^{\pm}$, Z			1	$\pm 1, 0$
Strong	8 gluons			1	0

Table 2.1: The quantum numbers of leptons, quarks and mediating bosons in the Standard Model.

In the Standard Model, the particle interaction equations are obtained from the gauge invariance principle: the Lagrangian must be invariant under a local (gauge) transformation from the symmetry group

$$SU(3)_C \otimes SU(2)_L \otimes U(1)_Y. \tag{2.1}$$

The $SU(2)_L \otimes U(1)_Y$ group is the symmetry generator for both electromagnetic and weak interaction which are unified as the electroweak interaction in the Glashow-Salam-Weinberg model [8]. The conserved quantum numbers in the electroweak interaction are the isospin (I_3) and hypercharge (Y). Their combinations lead to electromagnetic charges (q). Only left-handed (L) fermions attend the weak interaction. The $SU(3)_C$ is the symmetry generator for the strong interaction. Its conserved quantum number is the color charge (C) which is equivalent to the electromagnetic charge.

2.2 The Electromagnetic Interaction

The electromagnetic theory describes interactions of fermion and photon fields. The Lagrangian of a spin 1/2 fermion field ψ can be written with a kinematic term and a mass term

$$\mathcal{L}_D = i\bar{\psi}\gamma^\mu\partial_\mu\psi - m\bar{\psi}\psi \tag{2.2}$$

where m is the fermion mass, γ^μ is the Dirac gamma matrices [8] and $\psi\bar{\psi}$ is the spinor field for the fermion

$$\psi = \begin{pmatrix} \psi_R \\ \psi_L \end{pmatrix}. \tag{2.3}$$

The Lagrangian term for the photon field A_μ is

$$\mathcal{L}_\gamma = -\frac{1}{4}F^{\mu\nu}F_{\mu\nu} \tag{2.4}$$

where the $F_{\mu\nu} = \partial_\mu A_\nu - \partial_\nu A_\mu$ is the tensor field. Thus, the free Lagrangian for a fermion and photon field is

$$\mathcal{L}_D + \mathcal{L}_\gamma = i\bar{\psi}\gamma^\mu\partial_\mu\psi - m\bar{\psi}\psi - \frac{1}{4}F^{\mu\nu}F_{\mu\nu}. \tag{2.5}$$

Equation 2.5 has no coupling between the fermion field ψ and photon field A_μ. To obtain the missing interaction term, local gauge invariance is imposed, which requires the Lagrangian to be invariant under the transformation

$$\psi \to \psi' = e^{iq\theta(x)}\psi \tag{2.6}$$

where $\theta(x)$ is an arbitrary space-time (x) dependent function. For $0 \leq \theta < 2\pi$, transformations of $U = e^{iq\theta(x)}$ form the $U(1)$ symmetry group. So the electromagnetic

theory is a theory with $U(1)$ symmetry.

To satisfy local gauge invariance, the derivative operator can be redefined as

$$D_\mu = \partial_\mu + iqA_\mu \tag{2.7}$$

where q is the electromagnetic charge of the fermion, which can be interpreted as the strength of electromagnetic coupling; D_μ is named as the convariant derivative operator. Substituting the usual derivative operator by the convariant derivative, the electromagnetic Lagrangian is

$$\mathcal{L}_{\text{QED}} = i\bar{\psi}\gamma^\mu\partial_\mu\psi - m\bar{\psi}\psi - \frac{1}{4}F^{\mu\nu}F_{\mu\nu} - q\bar{\psi}\gamma^\mu A_\mu\psi. \tag{2.8}$$

The fourth term of the electromagnetic Lagrangian represents the electromagnetic interaction between the fermion and photon fields

$$\mathcal{L}_{\text{QED,int}} = -q\bar{\psi}\gamma^\mu A_\mu\psi \equiv -J^\mu A_\mu \tag{2.9}$$

where J^μ is the charge current, which is the probability of the particle current multiplied by its charge.

2.3 The Electroweak Interaction

The symmetry group of electroweak interactions is $SU(2)_L \otimes U(1)_Y$, in which only left-handed fermions are transformed under the $SU(2)$ symmetry and both left- and right-handed fermions are transformed under the $U(1)_Y$ symmetry. The eigenvectors of the $SU(2)_L$ and $U(1)_Y$ symmetries are re-combined into the eigenvectors of the weak and electromagnetic interactions. Therefore, the gauge fields are not the physical fields in the electroweak theory.

The $SU(2)_L$ symmetry group is generated by the Pauli matrices [8]. The third

eigenvalue of three Pauli matrices is used as one quantum number in the electroweak theory, I_3. In each family, there are two left-handed weak-isospin doublets, one for leptons and the other for quarks. They are

$$\begin{pmatrix} +1/2 \\ -1/2 \end{pmatrix}_{I_3} : \begin{pmatrix} \nu_e \\ e^- \end{pmatrix}_L, \begin{pmatrix} \nu_\mu \\ \mu^- \end{pmatrix}_L, \begin{pmatrix} \nu_\tau \\ \tau^- \end{pmatrix}_L, \begin{pmatrix} u \\ d \end{pmatrix}_L, \begin{pmatrix} c \\ s \end{pmatrix}_L, \begin{pmatrix} t \\ b \end{pmatrix}_L . \tag{2.10}$$

The right-handed neutrinos are not discovered so far, so the symmetry of parity is broken in electroweak interactions [8].

Similar to $U(1)$ symmetry, the doublet will be transformed under the local $SU(2)_L$ gauge as

$$\begin{pmatrix} \nu_e \\ e^- \end{pmatrix}_L \rightarrow \begin{pmatrix} \nu_e \\ e^- \end{pmatrix}'_L = e^{\frac{-i}{2}\vec{\alpha}(x)\cdot\vec{\tau}} \begin{pmatrix} \nu_e \\ e^- \end{pmatrix}_L \tag{2.11}$$

where e^- and ν_e are field functions for the electron and corresponding neutrino; L indicates the fermion is left-handed; $\vec{\tau}$ is the vector of Pauli matrices; $\vec{\alpha}(x)$ is a real vector which depends on space-time x.

Similar to Equation 2.6, the field function ψ of a left-handed or right-handed fermion is transformed under the local $U(1)$ gauge. Similarly, the quantum number of the $U(1)_Y$ symmetry is named as the hypercharge Y. The hypercharge is different for the left-handed fermion (Y_L) and its right-handed partner (Y_R).

$SU(2)_L \otimes U(1)_Y$ symmetry requires the presence of 4 gauge fields: 3 gauge fields from the $SU(2)_L$ doublet interaction and 1 gauge field from the $U(1)_Y$ singlet interaction. Similar to the electromagnetic theory, the covariant derivative operator is used in the electroweak Lagrangian

$$D_\mu = \partial_\mu + ig_2\frac{\vec{\tau}}{2}\cdot\vec{W}_\mu + ig_1\frac{Y}{2}B_\mu \tag{2.12}$$

where $\vec{W}_\mu = (W_1, W_2, W_3)_\mu$ is the gauge field with three components for the $SU(2)_L$ symmetry, B_μ is the gauge field for the $U(1)_Y$ symmetry, g_1 and g_2 are parameters of the interaction strength for $SU(2)_L$ and $U(1)_Y$ transformations.

After substituting the usual derivative by the covariant derivative and omitting the mass term, which will be discussed in the next section, the Lagrangian for the fermion and boson fields are

$$\mathcal{L}_{\text{fermion}} = \sum_f i\bar{\psi}\gamma^\mu D_\mu \psi, \tag{2.13}$$

$$\mathcal{L}_{\text{boson}} = -\frac{1}{4} W_i^{\mu\nu} W^i_{\mu\nu} - \frac{1}{4} B^{\mu\nu} B_{\mu\nu}. \tag{2.14}$$

Therefore, the electroweak Lagrangian is

$$\mathcal{L}_{\text{EW}} = \mathcal{L}_{\text{fermion}} + \mathcal{L}_{\text{boson}} = \sum_f i\bar{\psi}\gamma^\mu D_\mu \psi - \frac{1}{4} W_i^{\mu\nu} W^i_{\mu\nu} - \frac{1}{4} B^{\mu\nu} B_{\mu\nu}. \tag{2.15}$$

After expanding Equation 2.15 and comparing it to dynamic terms of the electromagnetic Lagrangian (Equation 2.8), the four physical fields for the $W^\pm$, Z bosons and the photon are defined by recombining the gauge fields $\vec{W}$ and B as

$$W^\pm_\mu = \frac{1}{\sqrt{2}}(W^1_\mu \mp W^2_\mu), \tag{2.16}$$

$$Z_\mu = \cos\theta_w W^3_\mu - \sin\theta_w B_\mu, \tag{2.17}$$

$$A_\mu = \cos\theta_w B_\mu + \sin\theta_w W^3_\mu. \tag{2.18}$$

In the electroweak theory, the Weinberg angle θ_w is defined as

$$\sin\theta_w = \frac{g_1}{\sqrt{g_2^2 + g_1^2}}. \tag{2.19}$$

Particle	Isospin (I_3)	Hypercharge (Y)
Fermion		
$(\nu_{e^-}, e^-)_L$	(1/2, -1/2)	(-1, -1)
e_R^-	0	-2
$(u, d)_L$	(1/2, -1/2)	(1/3, 1/3)
$(u, d)_R$	(0, 0)	(4/3, -2/3)
Boson		
(W^+, W^-)	(1, -1)	(0, 0)
Z	0	0
γ	0	0

Table 2.2: Summary of the weak isospin and the hypercharge of fermions and bosons.

The g_1 and g_2 can be written in terms of θ_w and unit of the electromagnetic charge e as

$$g_1 = \frac{e}{\cos\theta_w}, \tag{2.20}$$

$$g_2 = \frac{e}{\sin\theta_w}. \tag{2.21}$$

Therefore, the electromagnetic charge (q) of a fermion can be defined by the combination of its weak isospin (I_3) and hypercharge (Y)

$$q = I_3 + Y/2. \tag{2.22}$$

The weak isospin and the hypercharge of fermions and bosons are summarized in Table 2.2

2.4 The Higgs Mechanism and Symmetry Breaking

One more degree of complexity is needed in the electroweak theory, otherwise the fermions and bosons are massless. Therefore, a Higgs field is introduced as an $SU(2)$ doublet

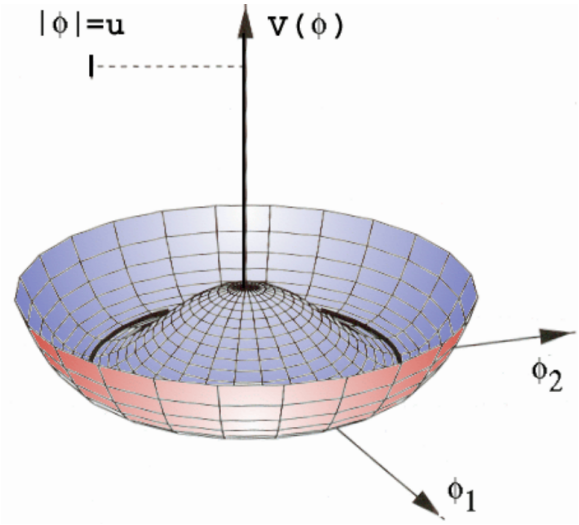

Figure 2.1: The Higgs potential $V(\phi) = \mu^2\phi^\dagger\phi + \lambda(\phi^\dagger\phi)^2$.

$$\phi = \begin{pmatrix} \phi^+ \\ \phi^0 \end{pmatrix} \tag{2.23}$$

where ϕ^+ and ϕ^0 are both complex fields

$$\phi^+ = \frac{\phi_1 + i\phi_2}{\sqrt{2}}, \tag{2.24}$$

$$\phi^0 = \frac{\phi_3 + i\phi_4}{\sqrt{2}}. \tag{2.25}$$

The Higgs field has a potential [8]

$$V(\phi) = \mu^2\phi^\dagger\phi + \lambda(\phi^\dagger\phi)^2 \tag{2.26}$$

which has a shape of the Mexican hat as shown in Figure 2.1.

Combining the potential and the kinematic term, the Higgs field Lagrangian is

$$\mathcal{L} = i(\partial_\mu\phi)^\dagger(\partial^\mu\phi) - \mu^2\phi^\dagger\phi - \lambda(\phi^\dagger\phi)^2. \tag{2.27}$$

The potential $V(\phi)$ has a minimum for $\mu^2 < 0$ at

$$\phi^\dagger\phi = \frac{-\mu^2}{2\lambda} = v^2/2 \tag{2.28}$$

where v is the Vaccum Expectation Value (VEV) with $v \approx 246$ GeV [8]. In the $SU(2)$ space, the Higgs field can be expanded around the minimum, $\phi = \phi_0 + \Delta\phi$. The appropriate choice is called vacuum ϕ_0,

$$\phi_0 = \frac{1}{\sqrt{2}} \begin{pmatrix} 0 \\ v \end{pmatrix} \rightarrow \phi = \frac{1}{\sqrt{2}} \begin{pmatrix} 0 \\ v + H \end{pmatrix}. \tag{2.29}$$

Note that the vacuum has no charge, $q = 0$ and the electromagnetic charge assignment of Equation 2.23 corresponds to $Y = 1$. So $I_3 = -1/2 = (q - Y/2)$ for the Higgs field ϕ. The Lagrangian of Equation 2.27 allows the Higgs boson decays into a pair of W^+ and W^- in which neither the weak isospin nor hypercharge is conserved, otherwise the Higgs boson should have $I_3 = Y = 0$. Therefore, both $SU(2)_L$ and $U(1)_Y$ symmetries are broken. However, the Lagrangian is invariant under a electromagnetic transformation

$$\phi \rightarrow \phi' = e^{i\alpha(x)q}\phi = \phi \tag{2.30}$$

which means the Higgs field has a $U'(1)$ symmetry corresponding to the electromagnetic charge conservation.

Substituting ϕ by Equation 2.29 and the ∂_μ by the convariant derivative D_μ of Equation 2.12 in Equation 2.27, the mass terms for bosons are

$$\frac{1}{8}v^2 g_2^2 \left((W_\mu^1)^2 + (W_\mu^2)^2 + \frac{1}{8}(g_1 B_\mu - g_2 W_\mu^3)^2 \right). \tag{2.31}$$

The first term corresponds to the W boson mass term

$$\left(\frac{1}{2}vg_2\right)^2 W_\mu^+ W_\mu^- \Rightarrow M_W = \frac{vg_2}{2} \tag{2.32}$$

and the second term to the mass term of the Z boson after comparing to Equation 2.18

$$M_Z = \frac{1}{2}v\sqrt{g_1^2 + g_2^2}. \tag{2.33}$$

To get the fermion masses, one adds the Yukawa coupling terms *e.g.* for leptons and quarks in the first family,

$$\mathcal{L}_{\text{int,lepton}} = g_e(\bar{L}\phi e_R^- + \phi^\dagger \bar{e}_R^- L), \tag{2.34}$$

$$\mathcal{L}_{\text{int,quark}} = g_d \bar{Q}_L \phi d_R + g_u \bar{Q}_L \phi_c u_R + \text{h.c.} \tag{2.35}$$

where $L = \begin{pmatrix} \nu_e \\ e^- \end{pmatrix}$, $Q_L = \begin{pmatrix} u_L \\ d_L \end{pmatrix}$, g_e, g_u, g_d are interaction strengths between fermions and the Higgs field, $\phi_c = \begin{pmatrix} -\frac{v+H}{\sqrt{2}} \\ 0 \end{pmatrix}$ arisen from the right-handed u quark. g_e, g_u, g_d are free parameters in the Standard Model, therefore fermion masses m_e, m_u and m_d determined from them are free parameters as well.

2.5 The Strong Interaction

The strong interaction only exists between quarks and gluons with the symmetry group $SU(3)$. The quantum number from the $SU(3)$ symmetry is the "color", which is a new degree of freedom and conserved under $SU(3)$ transformations similar to the isospin and hypercharge in the electroweak theory. There are 3 eigenstates in the strong interaction, usually named as "red"(R), "green"(G) and "blue"(B). The realistic quantum field theory for the strong interaction is Quantum Chromodynamics.

After imposing the color index $\alpha = 1, 2, 3$ (B,R,G) in Equation 2.2, the Lagrangian term for the free quark takes the form

$$\mathcal{L}_{\text{quark}} = i\bar{\psi}_\alpha \gamma^\mu D_\mu \psi_\alpha - m\bar{\psi}_\alpha \psi_\alpha. \tag{2.36}$$

The $SU(3)$ symmetry requires the Lagrangian to be invariant under the transformation

$$\psi_\alpha \to \psi'_\alpha = e^{-\frac{i}{2} g_3 \theta_a(x) \lambda_a} \psi_\alpha \tag{2.37}$$

where g_3 is related to the coupling constant of the strong interaction

$$g_3 = \sqrt{4\pi\alpha_s}. \tag{2.38}$$

λ_a are the eight generators of $SU(3)$, known as Gell Mann matrices [8] with structure constants f_{abc}. The $SU(3)$ group commutation rules are

$$\left[\frac{\lambda_a}{2}, \frac{\lambda_b}{2}\right] = i f_{abc} \frac{\lambda_c}{2}. \tag{2.39}$$

The $SU(3)$ convariant derivative takes the form

$$D_\mu = \partial_\mu + i\frac{g_3}{2}\lambda_a G^a_\mu \tag{2.40}$$

where G^a_μ are the 8 gluon fields. So the Lagrangian terms for quarks and gluons are

$$\mathcal{L}_{\text{QCD}} = i\bar{\psi}_\alpha \gamma^\mu \partial_\mu \psi_\alpha - m\bar{\psi}_\alpha \psi_\alpha - i g_3 \bar{\psi}_\alpha \gamma^\mu \lambda_a \psi^\alpha G^a_\mu - \frac{1}{4} G^{\mu\nu}_a G^a_{\mu\nu}, \tag{2.41}$$

in which the electroweak and Higgs interaction terms are ignored and the gluon tensor fields $G^{\mu\nu}_a$ defined as

$$G^a_{\mu\nu} = \partial_\mu G^a_\nu - \partial_\nu G^a_\mu - g_3 f^{abc} G_{\mu,b} G_{\nu,c}. \tag{2.42}$$

The third term of Equation 2.42 means that the gluon fields can have a self-interaction. This is due to the non-Abelian character of the $SU(3)$ symmetry group. The gluon self-interaction leads to one unique behavior of the strong interaction, that is, no free color multiplet is observed and all stable states can only be color singlets. This property is known as color confinement. In order to separate the color-charged quarks in a hadron, one had to impose such a large energy that gluon fields would get enough energy to produce quark-antiquark pairs in the intervening space. Thus, all the quarks and gluons are confined to exist as the constituents of mesons and baryons.

On the other hand, all the experiments show that in a sufficient high energy process, the quarks inside a hadron behave as free particles. This property is known as asymptotic freedom and it can be well explained by the renormalization of QCD theory [9]. The renormalization theory takes into account the higher order corrections in addition to the leading order (tree level) process. This happens because in nature particles can not be separated from interactions even when they are propagating in the "vacuum". The physics Lagrangian always contains an interaction term. Thus, a particle at any space-time point can produce virtual coupling that modifies the field around the particle itself.

In the Abelian theory of QED, higher energy will cause the two particles closer so that one can better experience the charge of the other. So the electromagnetic coupling constant α increases as the collision energy. In the non-Abelian QCD theory, a similar effect occurs, but the gluon self-coupling reverses the effect. Thus, the strong coupling constant α_s decreases as the collision energy.

The relation between α_s and energy scale μ is given by

$$\mu\frac{\partial\alpha_s(\mu)}{\partial\mu} = -\frac{11-\frac{2}{3}n_f}{2\pi}\alpha_s^2(\mu) - \mathcal{O}(\alpha_s^3(\mu)) \tag{2.43}$$

where n_f is the number of quark flavors with the mass $m_q < \mu$. So far, there are 6

different quarks observed in the Standard Model, so the leading term in Equation 2.43 is always negative. At high energies, the small α_s makes it possible to apply perturbative calculations. On the other hand, at low energies such as the meson and baryon states, the perturbative calculation is no longer valid. Instead, another theory called Lattice Field Theory [10] has been developed to study bound states.

2.6 The Drell-Yan Process

In high energy collisions, such as pp collisions at the Large Hadron Collider (LHC), quarks and antiquarks can produce plentiful Z/γ^* bosons composed with real Z bosons, off-shell photons and the interference between real Z and photons. The dominant production channel is the Drell-Yan (DY) process

$$q\bar{q} \to Z/\gamma^* \to f\bar{f}. \tag{2.44}$$

Although the proton is a matter particle, the Drell-Yan process is possible in pp collisions due to the parton "sea" in the proton, which consists of quarks, antiquarks and gluons, each typically carrying a small fraction of the proton's momentum and being created and destroyed in the strong interaction. The fraction x of the proton energy carried by the parton is called Bjorken scale [8]. The probability distribution of x is called Parton Distribution Function (PDF) denoted as $f(x, Q^2)$. PDFs depend on the square of the energy scale(Q); $xf(x, Q^2)$ increases as x decreases, which is shown in Figure 2.2.

If the colliding partons carry the fractions x_1 and x_2 of the proton momenta, then the invariant mass square of the colliding partons is

$$\hat{s} = x_1 x_2 s \tag{2.45}$$

where s is the square of the center-mass-energy of colliding proton beams. During

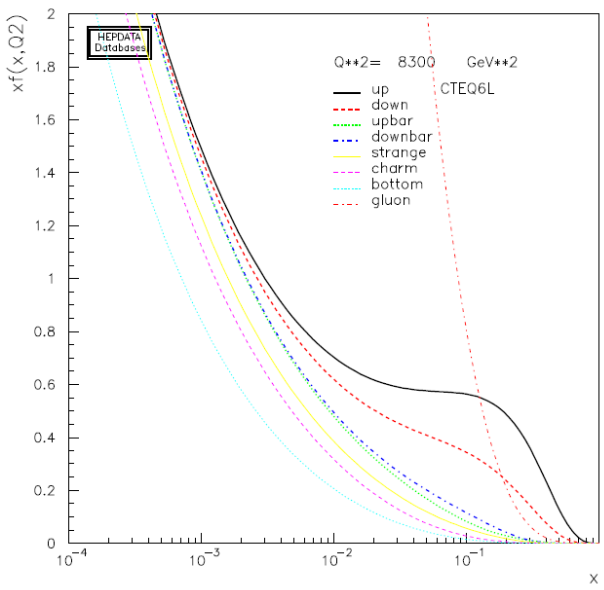

Figure 2.2: Parton density function as a function of Bjorken x with $Q^2 = m_Z^2$ from the CTEQ collaboration [1].

the year 2010 LHC operation, $\sqrt{s} = 7$ TeV. For on-shell Z production, $\sqrt{s} \approx m_Z$. So the x values for the Z boson production are very small. Consequently, the Z boson production rate is very high at the LHC.

The Z boson production is associated with soft gluon emissions, which give the Z boson transverse momentum. If there is a hard gluon or quark radiated in the Z boson production, an additional jet will be produced in the final state, which also passes a large transverse momentum to the Z boson. Figure 2.3(a) and 2.3(b) show the typical processes of $Z+0$ jet and $Z+1$ jet in the leptonic decay channel, respectively. Similarly, the Z boson production can also associate with more than one hard parton resulting in $Z + n$ jets events.

At the parton level, the Leading Order (LO) cross-section can be calculated using the electroweak theory without the QCD corrections since α_s is small at the large energy scale. The LO cross-section of the on-shell Z production [8] is

$$\hat{\sigma}_{q\bar{q}\to Z}(\hat{s}) = \frac{2\pi\sqrt{2}}{3} m_Z^2 G_F [(c_Z^{q_L})^2 + (c_Z^{q_R})^2] \delta(\hat{s} - m_Z^2) \tag{2.46}$$

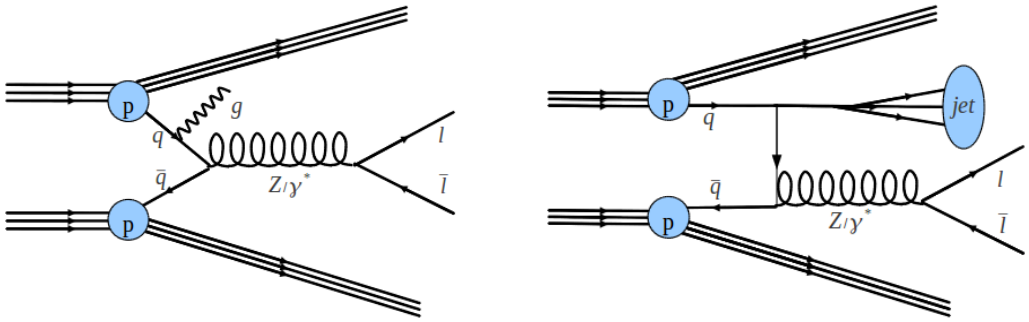

(a) (b)

Figure 2.3: Diagrams of (a) Z+0 jet and (b) Z+1 jet in proton-proton collisions. The Z boson decays to a pair of lepton and anti-lepton.

Particle	c_Z
ν_L	$\frac{1}{2}$
ℓ_L	$-\frac{1}{2} + \sin^2\theta_w$
u_L	$\frac{1}{2} - \frac{2}{3}\sin^2\theta_w$
d_L	$-\frac{1}{2} + \frac{1}{3}\sin^2\theta_w$
ℓ_R	$\sin^2\theta_w$
u_R	$-\frac{2}{3}\sin^2\theta_w$
d_R	$\frac{1}{3}\sin^2\theta_w$

Table 2.3: Couplings between fermions and Z bosons.

where the c_Z are couplings between fermions and Z bosons summarized in Table 2.3.

Note that in Equation 2.46 neither the decay width of the $Z(\Gamma_Z)$ nor any the photon terms is taken into account. The total Z production cross-section in pp collisions is calculated with the higher order corrections convolved with the relevant PDF set.

$$\sigma_{pp\to Z/\gamma^*} = \sum_q \int dx_1 dx_2 f_q(x_1, Q^2) f_{\bar{q}}(x_2, Q^2) + f_q(x_2, Q^2) f_{\bar{q}}(x_1, Q^2) \hat{\sigma}_{q\bar{q}\to Z}(x_1 x_2 s) \tag{2.47}$$

The contribution from γ^*(photon and $|\gamma Z|$ interference) is small under the resonance Z mass peak. Its contribution is estimated to be less than 2% [11] in the mass range (66, 116) GeV. However, it becomes important in the low mass region ($<$ 60

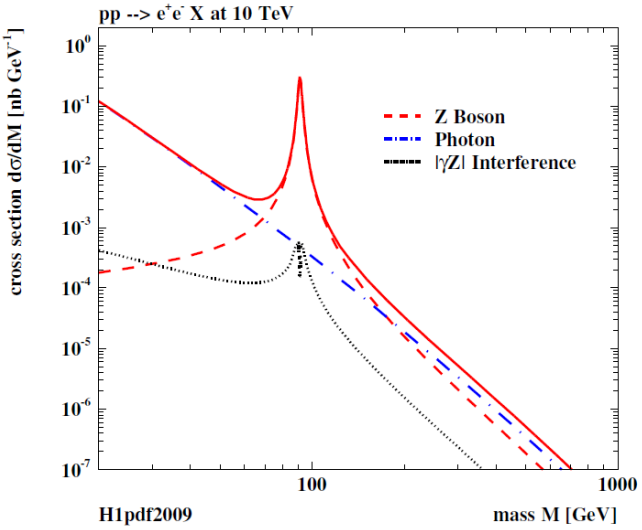

Figure 2.4: The invariant mass distributions of the Drell-Yan process at $\sqrt{s} = 10$ TeV [2]. In low and large mass regions, the production cross section is dominated by the pure photon contribution (dashed-dotted, blue curve). The real Z boson resonance is shown with dashed red curve. The $|\gamma Z|$ interference contribution (dotted, black) is shown in absolute. The sum of photon, Z and $|\gamma Z|$ contributions is shown as a solid red line.

GeV) and high mass range (> 200 GeV). Figure 2.4 shows the mass distributions of real Z, photon and $|\gamma Z|$ interference [12].

In Equation 2.47, the choice of Q^2 (or μ_F) has no physics origin, but rather is used for applying a perturbative QCD calculation for all orders. The dependence can be reduced by including more higher-order terms in the LO cross-section calculation of Equation 2.46. When performing higher order cross-section calculation, the strong coupling α_s must be determined. However α_s depends on the energy scale or renormalization scale μ (or μ_R) as shown in Equation 2.43. Usually the μ_F and μ_R are chosen to be m_Z^2 or s to calculate the Drell-Yan production cross-section. The variance of the cross-section due to the different choices of μ_F and μ_R is one of the systematic uncertainties.

Generator	Resummed	pQCD fixed order	PDF	Parton shower	Underlying events
Pythia	-	LO	MRST2007LO [22]	Pythia	Pythia
Alpgen	-	LO + N parton	CTEQ6L1 [23]	Herwig [24]	Jimmy [25]
Sherpa	-	LO + N parton	CTEQ6.6 [1]	Herwig	Jimmy
Mc@nlo	-	NLO	CTEQ6.6	Herwig	Jimmy
Powheg	-	NLO	CTEQ6.6	Herwig	Jimmy
Resbos	NLL	NLO	CTEQ6.6	-	-
Fewz	-	NNLO/NLO	MSTW2008 [22]	-	-

Table 2.4: Summary of Monte Carlo generators used in this thesis.

2.7 MC Generators

The Z boson production is simulated by Monte Carlo generators with different features. One feature is the highest order of the matrix element $\hat{\sigma}_{q\bar{q}\to Z}(\hat{s})$ with respect to the strong coupling constant α_s. In the resummed calculation, the matrix element is ordered by $\mathcal{O}(\log(\alpha_s))$ while in the fixed order pQCD calculation, it is ordered by $\mathcal{O}(\alpha_s)$.

Pythia [13] (Leading Order (LO)) and Mc@nlo [14, 15] (Next-to-Leading Order (NLO)) are two generators implemented in the ATLAS standard framework [16] with full simulation and reconstruction. Therefore, they are used as primary Monte Carlo samples simulating the $Z \to ee$ process. Pythia is used for central value calculations, while Mc@nlo is used for systematic studies. The final results are also compared to predictions from other generators: Alpgen [17], Sherpa [18], Powheg [19], Resbos [20] and Fewz [21]. Among these generators, only Resbos uses the resummed calculation up to the Next-to-Leading Logarithm (NLL) and only Fewz calculates the fixed order pQCD up to Next-to-Next-to-Leading Order (NNLO). The matrix element calculations, the PDF sets, the programs used to simulate the parton shower and underlying events of these generators are summarized in Table 2.4.

CHAPTER III

LHC and ATLAS

With its unprecedented high energy and luminosity, LHC will help physicists to address many fundamental questions in the Standard Model as well as to search for new physics beyond the Standard Model. In this chapter, Section 3.1 gives a general introduction of the LHC machine and its four experiments. The ATLAS experiment is one of the four experiments at the LHC with the largest detector in the world. It is a general purpose detector with a wide physics potential [26]. Section 3.2 focuses on the structure and performance of the ATLAS detector.

3.1 LHC

The Large Hadron Collider is a proton-proton synchrotron collider built at CERN, European Organization for Nuclear Research. It uses the tunnel of the Large Electron-Positron Collider (LEP) collider spanning the French-Swiss border with a circumference of 27 km. The LHC is the highest energy collider in the world. The designed proton beam energy is up to 7 TeV, with a center-mass-energy of 14 TeV. Since many interesting physics processes happen rarely, the proton-proton beams are collided at an extremely high rate. The designed instantaneous luminosity is 10^{34} $\mathrm{cm}^{-2}\mathrm{s}^{-1}$, resulting in approximately one billion collisions per second. Besides the proton-proton beams, heavy ions (lead) can also collide at the LHC. The designed heavy ion beam

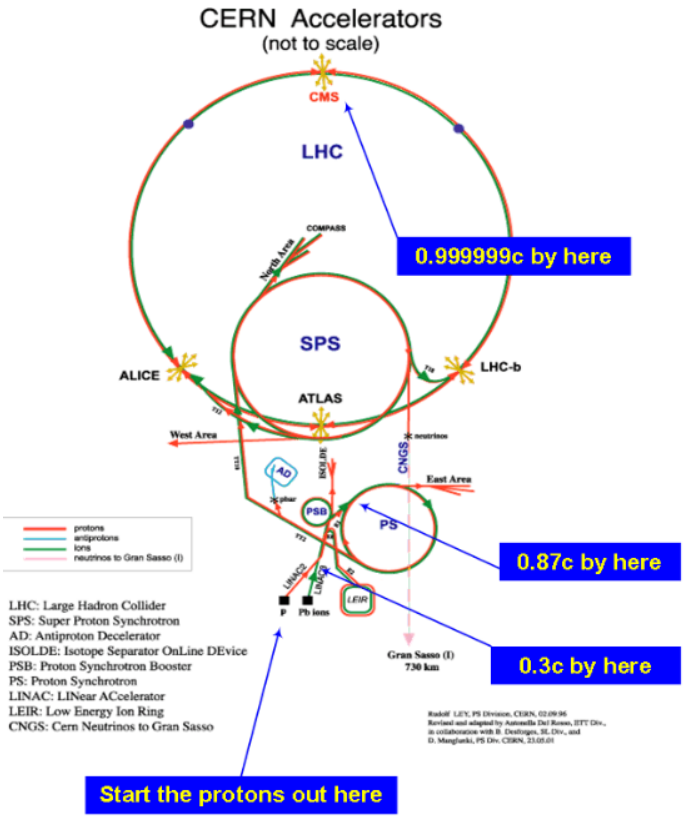

Figure 3.1: Layout of accelerators at CERN.

energy is 2.8 TeV per nucleon and the luminosity is 10^{27} cm^{-2}s^{-1}.

LHC uses high field magnets to keep the proton beams in orbit. The magnets are made of superconductors with magnetic fields up to 8.4 T. There are two different sets of magnets: the dipole and the quadrupole. The dipole is used to bend charged particles and the quadrupole is used to focus the beam. The LHC consists of 1232 main dipoles and 392 quadruples. The cavities of the LHC, which accelerate protons, are operated at a radiofrequency of 400 MHz. The pre-acceleration system for the LHC are: the Linac, the Booster, the Proto Synchrotron (PS) and the Super Proton Synchrotron (SPS). The proton beams are produced from an hydrogen source. The Linac boosts the protons up to 50 MeV, then Booster, PS and SPS accelerate the beams to 1.4, 25 and 450 GeV, respectively, before they are finally injected into the LHC. The layout of these accelerators is shown in Figure 3.1.

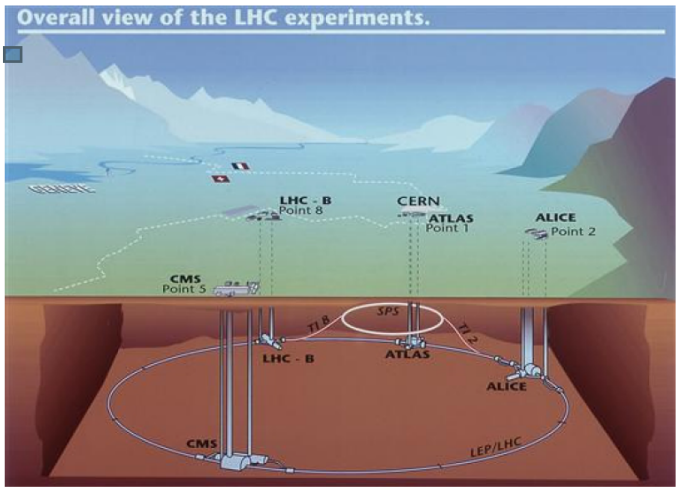

Figure 3.2: Overview of the LHC and its four experiments.

The luminosity for an hadron collider is given by

$$\mathcal{L} = \frac{\gamma_p f k_B N_p^2}{4\epsilon_n \beta^*} F \tag{3.1}$$

where γ_p is the Lorentz factor of protons, f is the revolution frequency, k_B is the number of bunches, N_p is the number of protons per bunch, ϵ_n is the normalized transverse emittance, β^* is the amplitude function [27] at the interaction point (IP) and F is the reduction factor due to the crossing angle. Four experiments are located at the interaction points: ATLAS (A Toroid LHC ApparatuS), CMS (Compact Muon Solenoid), LHCb (Large Hadron Collider Beauty experiment) and ALICE(A Large Ion Collider Experiment). ATLAS and CMS are two general purpose detectors with different technologies so that the measured collision events are doubled and results from two experiments can be cross-checked. LHCb is a single arm spectrometer designed for b-physics studies. ALICE is a heavy ion collision detector to investigate complex, strongly interacting systems and the quark-gluon plasma. The LHC and its four experiments are shown in Figure 3.2.

In year 2010, LHC started to collide proton-proton beams at 3.5 TeV per beam. The peak luminosity reached 2×10^{32} cm^{-2}s^{-1} with an integrated luminosity of 47

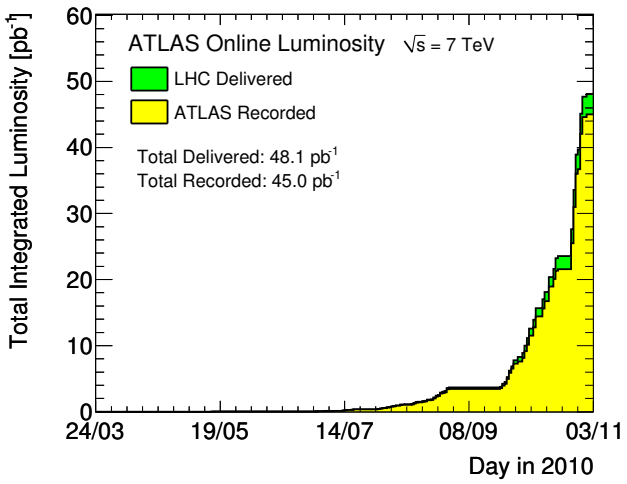

Figure 3.3: The integrated luminosity versus time delivered by the LHC and collected by the ATLAS detector in 2010.

pb^{-1}. The delivered and recorded integrated luminosity of the ATLAS experiment versus time are shown in Figure 3.3.

3.2 ATLAS

ATLAS is a general purpose detector at the LHC. It is designed for physics studies both within and beyond the Standard Model. The principle physics aims of ATLAS can be divided into four categories: Standard Model Physics, Higgs Physics, searches for physics beyond the Standard Model and heavy ion physics. To detect and measure different types of particles varying from few MeV to few TeV, the ATLAS design principles are

- Fast, radiation-hard electronics and sensors with a high granularity;
- Good momentum resolution, detector efficiency and vertex identification(*e.g.* secondary vertex reconstruction from b and τ decay);
- Electromagnetic (EM) calorimeter for electron and photon measurements and full coverage hadronic calorimeter for jet and missing transverse energy (E_T^{miss}) measurements;

Sub-detector	Required Resolution	η coverage Measurement	L1 Trigger
Tracking	$\frac{\sigma_{p_T}}{p_T} = 0.05\% p_T \oplus 1\%$	± 2.5	-
EM Calorimeter	$\frac{\sigma_E}{E} = \frac{10\%}{\sqrt{E}} \oplus 0.7\%$	± 4.9	± 2.5
Hadronic Calorimeter			
barrel and endcap	$\frac{\sigma_E}{E} = \frac{50\%}{\sqrt{E}} \oplus 3\%$	± 3.2	± 3.2
forward	$\frac{\sigma_E}{E} = \frac{100\%}{\sqrt{E}} \oplus 10\%$	$3.1 < \lvert\eta\rvert < 4.9$	$3.1 < \lvert\eta\rvert < 4.9$
Muon Spectrometer	$\frac{\sigma_{p_T}}{p_T} = 10\%$	± 2.7	± 2.4

Table 3.1: ATLAS design performance requirements. The muon spectrometer performance is quoted for a muon with $p_T = 1$ TeV, measured in the standalone mode, independently of the inner detector [3].

- Muon identification and measurement over a wide range of energies;
- High efficiency triggers with excellent background rejection, capable of working with low thresholds in a high multiplicity environment.

The designed energy/momentum resolution for the sub-detectors are summarized in Table 3.1.

A common set of coordinates is used throughout the ATLAS detectors. The z direction is defined to be aligned with the beam pipe, with the origin located at the center of the detector. The horizontal x axis is defined to point towards the center of the LHC ring and the y axis vertically. The polar (θ) and azimuthal (ϕ) angles are defined with respect to this right-handed (x, y, z) system. Instead of θ, it is more convenient to use the pseudorapidity (η) to describe the polar angle as the difference in η between two massless particles, $\Delta\eta$, is invariant under the Lorentz boost along the beam direction. η is defined as

$$\eta = -\ln\tan(\theta/2). \tag{3.2}$$

Radial distance is denoted by $R = \sqrt{x^2 + y^2}$, while the transverse momentum is $p_T = \sqrt{p^2 - p_z^2} = p/\cosh\eta$. Similarly, the transverse energy is defined as $E_T =$

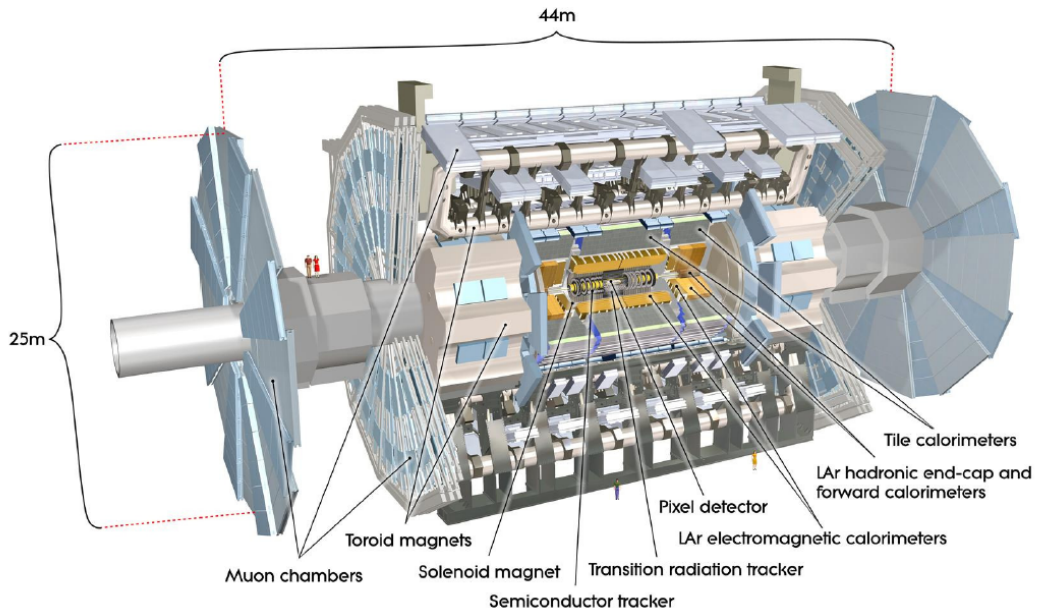

Figure 3.4: Schematic view of the ATLAS detector.

$E/\cosh\eta$. Since the particles are very energetic (> 1 GeV) in the TeV scale proton-proton collisions, the electrons and muons masses are usually ignored so that $E_T \approx p_T$.

A schematic view of ATLAS detector is shown in Figure 3.4. It consists of an inner detector, an electromagnetic calorimeter, a hadronic calorimeter, a muon spectrometer and a three-level trigger system, which will be introduced in the following sections.

3.2.1 The Inner Detector

The Inner Detector (ID) is responsible for the track and vertex reconstructions of charged particles. Due to the high charged particle density from the LHC collisions, the ID uses a high granularity design. It consists of three tracking technologies: the Pixel Detector (Pixel), the Semi-Conductor Tracker (SCT) and the Transition Radiation Tracker (TRT). These three sub-systems are each divided into one barrel and two endcap sections with the coverage region up to $|\eta^{\text{track}}| < 2.5$ and $p_T^{\text{track}} > 0.5$ GeV . The ID is immersed in a 2 T magnetic field provided by a superconducting

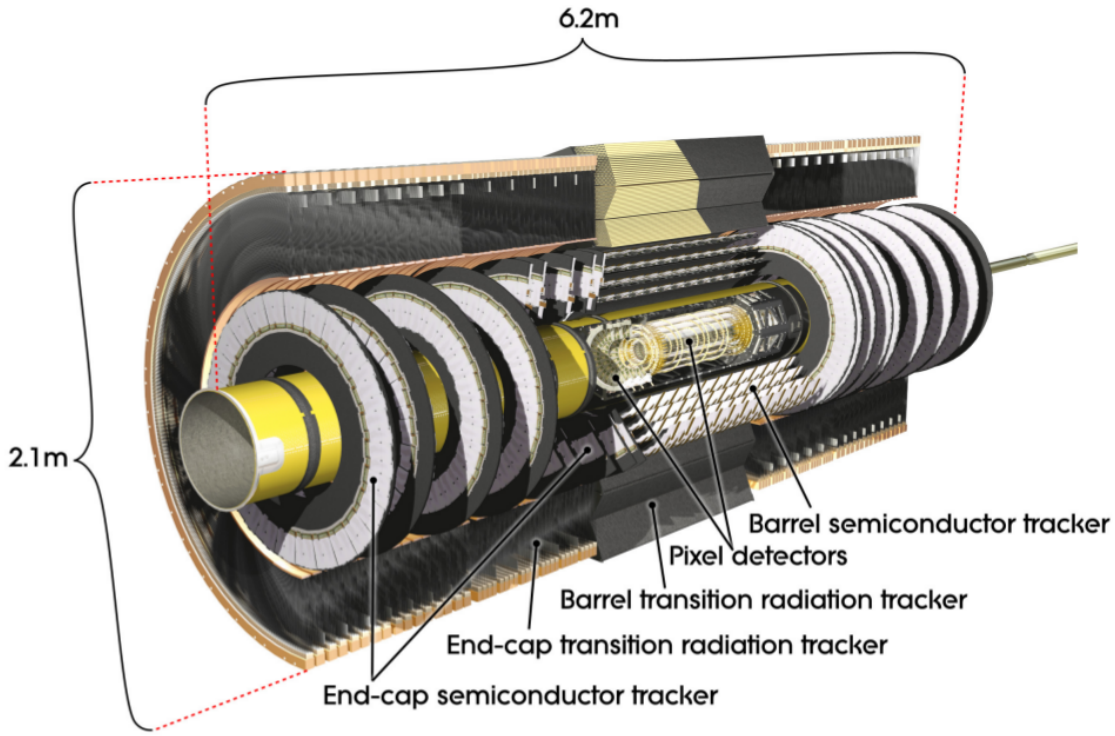

Figure 3.5: Schematic view of the ATLAS inner detector. It consists of three main components: the pixel detector, SCT and TRT.

solenoid which is located at the inner face of the electromagnetic calorimeter. The ID structure is shown in Figure 3.5.

One of the most important parameters of the ID is the amount of material it contains. The materials will cause multiple scattering, bremsstrahlung and photon conversion, which deteriorate the track reconstruction quality and momentum measurement [26]. The magnitude of these effects is determined by the number of radiation lengths [28] traversed by a particle passing through the ID, which is shown in Figure 3.6 as a function of $|\eta|$. The gap between barrel and endcaps can be seen at $|\eta| \approx 1.5$.

A successful ID alignment is crucial for a precise track measurement. To calibrate the ID alignment during normal runs, a daily selection of approximate one million tracks is used for monitoring studies. This should be sufficient to determine the silicon

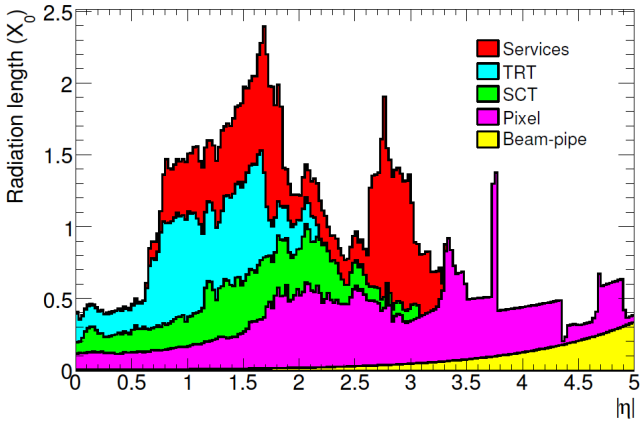

Figure 3.6: Accumulative materials traversed within the inner detector envelope by an infinite momentum track as a function of $|\eta|$. The material depth is measured in units of radiation length X_0.

module positions with a precision of 10 μm.

In addition to the material and alignment, the magnetic field calibration inside the ID volume is also important. This is achieved by using MC simulation and a movable array of Hall probes before the ID installation, with the barrel and endcap calorimeters installed [26]. The bending uncertainty of the magnetic field varies from 2% to (12×10^{-4})% for tracks with p_T from a few hundred MeV to a few TeV, mostly satisfying the requirement for a precise W mass measurement.

3.2.1.1 The Pixel Detector

The pixel detector lies closest to the interaction point. When a particle passes through the pixel element, it induces an electrical signal by the creation of an electron-hole pair. The signal is amplified and compared to a set threshold to give a binary output.

The granularity size of the pixel element, which is made of silicon, is 50×400 μm. There are three concentric layers and five additional disks in each endcap side with the high pseudorapidity. Over 1,500 modules, segmented in $R - \phi$ and z, provide approximately 80.4 M readout channels.

The pixel detector is also responsible for the measurements of impact parameters and vertex reconstructions. The position resolution of the pixel detector is down to 10 μm in $R-\phi$ and 115 μm in $z(R)$ in the barrel(endcap), which is crucial for finding secondary vertices of c, b and τ decays.

To protect the pixels and other ATLAS components from misdirected proton beams, an instrument called the Beam Conditions Monitor (BCM) is installed very close to the beam line. The BCM consists of two diamond sensors, placed less than 6 cm from the beam at $|z| = 1.9$ m. So the time difference between nominal proton-proton collisions and beam gas collisions will be $\Delta z/c = 12.5$ ns, which can be used to trigger an LHC beam abort. In addition to the protection feature, the BCM is also used as a signal trigger and for a bunch-by-bunch luminosity estimation, complementary to LUminosity measurement using a Cherenkov Integrating Detector (LUCID), which is the principal instrument for the luminosity measurement.

3.2.1.2 The Semi-Conductor Tracker

The working principle of the SCT is very similar to that of the pixel detector but with a coarser position resolution. The SCT consists of 4 concentric barrels and 9 disks of endcaps on each side. Silicon microstrips are glued into back-to-back pairs with a stereo angle of 40 mrad between them, which is designed to reduce ambiguities to acceptable levels. The SCT usually provides four space points for each track within the acceptance. In the barrel, one set of strips is aligned along the z direction; and in the endcaps, one set is aligned along the R direction, which is used for a precision measurement of ϕ. The $R-\phi$ resolution is up to 17 μm. The resolution of the z (R) direction in the barrel (endcaps) is worse, around 580 μm, due to the small stereo angle.

3.2.1.3 The Transition Radiation Tracker

The TRT is the outer-most layer of the ID, which provide a large number of hits per track, typically 36. It also provides the particle identification through the detection of transition radiation. The TRT consists of drift tubes of diameter 4 mm and length 144 cm lying parallelly (radially) to the beam line in the barrel (endcaps). Charged particles will ionize the gas inside the tubes and thus cause an electrical signal along an anode wire in the middle of the tube. When ultra-relativistic particles, *e.g.* electrons pass through the tubes, they can produce low energy transition radiation photons which then ionize the xenon gas mixture and induce high threshold hits [26]. The measured probability for such hits increases as a function of E/m, thus the TRT can provide the identification of electrons and pions.

3.2.2 The Electromagnetic Calorimeter

The Electromagnetic (EM) calorimeter is designed for two purposes: firstly it provides the precise measurement and identification of electrons and photons; secondly it complements to the hadronic calorimeter to measure the energy deposit of jets within its acceptance. The ATLAS calorimeter covers the region up to $|\eta| = 4.9$. It consists of five parts: one barrel, two endcaps and two forward calorimeters. A schematic view of the EM calorimeters is shown in Figure 3.7.

Liquid argon is used as the ionization medium for the EM calorimeter. Liquid argon fills the gaps between the accordion-shaped lead absorbers and kapton electrodes. A slice of EM calorimeter is shown in Figure 3.8. In the ϕ direction, the accordion-shaped calorimeter has a uniform coverage, while in the η direction, the folding angle, absorber thickness and wave amplitude are tuned to optimize the linearity and resolution. As shown in Figure 3.8, the EM calorimeter consists of several layers. Within $|\eta| < 2.5$, which is also covered by the ID, there are three layers. The first layer is finely segmented in η. It provides a precise measurement in η. The second layer is

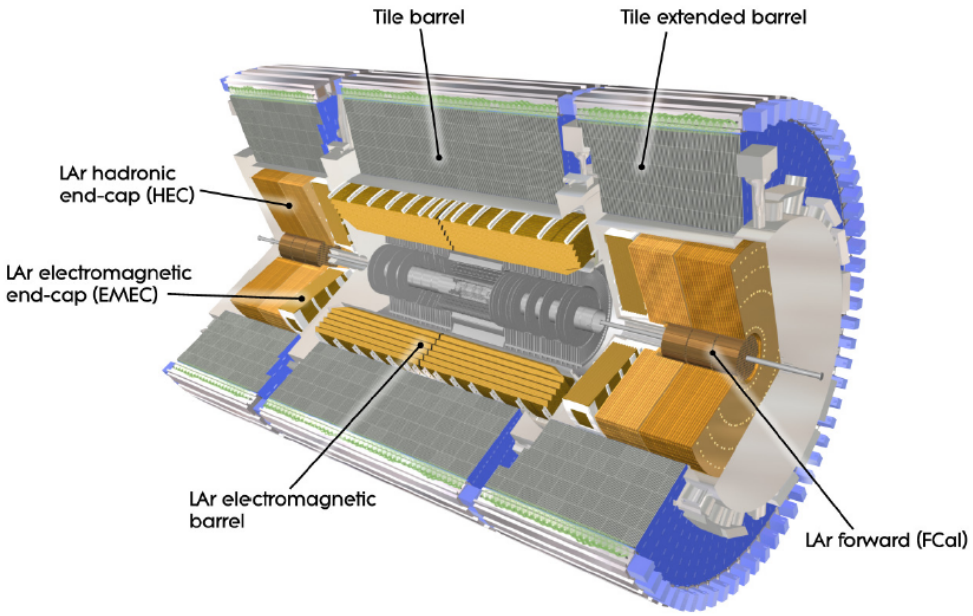

Figure 3.7: An schematic view of the ATLAS electromagnetic (yellow) and hadronic (blue) calorimeters. The electromagnetic calorimeter consists of five components: one barrel, two endcaps and two forward calorimeters. The hadronic calorimeter has two additional forward components (FCal).

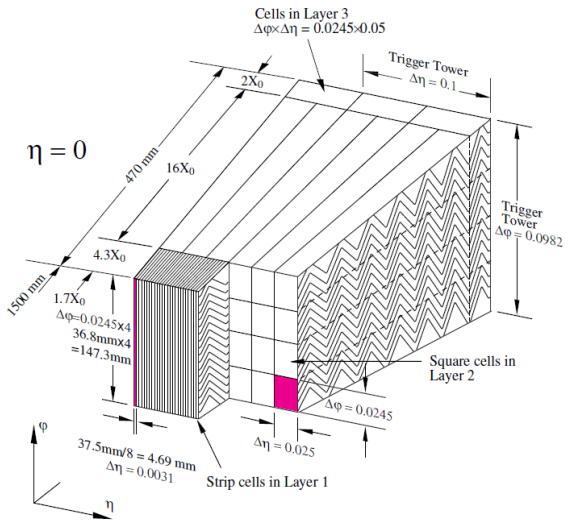

Figure 3.8: A slice of the ATLAS EM calorimeter showing the accordion structure as well as the different granularity in each layer and trigger tower.

the thickest, so most of the electromagnetic energy is deposited in it. The third layer, in front of the hadronic calorimeter, is used to measure the possible energy leakage from EM shower. Within the range $|\eta| < 1.8$, there is an additional layer before the first layer of the EM calorimeter. It is called pre-sampler, which estimates the energy loss of electrons and photons before reaching the EM calorimeter. In the region $2.5 < |\eta| < 3.2$. the design is similar, but with a coarser granularity and only two longitudinal layers. In the region $|\eta| > 3.2$, a different set of liquid argon calorimeters measure both electromagnetic and hadronic showers, which will be discussed in the next section.

3.2.3 The Hadronic Calorimeter

The hadronic calorimeter measures hadronic showers from a jet, a collimated flow of particles, resulting from an energetic quark or gluon of hard interactions. It covers the region $|\eta| < 4.9$. It completely stops and absorbs all strongly interacting particles and avoids particles punching through into the muon spectrometers. So the depth of the hadronic calorimeter is designed to be at least 10 interaction lengths over almost

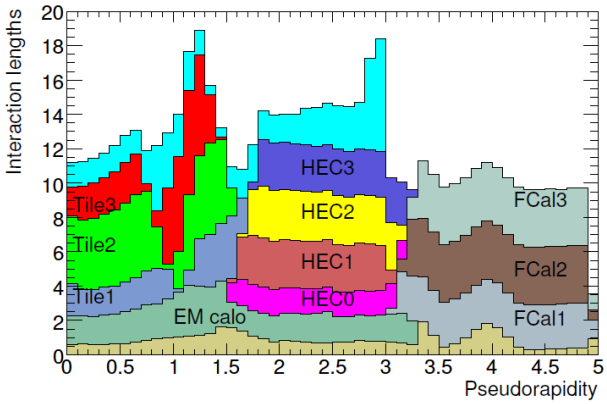

Figure 3.9: Accumulative depth of the hadronic calorimeter. The depth is in unit of interaction of length λ.

full η region. Figure 3.9 shows the depth of the hadronic calorimeter in the $|\eta|$.

The hadronic calorimeter consists of at least three layers over its full region. In the region $|\eta| < 1.7$, a sampling calorimeter called Tile Calorimeter (TileCal) is used. It is made of steel absorbers and scintillating tiles arranged as shown in Figure 3.10. The scintillation light in the tiles is read out through wavelength shifting fibers, by photomultiplier tubes behind each calorimeter module. In the region $1.5 < |\eta| < 3.2$, the hadronic endcap Hadronic Endcap Calorimeter (HEC) uses a liquid argon technology due to the intense radiation environment. It is similar to the EM calorimeter but with copper absorbers to provide the necessary density of material. The forward calorimeter covers the region $3.2 < |\eta| < 4.9$. It also uses liquid argon as the active medium. The Forward Calorimeter (FCal) has a high density design with high granularity output to accommodate the high particle density in this region. It consists of three longitudinal modules. The first module uses copper absorbers for the measurement of the electromagnetic shower. The other two modules have tungsten absorbers for the measurement of the hadronic shower [29].

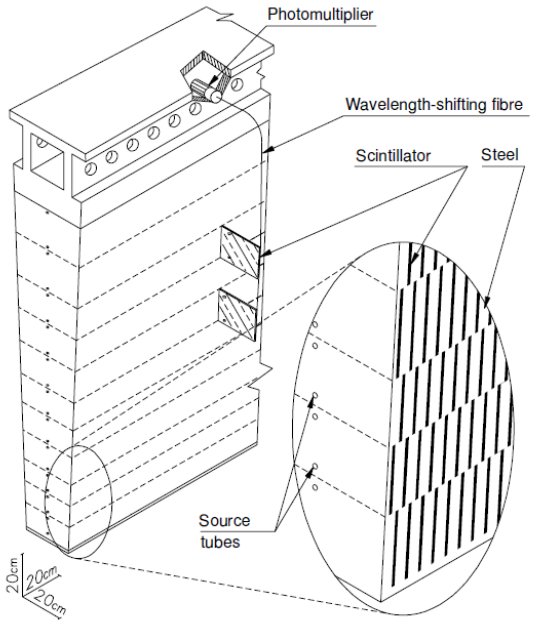

Figure 3.10: Schematics of a TileCal module, showing the optical readout from the scintillating tiles.

3.2.4 The Muon Spectrometer

The muon spectrometer is designed to measure the curvature of muons in the toroidal magnetic field, independently of the ID. It is the largest sub-detector in ATLAS. Besides neutrinos, muons are the only particles that can penetrate the EM and hadronic calorimeters. The muon spectrometer consists of two precision measurement sub-systems: Monitored Drift Tubes (MDT) in the central region with $|\eta| < 2.4$ and Cathode Strip Chambers (CSC) in the forward region with $2.4 < |\eta| < 2.7$. The muon trigger systems consist of Resistive Plate Chambers (RPC), Thin Gap Chambers (TGC) and CSC, which cover the region with $|\eta| < 1.05$, $1.05 < |\eta| < 2.4$ and $2.4 < |\eta| < 2.7$, respectively. A schematic view of the muon spectrometer is shown in Figure 3.11.

There are three stations for the muon spectrometer in both barrel and endcap regions. The chambers are aligned projectively from the interactive point. Muons bend in the η direction in the toroid field, which are measured by the MDT and CSC

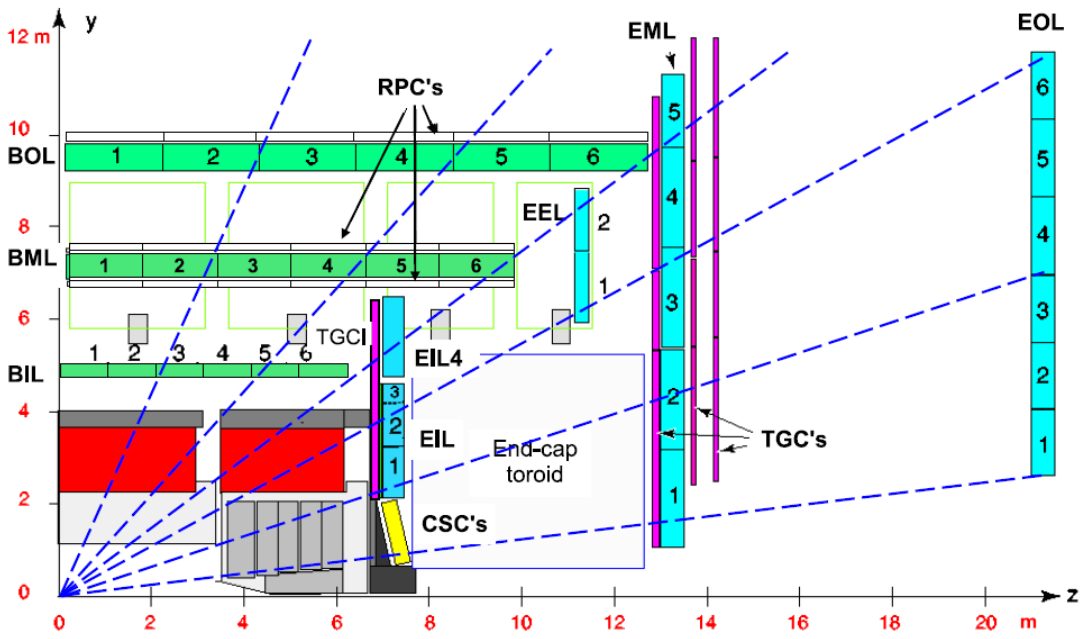

Figure 3.11: Schematic view of the muon spectrometer.

in the central and forward regions, respectively. The trigger chambers are arranged between the precision chambers. They provide a fast signal for the level-one trigger decision as well as the bunch crossing identification information. In addition, they also measure the muon bending in the ϕ direction.

The modules must be aligned to a high precision due to the stringent design requirement. The expected sagitta of a muon track with $p_T = 1$ TeV is only ≈ 0.5 mm within the muon spectrometer. Thus, the muon spectrometer alignment uncertainty must be significantly smaller than this. To calibrate the muon chambers, a complex optical alignment system is installed to achieve a precision of around 30 μm on sagitta measurements [26].

3.2.5 The Trigger System

The designed LHC bunching crossing rate is 40 MHz. On one hand, it is not feasible to permanently record every event to disk. On the other hand, only a small fraction

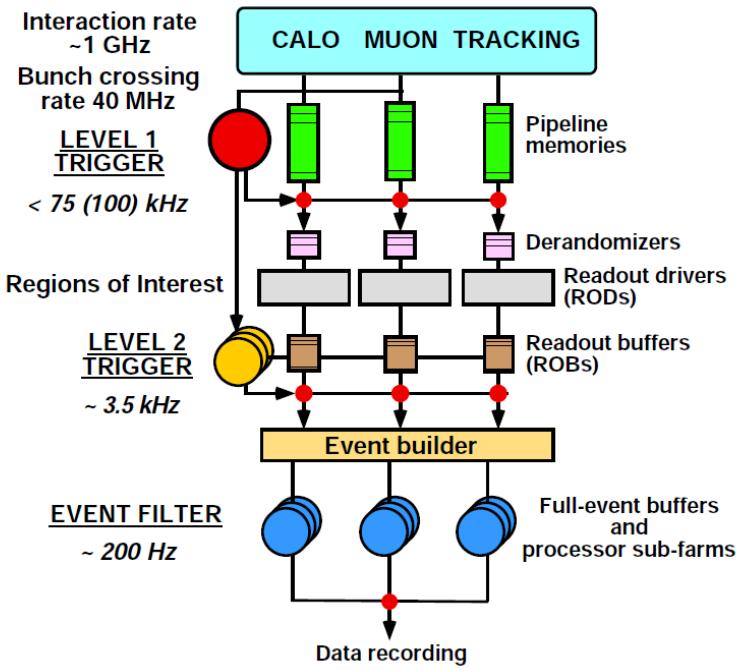

Figure 3.12: The ATLAS three-level trigger system.

of collision events contain interesting physics signatures. Thus, the ATLAS trigger system is designed to reduce the event rate to $\approx$ 200 Hz while keep high efficiency for interesting signal events. The ATLAS trigger has three levels: a Level One (L1) trigger based on hardware, a Level Two (L2) trigger mostly based on firmware and an Event Filter (EF) based on software. The L2 trigger and EF are usually collectively called as the High Level Trigger (HLT). Each level improves on the previous levels decision by running increasingly sophisticated algorithms, at the cost of increased execution time. The three-level triggers are applied sequentially: if the event is rejected at certain level, it will not enter the next level, thus it will not be recorded. The trigger information is based on Region Of Interest (ROI), which describe the position and threshold of the fired trigger. A schematic view of the ATLAS trigger system is shown in Figure 3.12.

During the earlier stages of running ($L < 10^{33}$ cm^{-2}s^{-1}), the event acceptance rate at each level is maintained as a constant with less stringent criteria. In addition

to less severe selection criteria, early triggers may run one or more levels in pass-through mode, meaning that the event is passed to the next level without further selection.

At high luminosities, some loose triggers will continue to run for monitoring purposes, but they will be heavily pre-scaled. This means that only a small, randomly selected subset of events passing the trigger selection will be fed into the next level.

The L1 trigger reduces the event recording rate from 40 MHz to 75 kHz. If an event passes an L1 trigger, the information of the ROI will be sent to the L2 trigger. The L2 trigger makes a decision in $\approx$ 10 ms using both ROI and additional information related to the ROI, and the output rate is reduced to $\approx$ 3.5 kHz. The EF algorithm is similar to L2 but more sophisticated, thus the processing time is even longer ($\approx$ 1s). The EF output rate is 200 Hz and events passing the EF will be recorded to mass storage.

For example, the L1 trigger of the Egamma stream uses the ROI from the EM calorimeter to make a decision. The information comes from the trigger "tower", $\Delta\eta \times \Delta\phi = 0.1 \times 0.1$ segments in the EM and hadronic calorimeters. Then L2 and EF triggers apply additional requirements on the shower shape as well as inner detector information of tracks which match to the ROI to make further decisions. The details of the electron trigger will be presented in the next chapter.

CHAPTER IV

Electrons in ATLAS

The electron identification and measurement are crucial for the $Z \to ee$ differential cross-section measurement. In this chapter, the ATLAS standard electron reconstruction and identification algorithms are introduced in Section 4.1. The electron trigger algorithms are discussed in Section 4.2. Section 4.3 presents the "tag-and-probe" method which is used to measure the electron identification and trigger efficiencies from data. The electron energy scale and resolution are calibrated using the well known Z boson line-shape. Studies of the electron energy scale and resolution are presented in Section 4.4.

4.1 Electron Reconstruction and Identification

4.1.1 Reconstruction

The electron is seeded from an electromagnetic tower with transverse energy above 3 GeV taken from the EM calorimeter. Then a track is searched to match the tower among all reconstructed tracks which do not belong to a photon-conversion pair reconstructed in the inner detector. The track, after extrapolation to the EM calorimeter, is required to match the cluster within a broad $\Delta\eta \times \Delta\phi$ window of 0.05×0.10. The ratio, E/p, of the energy of the cluster to the momentum of the track is required to be lower than 10. Approximately 93% of true isolated electrons [26], with $E_T > 20$ GeV

and $|\eta| < 2.5$, are selected as electron candidates. The inefficiency is mainly due to the large amount of material in the inner detector [30] and is therefore η-dependent.

4.1.2 Identification

Standard identification of high p_T electrons is based on many cuts which are applied independently. These cuts have been optimized in up to 10 bins in η and up to 11 bins in E_T . Three different electron identification criteria are defined: loose, medium and tight, which provides flexibility in different analyses. In the $Z \rightarrow ee$ analysis, "medium" electrons are used since the study is not subjected to large backgrounds from jets misidentified as electrons (fakes).

The variables used to select loose, medium and tight electrons are

- Loose Electron:
  - Electron transverse energy and pseudorapidity, E_T and η;
  - Ratio in η of cell energies in 3×7 versus 7×7 cells, R_η;
  - Ratio in ϕ of cell energies in 3×3 versus 7×7 cells, R_ϕ;
  - Lateral width of the shower.
- Medium Electron:
  - Difference between energy associated with the second largest energy deposit and energy associated with the minimal value between the first and second maxima, ΔE_s;
  - Second largest energy deposit normalized to the cluster energy, R_{max2};
  - Total shower width, w_{stot};
  - Number of hits in the pixel detector;
  - Number of hits in the pixels and SCT;

- Transverse impact parameter, d_0;
- $\Delta\eta$ between the cluster and the track;
- Ratio of the cluster energy to the track momentum, E/p;
- Total number of hits in the TRT;
- Ratio of the number of high-threshold hits to the total number of hits in the TRT.

- Tight Electron:
  - Number of B layer (first layer of the pixel detector) hits;
  - Same as TRT cuts above, but with tighter values corresponding to about 90% efficiency for isolated electrons.

4.1.3 Object Quality

During the course of the data taking, some regions of the EM calorimeter were disabled due to the dead Optical Transmitter (OTX), a part of the Front-End Board (FEB). The OTX cleaning removes events with electron candidates that fall into these regions to suppress electrons for which significant parts of the energy deposition are not measured.

The dead FEBs are in three layers of the EM calorimeter: pre-sampler, the first layer and second layer. The number of dead FEBs increased with time. The latest dead FEB maps are shown in the Figure 4.1(a), 4.1(b), 4.1(c). The electrons in this analysis are required not to be in any of dead FEB regions. The OTX cleaning efficiency is about 94% per electron.

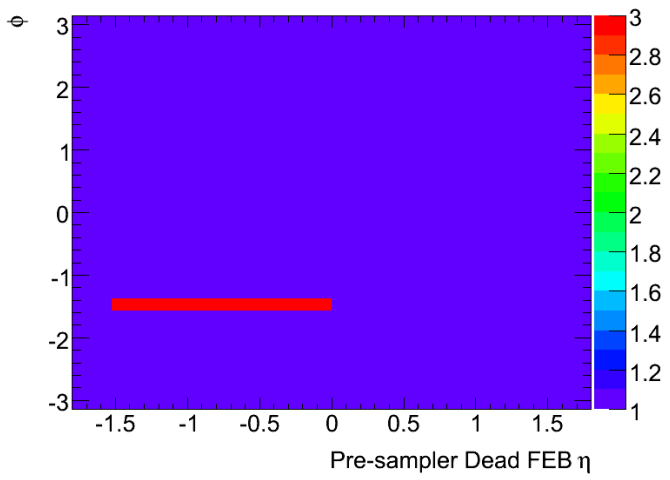

(a)

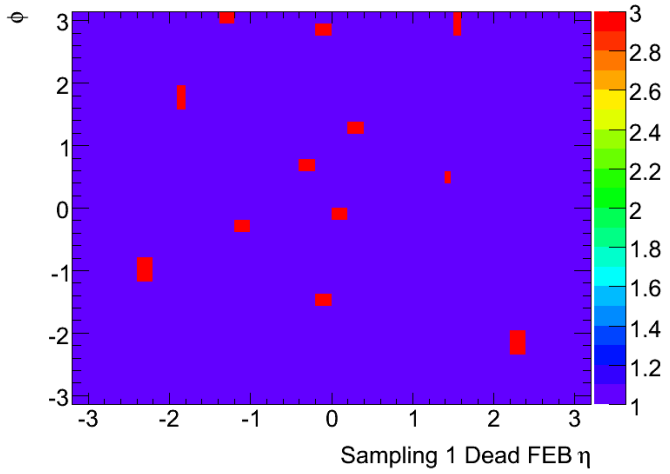

(b)

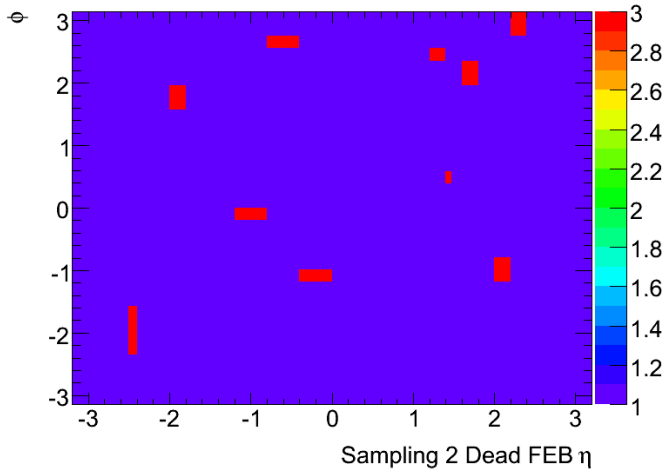

(c)

Figure 4.1: The dead FEBs (red) in the EM calorimeter: (a) pre-sampler (b) first layer (c) second layer.

4.2 The Electron Trigger

4.2.1 Level One

The electron L1 trigger ROI is an electromagnetic or hadronic calorimeter tower with dimensions $\Delta\eta \times \Delta\phi = 0.1 \times 0.1$. In this region all readout cells are summed over the full depth of either the electromagnetic or hadronic calorimeter. The L1 selection algorithm for electromagnetic clusters is based on a sliding 4×4 window of trigger towers which searches for the local maximum.

The trigger object is considered to contain an electron or photon candidate if the following requirements are satisfied:

- The central 2×2 "core" cluster consisting of both EM and hadronic towers is a local E_T maximum. This requirement prevents double counting of clusters by overlapping windows;
- The most energetic of the four combinations of two neighboring EM towers passes the electromagnetic cluster threshold;
- E_{isol}^{EM}: The total E_T in the 12 EM towers surrounding the 2×2 core cluster is less than the electromagnetic isolation threshold;
- E_{core}^{HAD}: The total E_T in the 4 towers of the hadronic calorimeter behind the 2×2 core cluster of the electromagnetic calorimeter is less than the hadronic core threshold;
- E_{isol}^{HAD}: The total E_T in the 12 towers surrounding the 2×2 core cluster in the hadronic calorimeter is less than the hadronic isolation threshold.

4.2.2 Level Two

The L2 trigger is seeded from the L1 ROI. Thus, L2 receives the reconstructed L1 object with the η and ϕ positions and the transverse energy thresholds passed. L2

accesses a sub-sample of the detector data around the given η and ϕ position ($\Delta\eta \times \Delta\phi = 0.4 \times 0.4$) and applies trigger specific reconstruction algorithms characterized for their speed and robustness. The transverse cluster energy and various shower shape variables calculated in the different layers of the EM calorimeter are used to identify electron and photon candidates. Tracks are reconstructed in the inner detector and matched to the calorimeter energy clusters at the L2 level. Thus, track finding and track-cluster matching variables can be used for the L2 trigger decision.

The L2 electron calorimeter algorithm selects events base on the following quantities:

- The transverse energy of the EM cluster;
- The transverse energy in the first layer of the hadronic calorimeter E_T^{HAD};
- The shower shape in η direction in the second EM sampling;
- The second maximum in the first EM sampling.

4.2.3 Event Filter

At the EF trigger level, offline reconstruction algorithms and tools are used as much as possible. An important difference, however, between the offline and the EF reconstruction is that the offline reconstruction is run once per event accessing the whole detector, while the EF uses a seeded approach. It runs several times per event, once for each ROI given by L2, accessing only the corresponding sub-sample of the detector($\Delta\eta \times \Delta\phi = 0.4 \times 0.4$).

Electron identification in the EF is very similar to the offline. Calorimeter shower shapes, leakage into the hadronic calorimeter and the E_T of the EM cluster are used for the calorimeter based selection for electrons. Compared to L2 more shower shape variables are used. Together with improved calibrations, this results in a further rate reduction. For electrons track-cluster matching variables, track quality cuts,

transverse impact parameter and for high luminosity running potentially transition radiation information could be used to further reduce the rate.

As an example, a loose electron EF selection will use the following selections: longitudinal leakage, shower shapes in the middle layer of the EM calorimeter, and very loose track-cluster matching cuts. Tighter selections might also use the shower shapes in the first EM calorimeter layer, information on the transverse impact parameter and on the track quality (number of hits in the pixels, SCT and B layer).

The 2010 data are divided in periods from A to I, which correspond roughly to periods of similar LHC operation conditions, i.e. beam intensities and number of bunches. The trigger chains were chosen to have the lowest threshold un-prescaled triggers which are stable in certain period. The EF became active since the period E3. Therefore, at least one L1 trigger chain is needed before the period E3 and one EF trigger chain for the remaining periods. Since medium electrons are used in the analysis, the lowest threshold un-prescaled trigger chains are L1_EM14 and EF_e15_medium for periods A to E3 and E3 to I, respectively.

4.3 The Tag-and-probe Method

The tag-and-probe method is used to measure the electron identification and trigger efficiency from data. It requires that the event should have two reconstructed electron candidates, one "tag" and one "probe", within the detector acceptance and with the invariant mass around Z mass peak

- $E_T > 20$ GeV;
- $|\eta| < 2.47$ and $|\eta| \notin (1.37, 1.52)$;
- $81 < m_{ee} < 101$ GeV.

The tag is a tight electron to ensure a clean sample from the Z decay. Additional isolation requirements are applied on tags to assess the systematic uncertainty. The

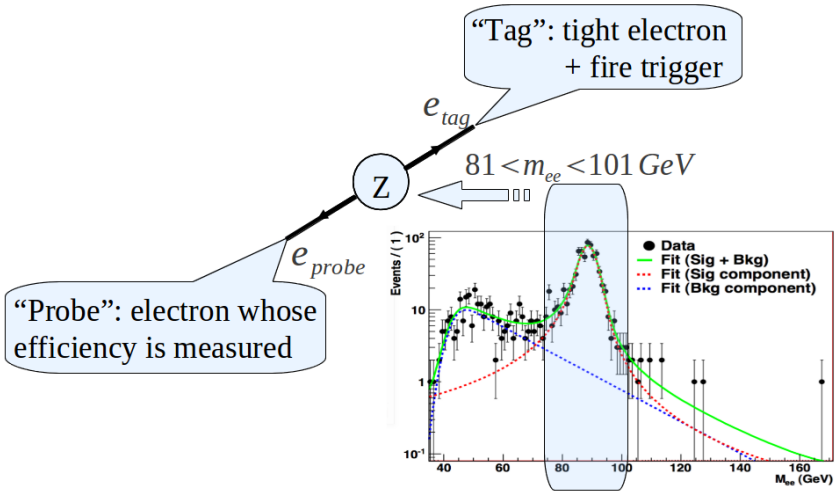

Figure 4.2: The tag-and-probe method used to measure electron efficiencies.

identification (trigger) efficiency is defined by the frequency with which the probe electron in this sample passes the relevant identification (trigger) selection. The tag electron is also required to fire the electron trigger of the event to eliminate potential bias. The tag-and-probe method is demonstrated in Figure 4.2.

It is possible that the probe electron satisfies the tag selection as well. In this case, the roles of tag and probe may be swapped: the tag becoming the probe and vice versa. Because the tag selection is at least as tight as the probe selection at every stage, the new probe passes the trigger selection automatically. Thus, tag and probe events fall into one of three categories:

- N_{1f} events where only one electron passes the tag cuts and the probe fails the probe selection.
- N_{1p} events where only one electron passes the tag cut and the probe passes the probe selection.
- N_{2p} events where both electrons pass the tag selection.

Counting these events, the measured efficiency may be expressed as

$$\epsilon = \frac{N_{1p} + 2N_{2p}}{N_{1f} + N_{1p} + 2N_{2p}} = \frac{N_P}{N_T} \tag{4.1}$$

where N_P and N_T are defined by the equation.

The remaining background can be subtracted by the side-band method. Define two side-bands and signal region as

- Side-band A: $61 < m_{ee} < 81$ GeV;
- Signal region B: $81 < m_{ee} < 101$ GeV;
- Side-band C: $101 < m_{ee} < 121$ GeV.

So that the N_P and N_T after background subtraction are defined as

$$N_P = N_P^B - \frac{N_P^A + N_P^C}{2} \qquad N_T = N_T^B - \frac{N_T^A + N_T^C}{2}. \tag{4.2}$$

Assuming the event number N obeys the Poisson distribution, the statistical uncertainty on ϵ is

$$\sigma = \frac{1}{N_T}\sqrt{[(1-2\epsilon)N_P + \epsilon^2 N_T + (1-\epsilon)^2 \cdot 2N_P]}. \tag{4.3}$$

The trigger efficiencies for a single electron versus the electron E_T and η are shown in Figure 4.3(a) and 4.3(b). The medium electron ID efficiencies are shown in Figure 4.4(a) and 4.4(b).

The single electron trigger efficiency is very high and the discrepancy between data and MC is very small, $< 1\%$. There are two electrons from Z decays in which either electron firing the trigger makes the event pass the trigger selection. Thus, data and MC trigger discrepancy is further reduced. There is no need to make a trigger efficiency correction in the MC. However, there is an about 3% difference in

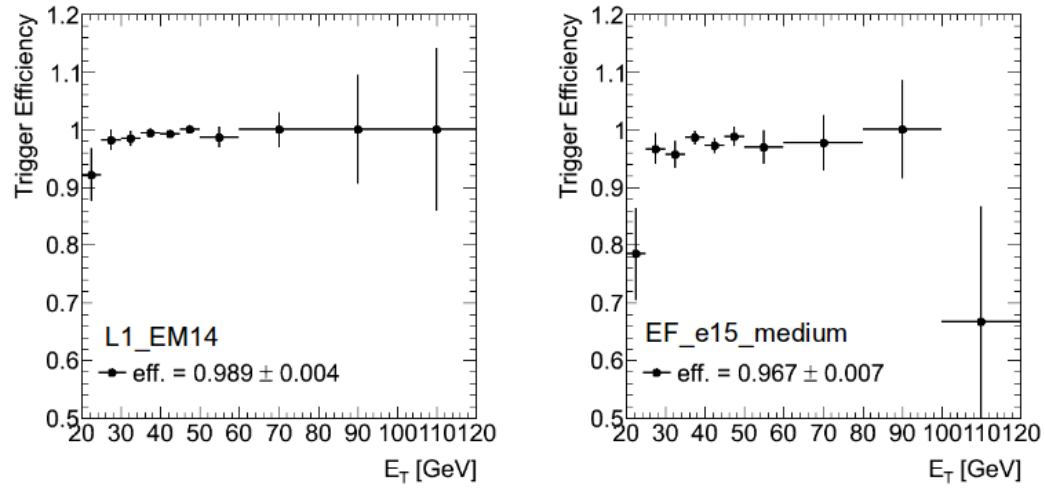

(a)

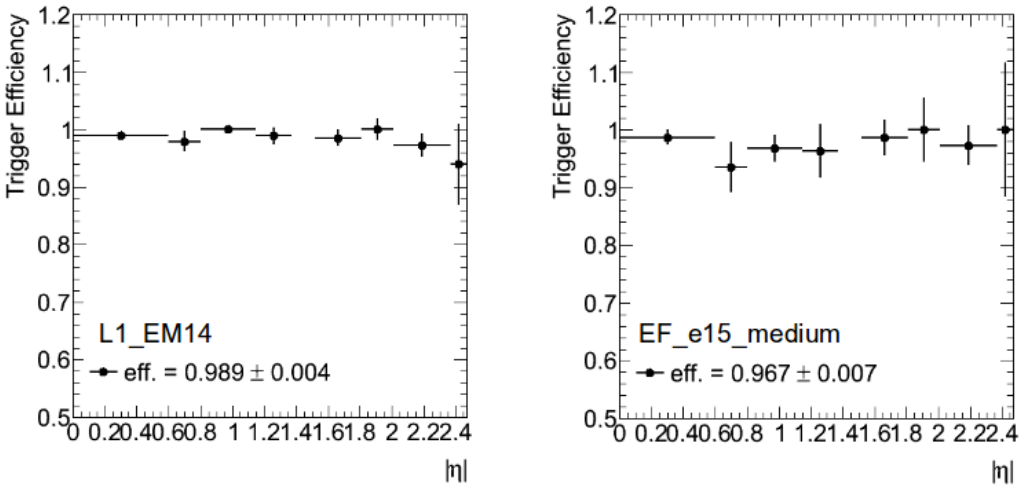

(b)

Figure 4.3: Electron trigger efficiencies versus E_T (a) and $|\eta|$ (b) measured by the tag-and-probe method.

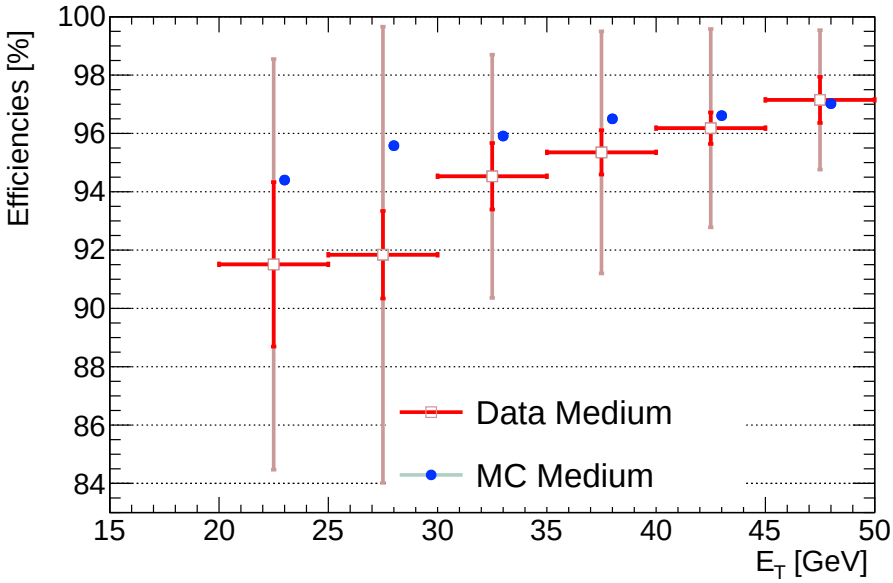

(a)

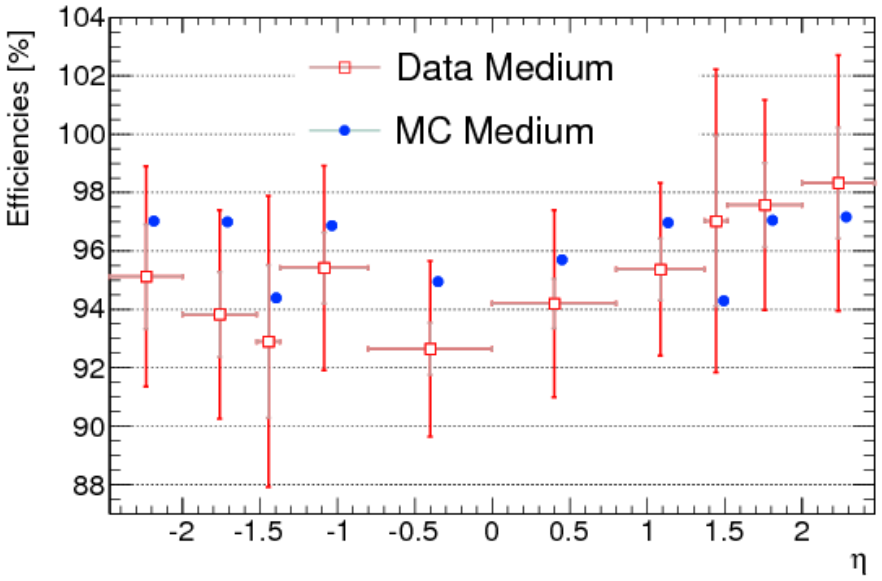

(b)

Figure 4.4: Medium electron ID efficiency versus η and E_T by the tag-and-probe method.

η bin	$(-2.47, -2.01)$	$(-2.01, -1.52)$	$(-1.37, -0.8)$	$(-0.8, 0.0)$
$\frac{\text{data}}{\text{MC}}$	0.945 ± 0.017	0.988 ± 0.016	0.972 ± 0.016	0.974 ± 0.015
η bin	$(0.0, 0.8)$	$(0.8, 1.37)$	$(1.52, 2.01)$	$(2.01, 2.47)$
$\frac{\text{data}}{\text{MC}}$	0.972 ± 0.015	0.967 ± 0.015	0.995 ± 0.029	0.961 ± 0.017

Table 4.1: Efficiency scale factors for single medium electrons. The statistical and systematic uncertainties are combined in quadrature.

the medium electron identification efficiency between data and the MC. This is caused by ID mis-alignment, mis-modeled electron shower shapes and additional materials before the EM calorimeter. A correction must be applied to account for the electron identification discrepancy. Therefore, a set of η dependent Scale Factors (SF) are used on the MC. The scale factor for the electron identification efficiency is defined as

$$SF = \frac{\text{Efficiency measured in data}}{\text{Efficiency measured in the MC}}. \tag{4.4}$$

The scale factors applied in the analysis along with its systematic uncertainties are listed in Table 4.1. The SF systematics arise mainly from different background subtraction methods, efficiency variation from different Z mass windows and pileup effects [30].

4.4 The Electron Energy Scale and Resolution

In the $Z \rightarrow ee$ process, one can extract the electron energy scale factor by constraining the di-electron invariant mass distribution to the well known Z lineshape [31]. The corrected energy is obtained by the following formula

$$E_{new} = \frac{E}{1 + \alpha} \tag{4.5}$$

where E_{new} is the electron energy after the correction, E is the electron energy before the correction and α is the correction factor. α is determined in the barrel and endcaps

by fitting the distribution of the di-electron invariant mass to a template made of a Breit-Wigner distribution convoluted with a Crystal-Ball distribution [32].

Different source of systematic uncertainties were investigated: extra-material, pre-sampler energy scale, event selection, pile-up, MC closure, dead OTX, non-nominal high voltage, electronic non-linearity. The dominant ones are the uncertainties on the knowledge of materials in front of the EM calorimeter and the pre-sampler energy scale.

However, with the appropriate energy scale correction applied, the data still have a broader invariant mass distribution than that of the MC. Thus, an additional energy smearing is applied to the MC. There are two main parameters constraining the electron energy resolution: sampling term and constant term. The relation between the reconstructed electron energy and these two terms is

$$\frac{\sigma}{E} = \frac{S}{\sqrt{E}} \oplus C \tag{4.6}$$

where σ is the resolution of the electron energy; E is the reconstructed electron energy; S is the sampling term and C is the constant term.

The discrepancy between data and the MC is mainly attributed to the constant term because the MC reproduces reasonably well the invariant mass distribution in $J/\psi \to ee$ events for central electrons whose energy resolution is dominated by the sampling term [26]. So a larger smearing factor is applied to the constant term than the sampling term.

In this analysis, the energy scale correction is applied to data and additional energy smearing is applied to the MC. The electron energy scale and smearing uncertainties are used to set the systematic uncertainties of p_T^Z measurements. The electron energy scale and smearing factors and their uncertainties are summarized in Table 4.2.

The invariant mass distributions of electron-positron pairs before and after the energy scale correction are shown in Figure 4.5(a),4.5(b),4.5(c)for barrel-barrel, barrel-

$\|\eta\|$ bin	$[0.0, 1.37]$	$[1.52, 2.5]$
α	-0.0096	0.0189
α uncert.	1%	3%
Sampling term	0.1	
Sampling term uncert.	20%	20%
Constant term	0.007	
Constant term uncert.	100%	400%

Table 4.2: Parameters used in the electron energy correction.

endcap, endcap-endcap three regions respectively. Similarly, the comparisons of the MC invariant mass distributions before and after the energy smearing are shown in Figure 4.6. After the energy scale and smearing corrections are applied, data and $Z \to ee$ MC have a reasonably good agreement.

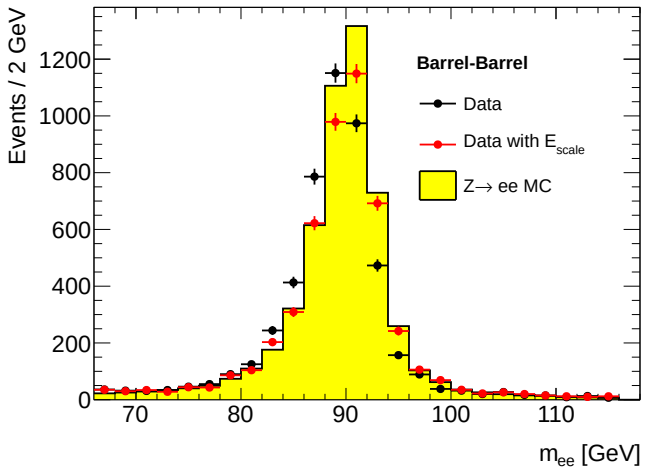

(a)

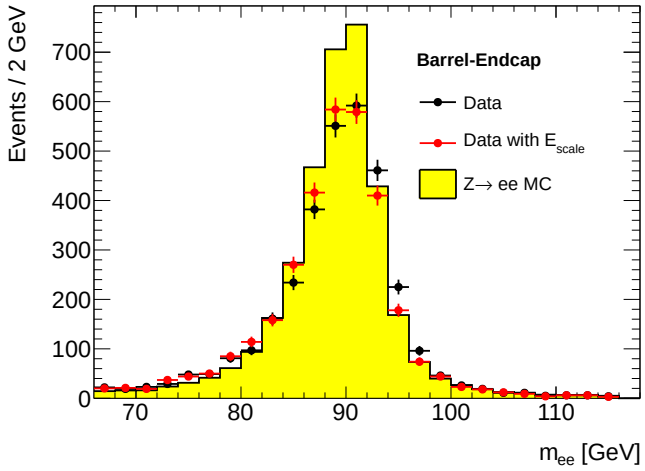

(b)

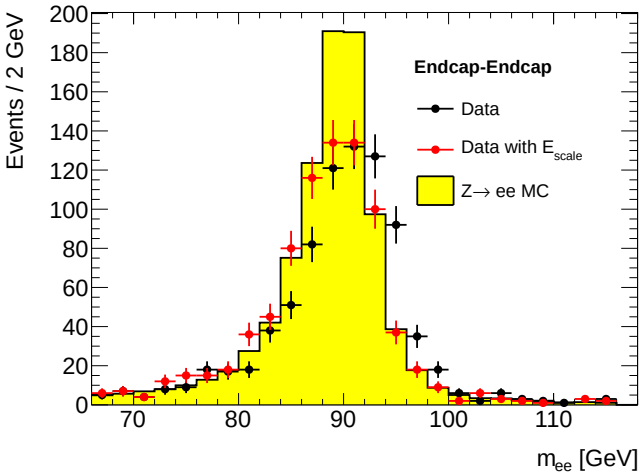

(c)

Figure 4.5: The invariant mass distributions before and after the energy scale correction in different regions: (a) barrel-barrel (b) barrel-endcap (c) endcap-endcap.

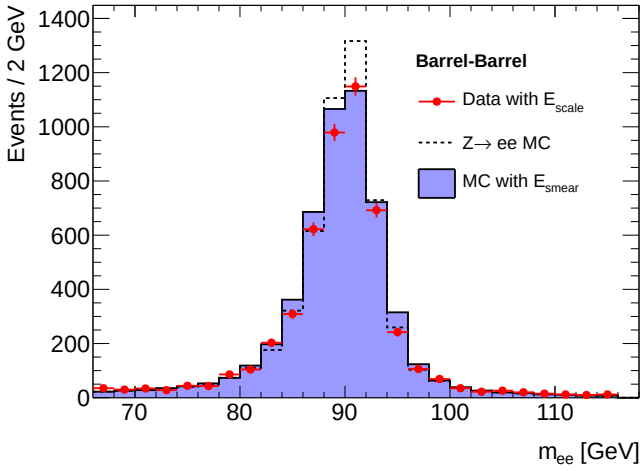

(a)

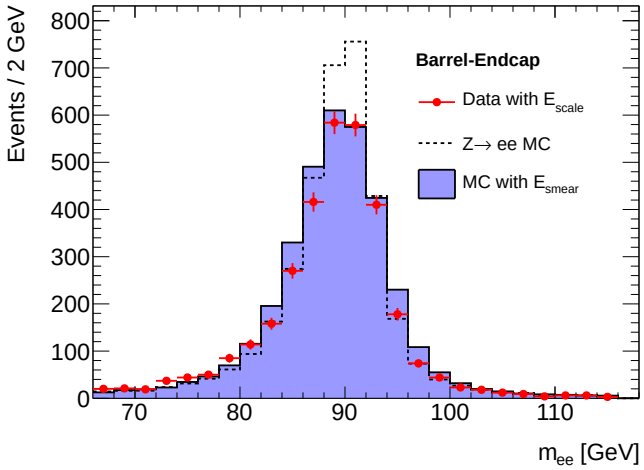

(b)

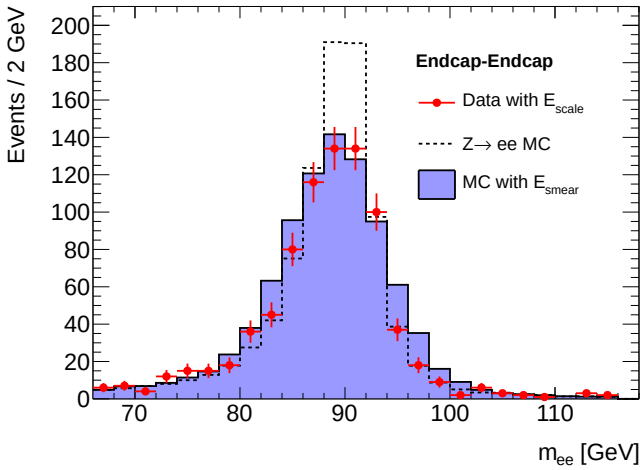

(c)

Figure 4.6: The invariant mass distributions before and after the energy smearing in different regions: (a) barrel-barrel (b) barrel-endcap (c) endcap-endcap.

CHAPTER V

p_T^{ee} Distribution

This chapter presents the observed di-electron transverse momentum distribution (p_T^{ee}[1]) from the $Z \to ee$ process. Section 5.1 and 5.2 summarize data and MC samples. Section 5.3 presents event selections applied to select $Z \to ee$ events. The binning of p_T^{ee} is studied in Section 5.4.

5.1 Data

As introduced in the previous chapter, the 2010 data are divided by periods from A to I corresponding to different LHC and ATLAS operating conditions. The luminosity information for each run is summarized in Table 5.1, 5.2 and 5.3. The lowest un-prescaled triggers are L1_EM14 for period A (152166) to E3 (160879), and EF_e15_medium for E4 (152347) to I (167776). The total recorded luminosity in 2010 is 35 pb^{-1} with a systematic uncertainty of 3.4% [33]. Since the normalized p_T^Z distribution is measured, the luminosity uncertainty only impacts the background estimation, which will be studied in the next chapter.

[1] In the following, p_T^Z stands for the Z boson transverse momentum at the truth level; p_T^{ee} stands for the Z boson transverse momentum at the reconstruction level.

RunNumber	Good LBs	Bad LBs	$L^{\text{Delivered}}$ (nb^{-1})	L^{LiveFrac} (nb^{-1})	L^{Prescale} (nb^{-1})	LiveFrac %	Prescale	Period
152166	95	0	0.01	0.01	0.01	99.94	1	A
152214	43	0	0.00	0.00	0.00	99.93	1	A
152221	163	0	0.02	0.02	0.02	99.93	1	A
152345	80	0	0.02	0.02	0.02	99.95	1	A
152409	590	0	0.08	0.08	0.08	99.84	1	A
152441	360	0	0.07	0.07	0.07	99.71	1	A
152508	66	0	0.01	0.01	0.01	99.94	1	A
152777	250	0	0.05	0.05	0.05	99.82	1	A
152844	56	0	0.01	0.01	0.01	99.93	1	A
152845	239	0	0.03	0.03	0.03	99.94	1	A
152878	115	0	0.02	0.02	0.02	99.85	1	A
152933	129	0	0.02	0.02	0.02	99.92	1	A
152994	60	0	0.01	0.01	0.01	99.92	1	A
153030	83	0	0.02	0.02	0.02	99.94	1	A
153134	43	0	0.01	0.01	0.01	99.57	1	A
153136	21	0	0.00	0.00	0.00	99.96	1	A
153159	90	0	0.01	0.01	0.01	99.86	1	A
153200	36	0	0.01	0.01	0.01	99.94	1	A
153565	893	0	0.77	0.76	0.76	99.85	1	B
154810	62	0	0.16	0.15	0.15	98.39	1	B
154813	128	0	0.27	0.26	0.26	98.73	1	B
154815	30	0	0.07	0.06	0.06	93.28	1	B
154817	279	0	0.54	0.53	0.53	99.28	1	B
155073	323	0	1.18	1.17	1.17	98.74	1	B
155112	474	0	3.47	3.41	3.41	98.43	1	B
155116	83	0	0.51	0.50	0.50	97.99	1	B
155160	263	0	1.33	1.33	1.33	99.57	1	B
155228	16	0	0.04	0.04	0.04	99.89	1	C
155280	16	0	0.15	0.03	0.03	18.47	1	C
155569	240	0	1.01	0.99	0.99	98.17	1	C
155634	186	0	1.05	1.05	1.05	99.57	1	C
155669	54	0	0.47	0.44	0.44	94.03	1	C
155678	68	0	1.20	1.19	1.19	99.31	1	C
155697	240	0	3.48	3.42	3.42	98.23	1	C
156682	105	0	1.30	1.30	1.30	99.84	1	C
158045	61	0	0.73	0.72	0.72	98.75	1	D
158116	413	0	14.50	14.44	14.44	99.60	1	D
158269	75	0	3.47	3.43	3.43	99.04	1	D
158299	71	0	1.34	1.34	1.34	99.73	1	D
158392	212	0	7.72	7.60	7.60	98.52	1	D
158443	22	0	1.11	1.09	1.09	98.15	1	D

Table 5.1: Run-number and luminosity information for 2010 data collected by the ATLAS detector.

RunNumber	Good LBs	Bad LBs	$L^{\text{Delivered}}$ (nb^{-1})	L^{LiveFrac} (nb^{-1})	L^{Prescale} (nb^{-1})	LiveFrac %	Prescale	Period
158466	16	0	1.62	1.62	1.62	99.94	1	D
158545	23	0	1.34	1.33	1.33	99.56	1	D
158548	196	0	10.88	10.08	10.08	92.67	1	D
158549	85	0	3.41	3.18	3.18	93.33	1	D
158582	307	0	16.13	16.09	16.09	99.70	1	D
158632	110	0	5.52	5.50	5.50	99.77	1	D
158801	177	0	7.18	7.16	7.16	99.83	1	D
158975	219	0	20.60	20.51	20.51	99.59	1	D
159041	259	0	25.72	25.64	25.64	99.71	1	D
159086	404	0	54.19	54.05	54.05	99.73	1	D
159113	256	0	28.10	28.04	28.04	99.77	1	D
159179	108	0	15.10	15.02	15.02	99.44	1	D
159202	81	0	9.88	9.80	9.80	99.15	1	D
159203	79	0	8.30	8.29	8.29	99.93	1	D
159224	539	0	64.79	64.30	64.30	99.24	1	D
160387	235	0	58.64	58.43	58.43	99.64	1	E
160472	366	0	76.84	76.34	76.34	99.35	1	E
160479	25	0	4.70	4.70	4.70	99.88	1	E
160530	424	0	96.22	92.45	92.45	96.09	1	E
160613	189	0	48.56	48.03	48.03	98.90	1	E
160736	59	0	17.38	17.16	17.16	98.71	1	E
160800	61	1	18.69	16.13	16.13	86.29	1	E
160801	370	0	79.22	75.79	75.79	95.66	1	E
160879	409	0	81.25	80.62	80.62	99.22	1	E
160899	15	0	4.81	4.81	4.81	99.86	1	E
160953	53	0	21.87	19.41	19.41	88.74	1	E
160954	62	1	17.08	16.63	16.63	97.36	1	E
160958	195	0	41.41	40.63	40.63	98.12	1	E
160963	13	0	2.34	2.33	2.33	99.88	1	E
160975	22	0	6.89	4.48	4.48	64.98	1	E
160980	30	0	8.99	8.99	8.99	99.90	1	E
161118	97	0	34.08	34.04	34.04	99.90	1	E
161379	357	0	96.09	95.89	95.89	99.79	1	E
161407	102	0	40.43	40.39	40.39	99.92	1	E
161520	351	0	113.95	113.86	113.86	99.92	1	E
161562	221	0	72.78	72.33	72.33	99.37	1	E
161948	352	0	90.50	89.08	89.08	98.43	1	E
162347	408	0	219.21	216.75	216.75	98.88	1	F
162526	360	0	253.51	252.41	252.41	99.56	1	F
162576	48	0	39.78	38.16	38.16	95.95	1	F

Table 5.2: Run-number and luminosity information for 2010 data collected by the ATLAS detector.

RunNumber	Good LBs	Bad LBs	$L^{\text{Delivered}}$ (nb^{-1})	L^{LiveFrac} (nb^{-1})	L^{Prescale} (nb^{-1})	LiveFrac %	Prescale	Period
162577	9	0	6.49	6.42	6.42	98.92	1	F
162620	66	0	70.33	67.14	67.14	95.46	1	F
162623	322	0	240.47	234.77	234.77	97.63	1	F
162690	349	0	323.02	321.43	321.43	99.51	1	F
162764	77	0	83.54	79.78	79.78	95.50	1	F
162843	379	0	307.55	306.28	306.28	99.59	1	F
162882	321	0	294.43	293.15	293.15	99.57	1	F
165591	366	2	148.82	147.94	147.54	99.41	1	G
165632	367	0	584.45	534.57	534.57	91.47	1	G
165703	42	0	87.85	87.52	87.52	99.62	1	G
165732	360	0	911.96	902.98	902.98	99.02	1	G
165767	329	0	936.79	922.98	922.98	98.53	1	G
165815	42	0	168.14	165.07	165.07	98.18	1	G
165817	2	2	9.67	5.63	0.22	58.19	1	G
165818	79	0	277.43	220.71	220.71	79.56	1	G
165821	73	0	228.72	214.15	214.15	93.63	1	G
165954	36	0	186.01	151.72	151.72	81.56	1	G
165956	18	0	92.82	90.65	90.65	97.67	1	G
166097	48	0	233.37	231.13	231.13	99.04	1	G
166142	140	0	688.46	671.78	671.78	97.58	1	G
166143	58	0	264.03	258.60	258.60	97.94	1	G
166198	351	0	1288.56	1213.71	1213.71	94.19	1	G
166305	23	0	180.50	179.73	179.73	99.58	1	G
166383	136	0	962.37	949.89	949.89	98.70	1	G
166466	156	0	1343.89	1307.19	1307.20	97.27	1	H
166658	250	0	2034.53	1952.75	1952.75	95.98	1	H
166786	233	0	1872.66	1863.33	1863.33	99.50	1	H
166850	157	2	6.79	6.46	6.46	95.07	1	H
166856	19	0	297.91	293.83	293.83	98.63	1	H
166924	150	0	1223.42	1218.51	1218.51	99.60	1	H
166927	89	2	557.83	556.05	544.93	99.68	1	H
166964	11	0	153.98	147.43	147.43	95.74	1	H
167575	8	0	73.38	37.72	37.72	51.40	1	I
167576	269	0	3524.18	3504.65	3504.65	99.45	1	I
167607	313	0	5228.70	5000.80	5000.80	95.64	1	I
167661	65	0	1327.27	1283.98	1283.98	96.74	1	I
167680	223	0	3647.86	3518.54	3518.53	96.45	1	I
167776	408	0	5866.40	5806.87	5806.87	98.99	1	I

Table 5.3: Run-number and luminosity information for 2010 data collected by the ATLAS detector.

Generator	Dataset ID	Process		Pileup	σ (nb)
		Signal			
Pythia	106046	$Z \to ee$	LO	x	0.99
Pythia	106046	$Z \to ee$	LO, Extra-material	x	0.99
Mc@nlo	106087	$Z \to ee$	LO+NLO	-	0.99
		Backgrounds			
Pythia	105802	Dijet, $p_{T,j} > 15$ GeV	LO	x	$9.8 \cdot 10^4$
Pythia	106043	$W \to e\nu$	LO	x	10.46
Pythia	106052	$Z \to \tau\tau$	LO	x	0.99
Pythia	107054	$W \to \tau\nu$	LO	x	0.99
Mc@nlo	105200	$t\bar{t}$	LO+NLO	x	0.16

Table 5.4: MC samples used for the $Z \to ee$ study. "x" means the pileup effect is implemented in the simulation, while "-" means the sample is generated without pileup effect.

5.2 Monte Carlo

A set of MC samples is used to simulate the signal and backgrounds. MC samples are overlaid with minimum bias interactions to account for multiple interactions per bunch crossing. The MC events were generated with Pythia, Mc@nlo and passed through the full Geant4-based [34] detector simulation. Table 5.4 summarizes the datasets for the signal and background processes.

MC events are generated with one pile-up configuration with in-time pile-up corresponding to an average of two interactions. However, the pile-up situations are different in each data taking period. So the distribution of the MC primary vertex multiplicity is reweighted to data in each period after trigger and Good Runs List (GRL) selections. The luminosity-dependent average weight is applied to the MC event weight. The primary vertex multiplicity and pile-up weight for each period are shown in Figure 5.1(a) and 5.1(b).

5.3 Event Selections

In order to select events from stable proton-proton collisions with the detector functioning nominally, a set of event level cuts are applied: GRL, primary vertex,

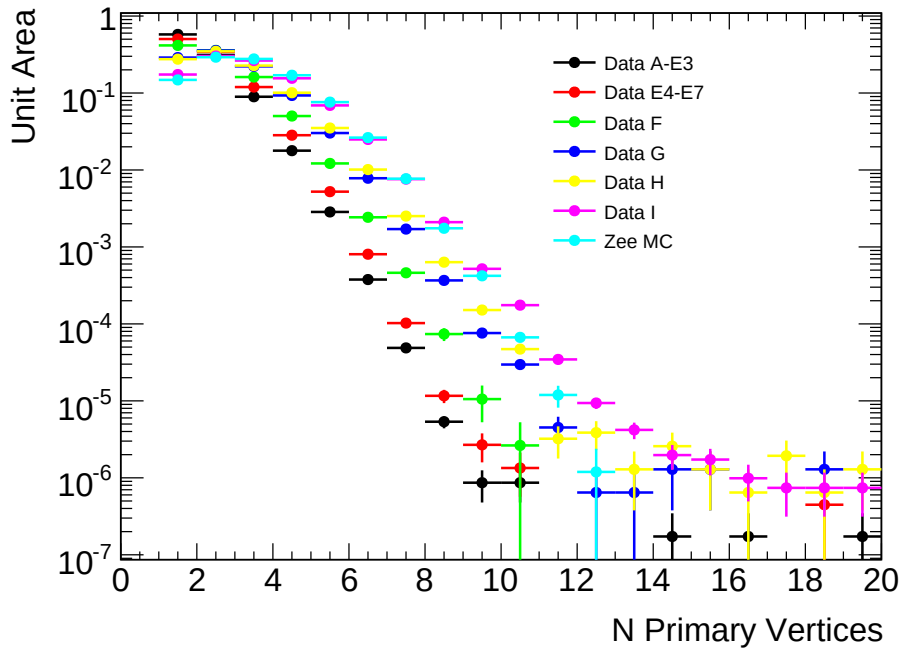

(a)

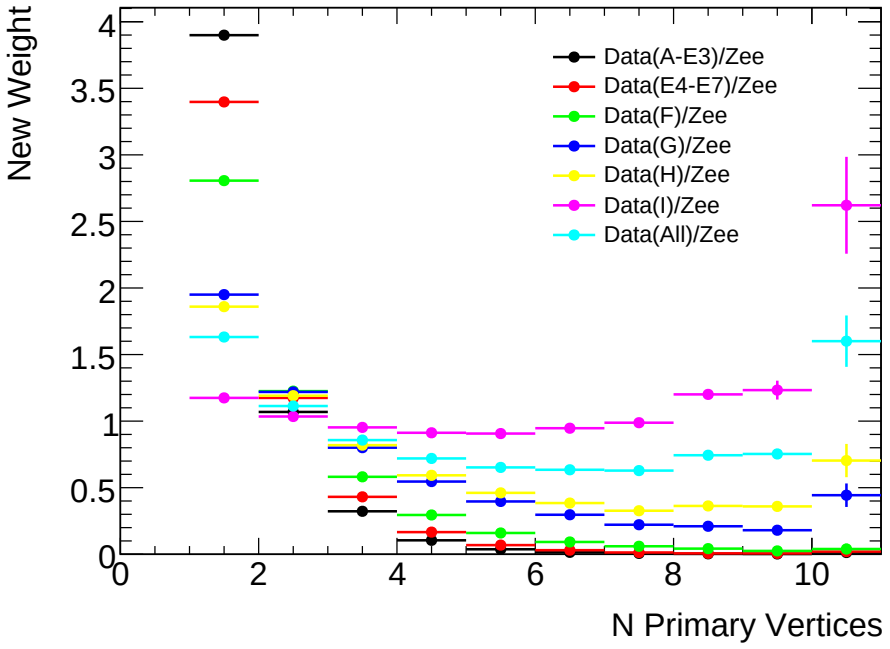

(b)

Figure 5.1: (a) Primary vertex multiplicity distributions for each period and the PYTHIA MC. (b) Pile-up weight for each period.

N PV	A-D	E	F	G	H	I	Average
1	3.8991 ± 0.0113	3.3976 ± 0.0102	2.8065 ± 0.0107	1.9503 ± 0.0063	1.8599 ± 0.0060	1.1745 ± 0.0036	1.6317 ± 0.0026
2	1.0689 ± 0.0023	1.1743 ± 0.0027	1.2253 ± 0.0041	1.2193 ± 0.0030	1.1911 ± 0.0029	1.0347 ± 0.0023	1.1134 ± 0.0015
3	0.3226 ± 0.0008	0.4311 ± 0.0012	0.5816 ± 0.0026	0.8006 ± 0.0021	0.8195 ± 0.0022	0.9529 ± 0.0022	0.8575 ± 0.0013
4	0.1047 ± 0.0004	0.1662 ± 0.0008	0.2950 ± 0.0023	0.5460 ± 0.0020	0.5929 ± 0.0022	0.9124 ± 0.0027	0.7197 ± 0.0015
5	0.0374 ± 0.0003	0.0687 ± 0.0007	0.1598 ± 0.0024	0.3966 ± 0.0024	0.4611 ± 0.0027	0.9066 ± 0.0040	0.6523 ± 0.0022
6	0.0143 ± 0.0003	0.0305 ± 0.0007	0.0922 ± 0.0031	0.2966 ± 0.0034	0.3845 ± 0.0040	0.9467 ± 0.0070	0.6345 ± 0.0038
7	0.0063 ± 0.0004	0.0133 ± 0.0009	0.0600 ± 0.0046	0.2217 ± 0.0051	0.3270 ± 0.0066	0.9881 ± 0.0135	0.6284 ± 0.0073
8	0.0031 ± 0.0006	0.0067 ± 0.0013	0.0422 ± 0.0081	0.2102 ± 0.0104	0.3628 ± 0.0150	1.2008 ± 0.0340	0.7438 ± 0.0182
9	0.0021 ± 0.0009	0.0064 ± 0.0026	0.0250 ± 0.0126	0.1805 ± 0.0192	0.3594 ± 0.0303	1.2329 ± 0.0709	0.7534 ± 0.0378
10	0.0129 ± 0.0060	0.0201 ± 0.0119	0.0394 ± 0.0398	0.4436 ± 0.0883	0.7037 ± 0.1250	2.6213 ± 0.3638	1.6006 ± 0.1929

Table 5.5: The pileup weight as a function of the number of primary vertex (NPV) for each period and the average weight applied on the MC.

trigger, and OTX cleaning. Then, the electron quality, the di-electron charge and invariant mass cuts are applied to select final $Z \to ee$ candidates.

- Collision event selections:
  - Stable, colliding beams; solenoid, toroid, calorimeters, and inner detector were fully operational (GRL);
  - At least one primary vertex;
  - The primary vertex with largest $\sum_{\text{trk}} p_{\text{T}}$ has at least three tracks;
  - Trigger requirement(period dependent):
    - L1_EM14 for period A to E3;
    - EF_e15_medium for period E to I.
  - OTX cleaning.
- Electron selections (for both electrons):
  - the electron is found by the sliding window algorithm (electron author is 1 or 3);
  - The transverse energy of the electron measured by the calorimeter: $E_T^{\text{cluster}} > 20$ GeV;
  - The pseudo rapidity measured by the calorimeter $|\eta^{\text{cluster}}| < 2.4$ and not in $[1.37, 1.52]$;

Selection	Data	$Z \to ee$	Backgrounds
Trigger	13350533	28206 ± 33	1293680512 ± 409289
Author	6147198	21144 ± 28	594139776 ± 277393
$\|\eta\| < 2.4$	5588117	18772 ± 26	542553728 ± 265078
OTX Clean	329812	11387 ± 20	5325860 ± 26251
Medium Electron	10251	9436 ± 19	890 ± 317
$m_{ee} \in [66, 116]$ GeV	9281	9160 ± 19	296 ± 183
Opposite Charge	8916	8905 ± 19	158 ± 129

Table 5.6: Cutflow comparison between data and Monte Carlo simulations. The number of events from the data are approximately equal to the sum of the simulated $Z \to ee$ and backgrounds.

Selection	Dijet	$t\bar{t}$	$W \to e\nu$	$Z \to \tau\tau$
Trigger	1391687168 ± 440429	3109 ± 4	354430 ± 134	33600 ± 24
Author	639253504 ± 298498	3065 ± 4	69298 ± 59	11667 ± 14
$\|\eta\| < 2.4$	583752448 ± 285246	3039 ± 4	61477 ± 56	10391 ± 13
OTX Clean	5724755 ± 28248	1090 ± 2	4189 ± 15	587 ± 3
Medium Electron	836 ± 341	36 ± 0	50 ± 2	27 ± 1
$m_{ee} \in [66, 116]$ GeV	279 ± 197	13 ± 0	17 ± 1	7 ± 0
Opposite Charge	139 ± 139	12 ± 0	10 ± 1	6 ± 0

Table 5.7: Cutflow of $Z \to ee$ backgrounds estimated by Monte Carlo simulations.

  - The electrons is at least "medium".

- $Z \to ee$ selection:

  - Exactly two such electrons and no additional medium electrons;

  - The electrons are oppositely charged;

  - The invariant mass of the electron-positron pair is with the Z mass window $66 < m_{\mathrm{ee}} < 116$ GeV.

The distributions of the leading electron transverse energy and invariant mass of electron-positron pairs after the final selection are shown in Figure 5.2.

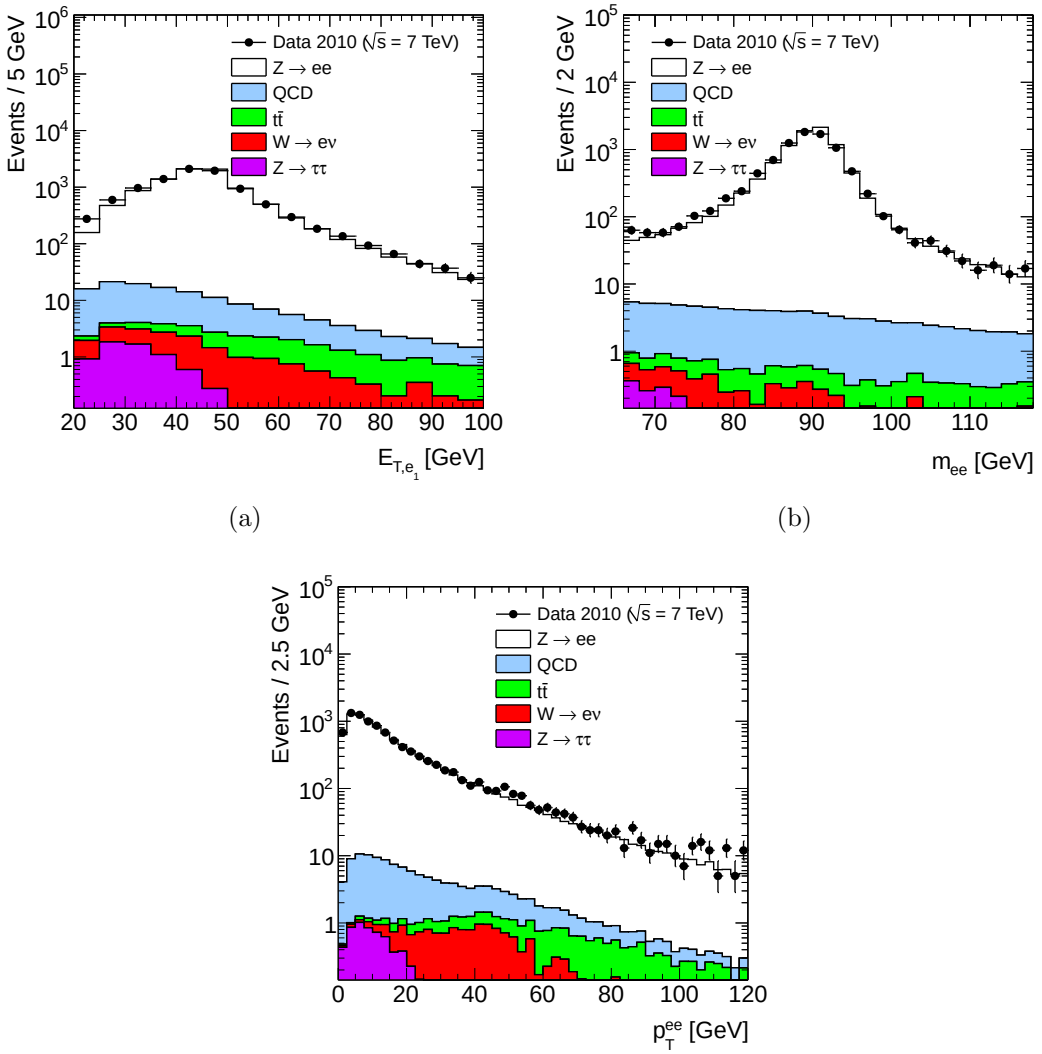

(a) (b)

(c)

Figure 5.2: Distributions of electron-positron pairs after the final selection: (a) the leading electron transverse momentum E_{T,e_1} (b) the invariant mass m_{ee} (c) the transverse momentum p_T^{ee}

5.4 The Binning of p_T^{ee}

For candidates passing the final selection, the reconstructed p_T^{ee} and true Z boson transverse momentum p_T^Z are different due to the detector resolution. The bin purity is used to study this effect, which is defined as the probability of an event remaining in the same bin after reconstruction

$$\text{Purity of bin } i = \frac{\text{Reconstructed and true } p_T \text{ in bin } i}{\text{True } p_T \text{ in bin } i}. \tag{5.1}$$

On one hand, the bin size should be compatible with the electron energy resolution otherwise the measurement would suffer a large systematic uncertainty from simulating the migration effect. On the other hand, the bin size is also constrained by the statistical uncertainty. Thus, a binning set with 19 bins between 0 and 350 GeV is used in this analysis: (0, 3, 6, 9, 12, 15, 18, 21, 24, 27, 30, 36, 42, 48, 54, 60, 80, 100, 180, 350) GeV. The purity of each bin is always over 60% as shown in the Figure 5.3. The bin purities from Pythia and Mc@nlo have a very good agreement.

Table 5.8 summarizes data candidates in each bin with different electron energy scale corrections as introduced in Section 4.4. Events with p_T^{ee} beyond 350 GeV are ignored in this analysis. Among all $Z \to ee$ candidates in data, there is only one event with $p_T^{ee} > 350$ (= 358) GeV.

The p_T^{ee} distribution shown in Figure 5.2(c) is re-calculated with the chosen binning set, as shown in Figure 5.4.

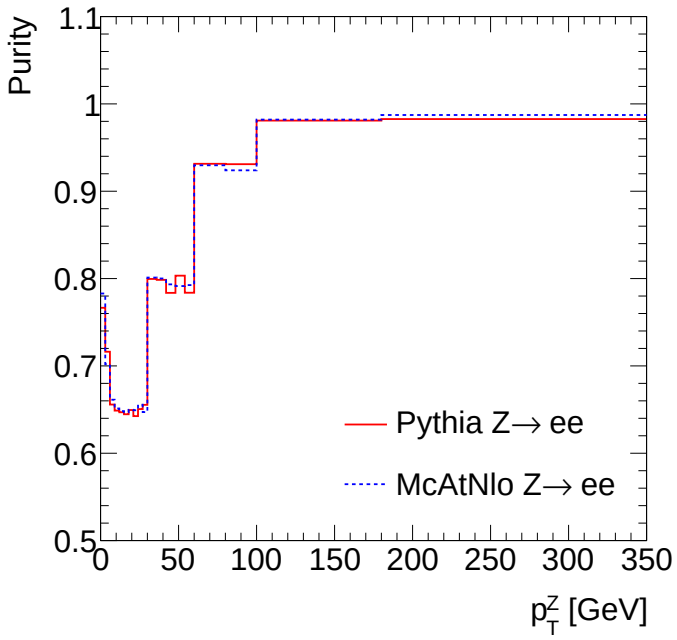

Figure 5.3: The purity of each bin for p_T^Z measurements. PYTHIA and MC@NLO $Z \to ee$ samples predict consistent bin purities.

p_T (GeV)	Data	stat.	+ energy correction	+ scale uncertainty	- scale uncertainty
0 – 3	829	29	837	846	809
3 – 6	1525	39	1514	1508	1508
6 – 9	1286	36	1280	1298	1269
9 – 12	969	31	964	966	989
12 – 15	813	29	815	800	798
15 – 18	577	24	570	569	595
18 – 21	463	22	458	449	463
21 – 24	347	19	360	356	365
24 – 27	290	17	285	274	293
27 – 30	263	16	271	258	269
30 – 36	378	19	381	377	390
36 – 42	265	16	257	249	277
42 – 48	195	14	191	196	194
48 – 54	162	13	168	156	165
54 – 60	113	11	113	107	123
60 – 80	206	14	210	199	219
80 –100	104	10	100	98	107
100–180	125	11	129	122	130
180–350	12	3.5	12	11	12

Table 5.8: Number of data candidates in each bin with different corrections of electron energy scales.

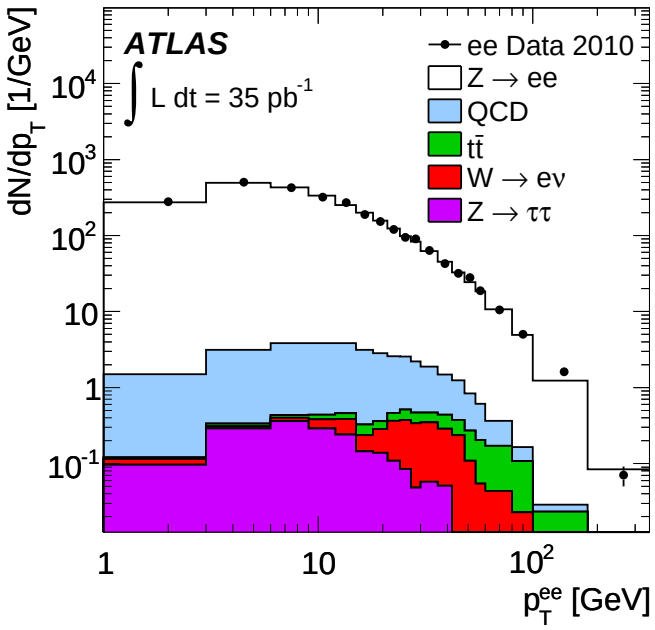

Figure 5.4: p_T^{ee} distribution after the final selection with the bin width correction applied. The background estimations are presented in detail in the next chapter.

CHAPTER VI

Backgrounds

Backgrounds for $Z \to ee$ are loosely divided into two categories. The first category is usually named as the "electroweak" background, which contains at least one real high E_T electron from W or Z boson decays. Section 6.1 presents the estimation of electroweak backgrounds. The second category is "QCD" background which arises mostly from misidentification of jets as good quality electrons in the $pp \to jj$ (di-jet) process. The cross-section of the QCD process is huge and suffers significant uncertainties. Therefore, the estimation of QCD background requires data-driven methods.

For the measurement of the p_T^Z distribution, not only the total number (or the normalization) but also the shape of the QCD background must be extracted. Section 6.2 presents two data-driven methods to extract the normalization of the QCD background, while Section 6.3 presents the shape estimation in the same bin set defined in Section 5.4. Finally, the QCD background along with electroweak backgrounds are summarized in Section 6.4.

6.1 Electroweak Backgrounds

Dominant electroweak backgrounds are from $W \to e\nu$ and $Z \to \tau\tau$ processes, as well as the top pair ($t\bar{t}$) production in which either one or both W bosons decay

into electrons. These backgrounds are estimated using MC samples as introduced in Section 5.2. Their uncertainties are mainly from limited statistics in each bin and theoretical cross-section uncertainties. As studied in the inclusive W/Z cross-section measurement [11], the cross-section uncertainties for W, Z and $t\bar{t}$ processes are 5%, 6% and 7%, respectively. The luminosity uncertainty of 3.4% is also added in quadrature to cross-section uncertainties.

6.2 The QCD Background Normalization

The QCD process has different di-electron invariant mass and electron isolation distributions from those of the $Z \to ee$ process. Therefore, the first data-driven method uses the invariant mass distribution to estimate the QCD background normalization, while the second one uses the isolation distribution.

6.2.1 Fit m_{ee}

In principle, one can directly fit the well-known Z boson line-shape to extract the QCD background in the signal region. However, it does not give a reliable result due to the low statistics of the QCD background in the signal region. The first data-driven method selects a control sample by loosening the electron identification so that the QCD contribution is enhanced. Then, $Z \to ee$ and QCD background invariant mass templates are made to fit the data distribution to extract the QCD contribution, $(N_{\mathrm{QCD}}^{\mathrm{ctrl.}})$. In the end, a scale factor (SF) is applied to extrapolate the number of QCD events from the control region to the signal region $(N_{\mathrm{QCD}}^{\mathrm{est.sig.}})$

$$N_{\mathrm{QCD}}^{\mathrm{est.sig.}} = N_{\mathrm{QCD}}^{\mathrm{ctrl.}} \times SF. \tag{6.1}$$

The extrapolation scale factor, SF can be estimated from another control region made of events with only one medium electron and a small missing transverse mo-

mentum, $E_T^{miss} < 15$ GeV. Due to the E_T^{miss} cut, events from the $W \to e\nu$ process with an escaping neutrino are reduced. Therefore, events from the QCD process with one misidentified electron dominate this control region.

6.2.1.1 Electrons with Different Qualities

In this section, electron pairs with different qualities are used in the QCD background estimation:

- cand-cand: two reconstructed electrons without relaxing any identification requirement;
- cand-loose: one electron is at least loose;
- cand-medium: one electron is at least medium;
- loose-medium: one electron is medium and the other electron is at least loose;
- medium-medium: both electrons are medium;
- tight-tight: both electrons are tight;
- medium-non-medium: one electron is medium and the other electron is not medium.

The variables used to estimate the QCD normalization in the signal regions are

- $\varepsilon^{\text{medium}}_{\text{loose,QCD}}$: the probability of one loose electron passing the medium selection in the QCD process;
- $N^{\text{loose}-\text{loose}}_{\text{QCD}}$: the number of QCD events with two loose electrons in which the loose electron could also be medium;
- $N^{\text{loose}-\text{medium}}_{\text{QCD}}$ or $N^{\text{ctrl.}}_{\text{QCD}}$: the number of QCD events with one loose and one medium electrons, in which the loose electron could also be medium;

- $N_{\rm QCD}^{\rm medium-medium}$ or $N_{\rm QCD}^{\rm est.sig.}$: the number of QCD events with two medium electrons.

Then $\varepsilon_{\rm loose,QCD}^{\rm medium}$, $N_{\rm QCD}^{\rm loose-loose}$, $N_{\rm QCD}^{\rm loose-medium}$ and $N_{\rm QCD}^{\rm medium-medium}$ will satisfy the following equations

$$N_{\rm QCD}^{\rm loose-loose} \times 2\varepsilon_{\rm loose,QCD}^{\rm medium}(1-\varepsilon_{\rm loose,QCD}^{\rm medium}) = N_{\rm QCD}^{\rm loose-medium} - N_{\rm QCD}^{\rm medium-medium}; \quad (6.2)$$

$$N_{\rm QCD}^{\rm loose-loose} \times (\varepsilon_{\rm loose,QCD}^{\rm medium})^2 = N_{\rm QCD}^{\rm medium-medium}. \quad (6.3)$$

Re-write $N_{\rm QCD}^{\rm medium-medium}$ in terms of $\varepsilon_{\rm loose,QCD}^{\rm medium}$ and $N_{\rm QCD}^{\rm loose-medium}$

$$N_{\rm QCD}^{\rm medium-medium} = N_{\rm QCD}^{\rm loose-medium} \times \varepsilon_{\rm loose,QCD}^{\rm medium}/(2-\varepsilon_{\rm loose,QCD}^{\rm medium}). \quad (6.4)$$

Comparing Equation 6.4 to Equation 6.1, the extrapolation scale factor SF can be written in terms of $\varepsilon_{\rm loose,QCD}^{\rm medium}$

$$SF = \varepsilon_{\rm loose,QCD}^{\rm medium}/(2-\varepsilon_{\rm loose,QCD}^{\rm medium}). \quad (6.5)$$

6.2.1.2 The QCD Background Composition

The QCD background consists of three main components: light hadron fakes, photon conversions and heavy quark (b or c) decays. The $\varepsilon_{\rm loose,QCD}^{\rm medium}$ of the three components are different. Contributions from three sources may vary with electron qualities. QCD compositions in the control region and signal region should be close since the $\varepsilon_{\rm loose,QCD}^{\rm medium}$ estimated from the single electron sample will be used in the di-electron sample. From a large MC sample with 100 M events, the loose and medium electrons from the QCD process have similar compositions as shown in Figure 6.1. So the extrapolation scale factor from loose-medium pairs to medium-medium pair is reliable.

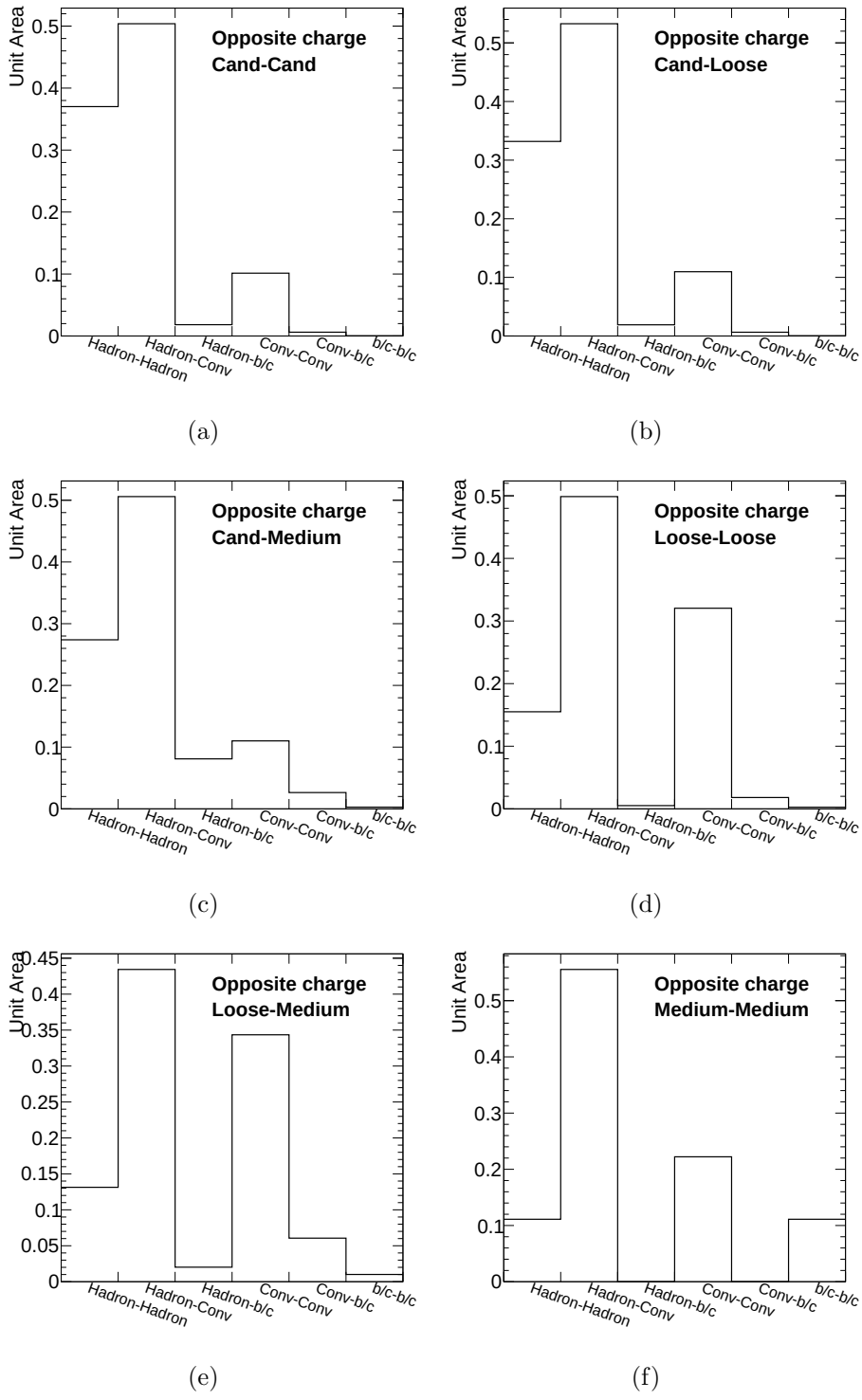

Figure 6.1: MC fake electron compositions for electron pairs with different electron quality. The composition of the fakes in the loose-loose sample (d) and the composition of the fakes in the medium-medium sample (f) can be seen to be similar.

6.2.1.3 Estimate $N_{\rm QCD}^{\rm loose-medium}$

To extract $N_{\rm QCD}^{\rm loose-medium}$, signal and background templates are fit to the di-electron invariant mass distribution within $50 < m_{\rm ee} < 130$ GeV. To increase statistics of the QCD background, the mass window of the fit is wider than that used in the event selection ($66 < m_{\rm ee} < 116$ GeV). The signal template is composed of a Breit-Wigner form convolved with a Gaussian. The background template is modeled with a second order polynomial function. The fit result is shown in Figure 6.2(a). In the mass window $66 < m_{\rm ee} < 116$ GeV, a background of $N_{\rm QCD}^{\rm loose-medium} = 1662 \pm 80$(stat) is determined.

The fits were performed with different bin sizes and different fit ranges. The results are listed in Table 6.1. The largest difference is 52 ($= |1714 - 1662|$) which is considered as the bin size and fit range systematic uncertainties.

In addition to the QCD background, the fit could also contain the electroweak backgrounds and Drell-Yan events, which are treated as systematic uncertainties. The electroweak contamination is estimated from MC to be $N_{\rm EW}^{\rm loose\text{-}medium} = 135 \pm 5$(stat) events with 5% systematic uncertainty from the cross-section uncertainties. Since the medium electron charge mis-identification rate is around 3% [35], and Drell-Yan contribution with $66 < m_{ee} < 116$ GeV is about 2%, the number of same-charge Drell-Yan events is negligible compared to those from Z and QCD processes.

In the QCD process, the asymmetry of same-charge and opposite-charge pairs, is caused by heavy flavor $b\bar{b}/c\bar{c}$ decay. In the electron channel, the dominant fraction of the QCD background is from light flavor hadrons and photon conversions. This results in a negligible asymmetry between same-charge and opposite-charge events. Therefore, the Drell-Yan contribution is determined from the difference between fits to the invariant mass distribution of same-charge and opposite-charge pairs. The Drell-Yan contribution is estimated to be $N_{\rm Drell-Yan}^{\rm loose\text{-}medium} = 148$. So the fit contamination is estimated to be 200 ($= \sqrt{135^2 + 148^2}$).

$N_{QCD}^{loose-medium}$	1 GeV bin		2 GeV bin	
fit range	opposite-sign	same-sign	opposite-sign	same-sign
$[50, 130]$ GeV	1662 ± 80	1514 ± 30	1656 ± 79	1527 ± 30
$[66, 116]$ GeV	1714 ± 134	1548 ± 65	1701 ± 158	1551 ± 65
$[60, 140]$ GeV	1678 ± 85	1521 ± 32	1643 ± 96	1508 ± 32

Table 6.1: Estimation of $N_{\rm QCD}^{\rm loose-medium}$ using different bin sizes, fit ranges, and the invariant mass distribution of same-sign and opposite-sign electron-positron pairs.

In summary, the QCD background normalization in the loose-medium control region is

$$N_{\rm QCD}^{\text{loose-medium}} = 1662 \pm 80(\text{stat}) \pm 207(\text{syst}), \tag{6.6}$$

in which the systematic uncertainty is a quadratic sum of two terms as discussed above, $207 = \sqrt{52^2 + 200^2}$.

6.2.1.4 Estimate $\varepsilon_{\rm loose,QCD}^{\rm medium}$

The probability of a loose electron from jet misidentification passing the medium selection, $\varepsilon_{\rm loose,QCD}^{\rm medium}$ is determined from the control sample made of single electron plus small transverse missing energy (< 20 GeV). This control sample is dominated by a QCD process in which one jet is misidentified as an electron. This efficiency is shown in Figure 6.2(b) as a function of E_T and η. The average value amounts to $\bar{\varepsilon}_{\rm loose,QCD}^{\rm medium} = 0.122$ with a negligible statistical uncertainty. From the MC simulation, the average value is $\bar{\varepsilon}_{\rm loose,QCD,MC}^{\rm medium} = 0.126 \pm 0.001(\text{stat.})$. The difference between data and MC is assigned as a systematic uncertainty.

There is a bias if the average value rather than the efficiency map is used to extrapolate the QCD background normalization. Therefore, a QCD MC sample with large statistics (100 M) is used to study this bias and the estimations of the QCD background are summarized in Table 6.2. The results from using the map and using

Charge	$N_{\mathrm{QCD,MC}}^{\mathrm{medium-medium}}$	
	use the map	use the average
Opposite Sign	104.4 ± 4.8	95.8 ± 4.4
Same Sign	106.7 ± 4.8	100.9 ± 4.6

Table 6.2: Estimated $N_{\mathrm{QCD,MC}}^{\mathrm{medium-medium}}$ from the MC simulation. The results from using the efficiency map and average efficiency are 10% different.

the average value differ by 10% which is assigned as another systematic uncertainty to $\bar{\varepsilon}_{\mathrm{loose,QCD}}^{\mathrm{medium}}$. In summary:

$$\bar{\varepsilon}_{\mathrm{loose,QCD}}^{\mathrm{medium}} = 0.122 \pm 0.012(\mathrm{syst}) \tag{6.7}$$

6.2.1.5 Summary of $N_{\mathrm{QCD}}^{\mathrm{medium-medium}}$

After substituting Equation 6.6 and 6.7 into 6.4, it yields $N_{\mathrm{QCD}}^{\mathrm{medium-medium}} = 108.0 \pm 5.2(\mathrm{stat}) \pm 17.1(\mathrm{syst})$.

For a further cross-check, the "loose" is modified to "loose+SiCut", in which "SiCut" requires the track of the electron to have at least 7 hits in silicon trackers. The background fit for the "looseSiCut-medium" pairs is $N_{\mathrm{QCD}}^{\mathrm{looseSiCut\text{-}medium}} = 1037 \pm 56(\mathrm{stat})$. The $\bar{\varepsilon}_{\mathrm{loose,QCD}}^{\mathrm{medium}}$ is also changed to $\bar{\varepsilon}_{\mathrm{looseSiCut,QCD}}^{\mathrm{medium}} = 0.255 \pm 0.000(\mathrm{stat})$. So the estimated medium-medium QCD background event number is $N_{\mathrm{QCD}}^{\mathrm{medium-medium}} = 151.5 \pm 8.2(\mathrm{stat})$. The difference between QCD background estimations from using the loose and loose+SiCut criteria is quoted as an additional systematic uncertainty, which is around 50%.

In summary, the final total QCD background is

$$N_{\mathrm{QCD}}^{\mathrm{medium-medium}} = 108.0 \pm 5.2(\mathrm{stat}) \pm 56.6(\mathrm{syst}). \tag{6.8}$$

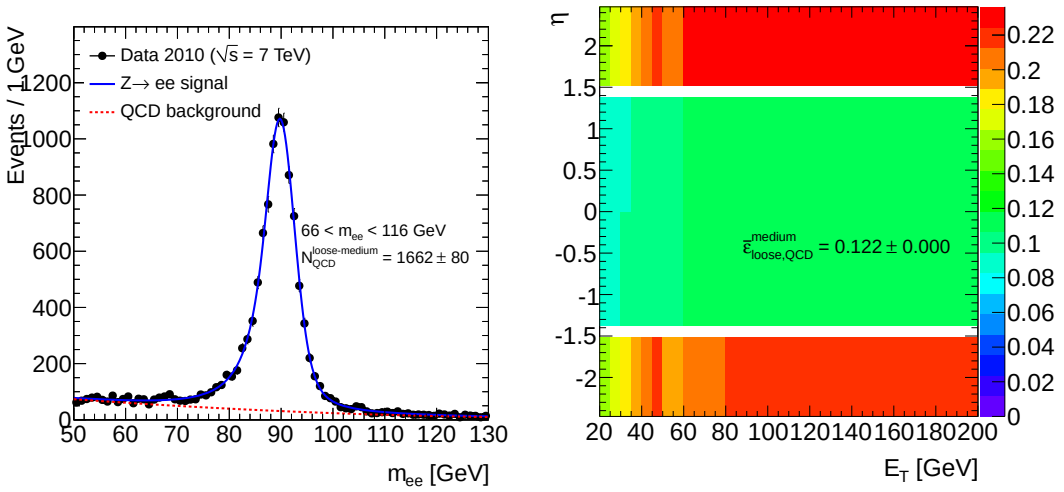

(a) (b)

Figure 6.2: (a) Invariant mass fit of loose-medium electron-positron pairs. (b) The probability of an misidentified loose electron passing the medium selection in the QCD process with negligible statistical uncertainty.

6.2.2 Fit Electron Isolation Variables

In the second method, the QCD normalization is determined from a template fit of the electron isolation variable in the signal region. Due to the limited statistics, the fit suffers from a large statistical uncertainty. It is therefore used as a cross-check of the result from the first method. Two calorimeter based isolation variables are used. One variable is "ETCone30", which is the energy deposit in the EM calorimeter around the electron within a cone of $\Delta R < 0.3$, of the sub-leading electron divided by its E_T. The second discriminating variable is the difference between isolation variable ETCone30 of two electrons divided by the sum of their E_T.

The $Z \rightarrow ee$ template is taken from a sample of tight-tight electron-positron pairs in a smaller invariant mass window $80 < m_{ee} < 100$ GeV. Similarly, the QCD background in this sample can be estimated by extrapolating medium-medium electron pairs to tight-tight ones. The scale factor $\bar{\varepsilon}^{\text{tight}}_{\text{medium,QCD}}$ is estimated from the same control sample which was previously used to estimate $\bar{\varepsilon}^{\text{medium}}_{\text{loose,QCD}}$. A value of $\bar{\varepsilon}^{\text{tight}}_{\text{medium,QCD}} = 0.13 \pm 0.02(\text{stat})$ is found. Therefore, the QCD background is esti-

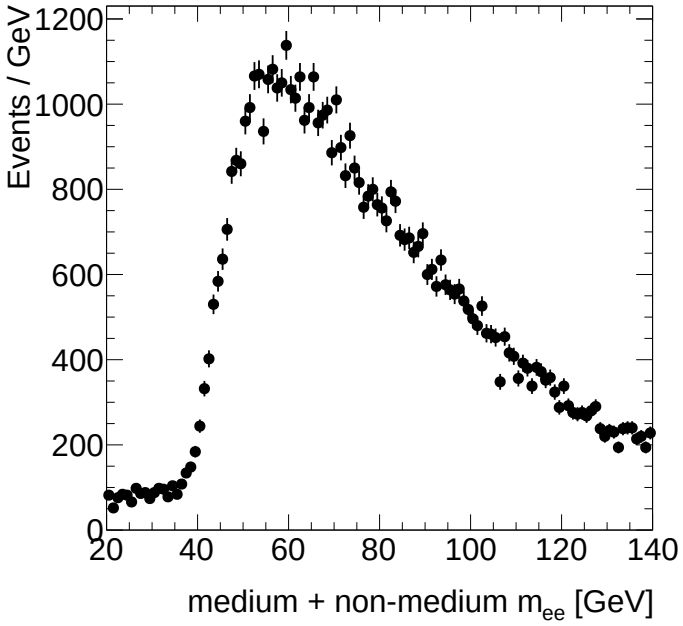

Figure 6.3: Invariant mass distribution of medium-non-medium pairs used to determine the QCD background shape.

mated to be about 0.1% of the $Z \to ee$ process, which is negligible.

The QCD template is built from a sample where the $Z \to ee$ process is negligible. Such a sample can be constructed by reversing the medium electron identification selection for either electron or positron, *i.e.* selecting medium-non-medium pairs with invariant masses $m_{ee} < 66$ GeV or $m_{ee} > 116$ GeV. The invariant mass distribution of medium-non-medium pairs are shown in Figure 6.3, in which the Z resonance peak is negligible compared to the QCD contribution.

After subtracting the electroweak backgrounds from data using MC samples, two fits with different discriminating variables are shown in Figure 6.4(a) and 6.4(b), respectively. The resulting normalization of the QCD background are 89.4 ± 30.2(stat) and 96.6 ± 22.0(stat). They are consistent with the result from the first method.

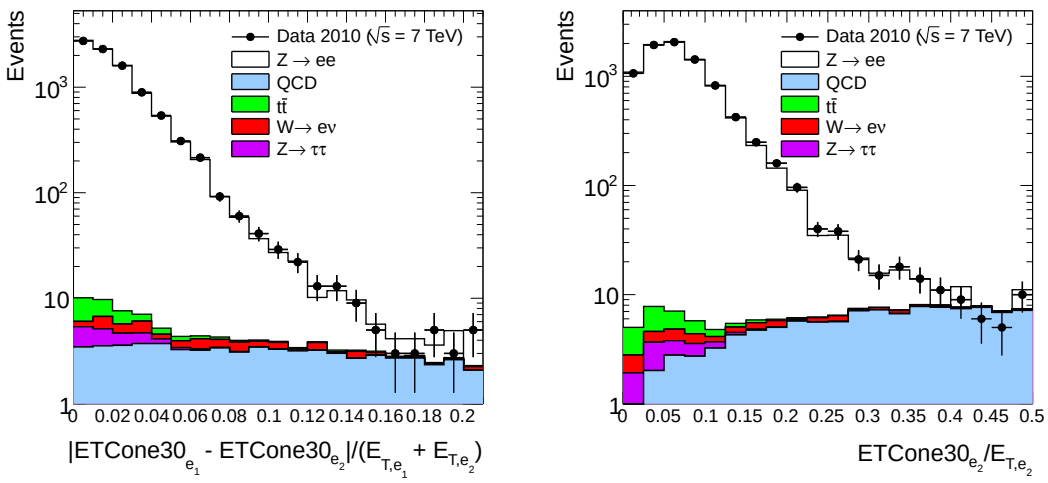

(a) (b)

Figure 6.4: (a) QCD background fit using the calorimeter based isolation variable of the sub-leading electron ETCone30/E_T (b) QCD background fit using $|\mathrm{ETCone30_{e_1}} - \mathrm{ETCone30_{e_2}}|/|E_{T,e_1} - E_{T,e_2}|$

6.3 The QCD Background Shape

The QCD background shapes for the p_T^{ee} distribution is also determined from medium-non-medium pairs where $Z \to ee$ processes are negligible.

A comparison of the shapes between same-sign and opposite-sign pairs is displayed in Figures 6.5. The difference between same-sign opposite-sign pairs is considered as a systematic uncertainty of the shape estimation.

6.4 Summary of Backgrounds

Combining the QCD normalization and shape, the final QCD background p_T^{ee} spectrum is shown in Figure 6.6 along with electroweak backgrounds estimated from MC samples. The background contributions summarized in Table 6.3 for 19 bins.

In the low p_T^{ee} (< 100 GeV) region, the dominant background is from QCD processes, while in the high p_T^{ee} (> 100 GeV) region, the dominant background is $t\bar{t}$.

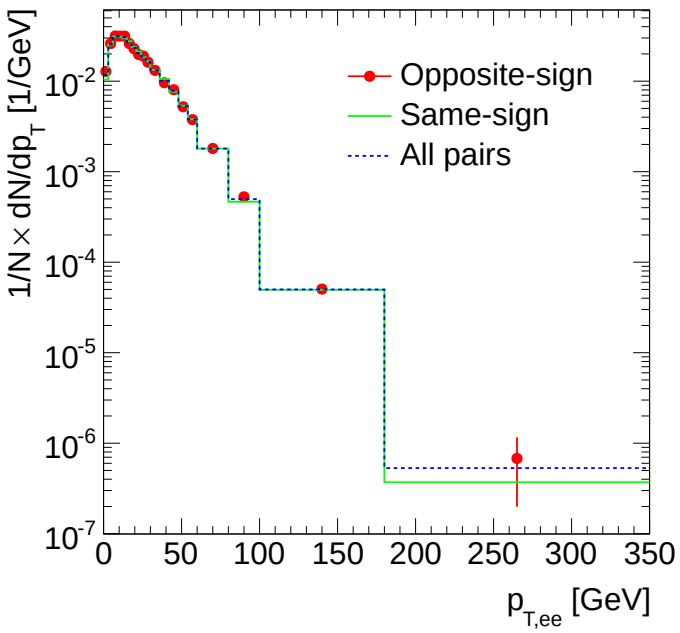

Figure 6.5: Normalized medium-non-medium pair spectrum in $p_{T.ee}$ Red marker: opposite-sign pairs, Green line: same-sign pairs, blue dashed-line: all pairs without the charge requirement.

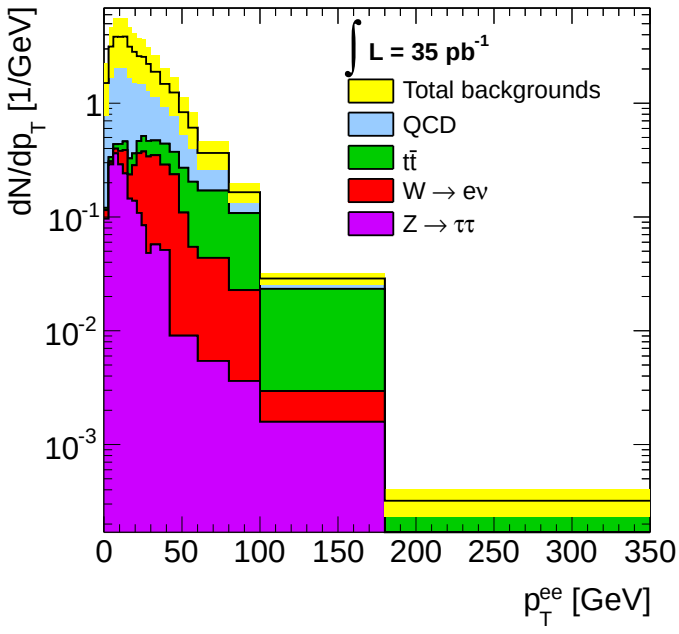

Figure 6.6: Summary of electroweak and QCD backgrounds.

p_T^{ee}	QCD	$t\bar{t}$	$W \to e\nu$	$Z \to \tau\tau$	Total Background
(GeV)			dN/dp_T^{ee} (1/GeV)		
0 − 3	1.3841 ± 0.7284	0.0056 ± 0.0028	0.0182 ± 0.0182	0.0965 ± 0.0246	1.5045 ± 0.7291
3 − 6	2.8098 ± 1.4787	0.0280 ± 0.0065	0.0182 ± 0.0182	0.2896 ± 0.0442	3.1456 ± 1.4795
6 − 9	3.4053 ± 1.7922	0.0378 ± 0.0076	0.0365 ± 0.0258	0.3620 ± 0.0501	3.8416 ± 1.7931
9 − 12	3.3929 ± 1.7856	0.0575 ± 0.0096	0.0911 ± 0.0409	0.2896 ± 0.0442	3.8311 ± 1.7867
12 − 15	3.3950 ± 1.7867	0.0743 ± 0.0111	0.1458 ± 0.0519	0.2413 ± 0.0400	3.8564 ± 1.7879
15 − 18	2.8119 ± 1.4798	0.0911 ± 0.0125	0.0911 ± 0.0409	0.1448 ± 0.0304	3.1389 ± 1.4808
18 − 21	2.4674 ± 1.2985	0.0771 ± 0.0113	0.1458 ± 0.0519	0.1388 ± 0.0298	2.8291 ± 1.3000
21 − 24	2.1270 ± 1.1194	0.1009 ± 0.0133	0.2552 ± 0.0690	0.1086 ± 0.0262	2.5918 ± 1.1219
24 − 27	2.0399 ± 1.0736	0.1388 ± 0.0161	0.2917 ± 0.0739	0.0845 ± 0.0230	2.5548 ± 1.0765
27 − 30	1.7494 ± 0.9207	0.1261 ± 0.0152	0.2917 ± 0.0739	0.0483 ± 0.0172	2.2154 ± 0.9239
30 − 36	1.4194 ± 0.7470	0.1212 ± 0.0116	0.2917 ± 0.0530	0.0573 ± 0.0135	1.8896 ± 0.7491
36 − 42	1.0376 ± 0.5461	0.1521 ± 0.0136	0.2370 ± 0.0475	0.0513 ± 0.0127	1.4779 ± 0.5484
42 − 48	0.8685 ± 0.4571	0.1367 ± 0.0126	0.2279 ± 0.0466	0.0090 ± 0.0052	1.2420 ± 0.4596
48 − 54	0.5634 ± 0.2965	0.1612 ± 0.0142	0.1003 ± 0.0305	0.0090 ± 0.0052	0.8339 ± 0.2985
54 − 60	0.4057 ± 0.2135	0.1493 ± 0.0134	0.0456 ± 0.0205	0.0090 ± 0.0052	0.6096 ± 0.2150
60 − 80	0.1949 ± 0.1026	0.1268 ± 0.0090	0.0383 ± 0.0104	0.0054 ± 0.0022	0.3653 ± 0.1035
80 −100	0.0570 ± 0.0300	0.0854 ± 0.0065	0.0191 ± 0.0073	0.0036 ± 0.0018	0.1651 ± 0.0316
100−180	0.0054 ± 0.0029	0.0204 ± 0.0016	0.0014 ± 0.0010	0.0016 ± 0.0006	0.0288 ± 0.0035
180−350	0.0001 ± 0.0000	0.0002 ± 0.0001	0.0000 ± 0.0000	0.0000 ± 0.0000	0.0003 ± 0.0001

Table 6.3: Summary of QCD, $W \to e\nu$, $t\bar{t}$ and $Z \to \tau\tau$ backgrounds for $Z \to ee$ process. The QCD background is estimated using data-driven method and the error includes both statistical and systematic errors. $W \to e\nu$, $t\bar{t}$ and $Z \to \tau\tau$ backgrounds are estimated from Monte Carlo simulation and the error reflects the limited Monte Carlo statistics.

CHAPTER VII

p_T^Z Extraction

After the background subtraction, p_T^Z is extracted from p_T^{ee} through "unfolding", which is a process converting observed measurements at the reconstruction level into the corresponding physics properties at the truth level. Section 7.1 introduces basic unfolding strategies. Section 7.2 and Section 7.3 present two unfolding methods: bin-by-bin unfolding and regularized matrix unfolding. To measure a binned distribution of a steeply falling spectrum, the bin center also requires corrections, which is studied in Section 7.4.

7.1 Unfolding Procedures

The transverse momentum of the Z boson is studied in two scenarios at the Born level before the final state radiation:

- p_T^Z in the fiducial (E_T, η) volume: p_T^Z with electron kinematic selections ($p_T^e > 20$ GeV and $|\eta^e| < 2.4$) and $66 < m_{ee} < 116$ GeV;
- p_T^Z in the full (E_T, η) phase-space: p_T^Z with $66 < m_{ee} < 116$ GeV.

To extract fiducial p_T^Z from p_T^{ee}, a bin-by-bin unfolding method is applied, which is cross-checked by the matrix unfolding. The corresponding correction is usually called "efficiency correction" (C), which accounts for the collision event selection, electron

identification, electron final state radiation, and detector resolution. The full phase-space p_T^Z is calculated by the bin-by-bin unfolding from the fiducial volume. The corresponding correction is usually called the "acceptance correction" (A), which is an extrapolation from a small (E_T^e, η^e) phase-space (fiducial volume) to the full (E_T^e, η^e) phase-space.

Since the binned p_T^Z or p_T^{ee} distribution is a vector with 19 elements, the general form of C or A should be an 19×19 matrix. For both bin-by-bin unfolding and regularized matrix unfolding, C and A are determined through $Z \to ee$ MC simulations.

One of the advantages of studying p_T^Z in the fiducial volume is that the acceptance factor A is same for both electron and muon decay channels. So one can combine electron and muon fiducial p_T^Z using the same A to get the differential cross-section of $Z \to \ell\ell$ $(\ell = e, \mu)$.

This thesis will focus on the extraction of the fiducial cross-section.

7.2 The Bin-by-bin Unfolding

The bin-by-bin unfolding method ignores the correlations between bins. Only diagonal elements of C and A matrices are non-zero. Therefore, C and A are reduced to vectors with 19 elements. The observed number of events N, the cross-section σ, efficiency correction ϵ and luminosity L satisfy $N = \sigma\epsilon L$. Thus, the differential $Z \to ee$ cross-section can be expressed as

$$\frac{\Delta\sigma_Z^i}{\Delta p_T^{Z,i}} = \frac{1}{\Delta p_T^{Z,i}} \cdot \frac{N_{\text{data}}^i - N_{\text{bkg}}^i}{A^i \cdot C^i \cdot L} \tag{7.1}$$

where

- $\Delta\sigma_Z^i$ is the integrated cross-section of Z boson times the branching ratio for decays into electrons in the i-th bin;

- $\Delta p_{\mathrm{T}}^{i}$ is the width of the corresponding bin;
- N_{data}^{i} is the number of $Z \to ee$ candidates in each bin from data;
- N_{bkg}^{i} is the estimated total background event number in each bin;
- $A^{i} = \frac{N_{\mathrm{geo}}^{i}}{N_{\mathrm{gen}}^{i}}$ is the acceptance correction factor determined from Monte Carlo simulation, defined as the fraction of generated events (N_{gen}) satisfying the geometrical constrains (N_{geo}) at the generator level;
- $C^{i} = \frac{N_{\mathrm{reco}}^{i}}{N_{\mathrm{geo}}^{i}}$ is the efficiency correction factor, defined as the ratio between number of signal events which pass the final selection (N_{reco}) and total number of generated events within the detector geometrical acceptance (N_{geo});
- L the integrated data luminosity.

In the fiducial volume, the cross-section is

$$\frac{\Delta\sigma_{\mathrm{bare}}^{i}}{\Delta p_{T}^{Z,i}} = \frac{1}{\Delta p_{T}^{Z,i}} \cdot \frac{N_{\mathrm{data}}^{i} - N_{\mathrm{bkg}}^{i}}{C^{i} \cdot L}. \tag{7.2}$$

7.2.1 The Efficiency Correction Factor C

C^{i} is determined from C_{MC}^{i} from the $Z \to ee$ MC and requires additional corrections to account for discrepancies of electron trigger and identification efficiencies between data and the MC, which lead to the following form:

$$C^{i} = C_{\mathrm{MC}}^{i} \cdot \frac{\varepsilon_{\mathrm{data}}^{\mathrm{ID},i}}{\varepsilon_{\mathrm{MC}}^{\mathrm{ID},i}} \cdot \frac{\varepsilon_{\mathrm{data}}^{\mathrm{trig},i}}{\varepsilon_{\mathrm{MC}}^{\mathrm{trig},i}}, \tag{7.3}$$

$$\varepsilon^{\mathrm{ID},i} = \frac{1}{N} \sum_{n=1}^{N} \varepsilon_{e_1}^{\mathrm{ID}}(E_T \text{ or } p_{\mathrm{T}}, \eta) \cdot \varepsilon_{e_2}^{\mathrm{ID}}(E_T \text{ or } p_{\mathrm{T}}, \eta) \cdot \Delta_{n}^{i}, \tag{7.4}$$

$$\varepsilon^{\mathrm{trig},i} = \frac{1}{N}\sum_{n=1}^{N}(1-(1-\varepsilon_{e_1}^{\mathrm{trig}}(E_T \text{ or } p_{\mathrm{T}},\eta))\cdot(1-\varepsilon_{e_2}^{\mathrm{trig}}(E_T \text{ or } p_{\mathrm{T}},\eta)))\cdot\Delta_n^i \qquad (7.5)$$

where

- $\varepsilon^{\mathrm{ID},i}$: electron identification efficiency determined from data or the $Z \to ee$ MC; by summing over all the candidates. $\Delta_n^i = 1(\Delta_n^i = 0)$ if the nth event falls inside(outside) bin i;
- $\varepsilon^{\mathrm{trig},i}$: trigger efficiency determined by data or the $Z \to ee$ MC.

As presented Section 4.2, trigger efficiencies of data and the $Z \to ee$ MC are close, $\frac{\varepsilon_{\mathrm{data}}^{\mathrm{trig},i}}{\varepsilon_{\mathrm{MC}}^{\mathrm{trig},i}} \approx 1$. So only the medium electron identification scale factor is needed to correct C_{MC}. Re-writing Equation 7.3 with the medium electron scale factor (SF) summarized in Table 4.1

$$C^i = C_{\mathrm{MC}}^i \cdot \prod_{n=1}^{N} SF_n^{e_1} SF_n^{e_2} \Delta_n^i. \qquad (7.6)$$

The C_{MC} and SF from the default PYTHIA sample are shown in Figure 7.1 and 7.2.

7.2.2 The Acceptance Correction Factor A

The acceptance factor only depends on truth level information so that it can be studied easily without full simulation chains. The nominal A from the default PYTHIA sample is shown in Figure 7.3.

7.2.3 The FSR Correction Factor C_{bare}^i

Before electrons reach the detector, they might radiate photons. Therefore, it is also important to extract the cross-section σ_{bare}^i corresponding to Z bosons constructed by two "bare" electrons. The bare electrons are Born level electrons after

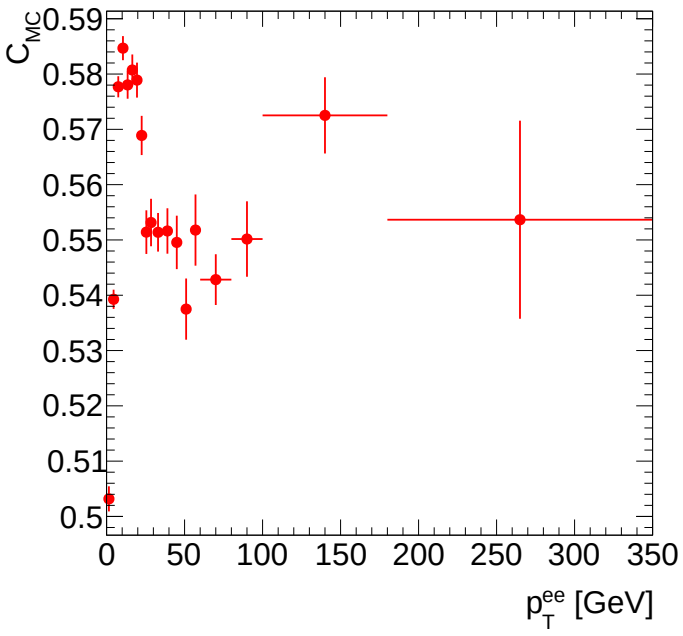

Figure 7.1: Nominal C_{MC} from the PYTHIA sample.

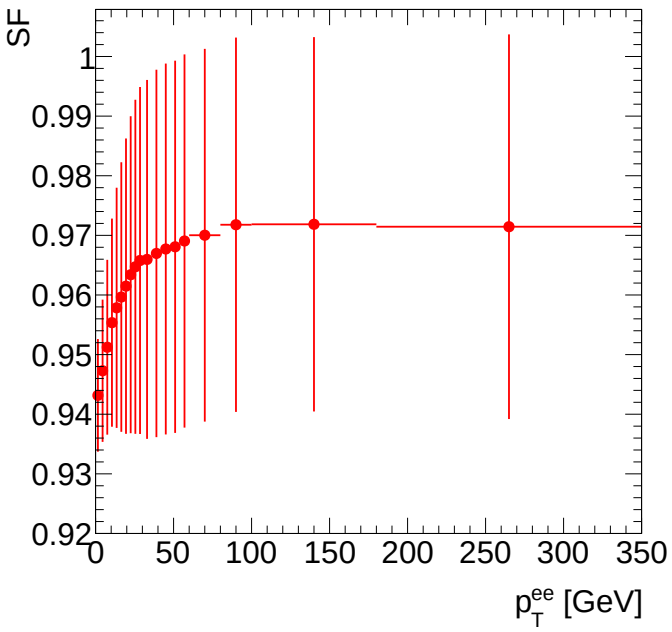

Figure 7.2: Nominal SF from the PYTHIA sample.

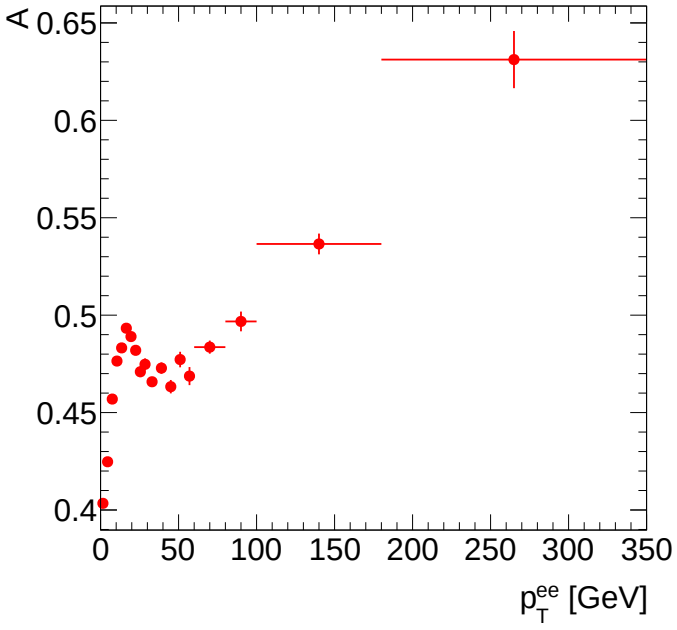

Figure 7.3: Nominal A from the PYTHIA sample.

corrections of QED final state radiation. An additional efficiency correction factor is needed to calculate the bare cross-section from the Born cross-section

$$\sigma^i_{\text{bare}} = \sigma^i_Z \cdot C^i_{\text{bare}} = \frac{N^i_{\text{data}} - N^i_{\text{bkg}}}{A^i \cdot L} \frac{C^i_{\text{bare}}}{C^i}. \tag{7.7}$$

The nominal C_{bare} from the default PYTHIA sample is shown in Figure 7.4.

7.2.4 Unfolding Results

The final normalized differential cross-section is calculated as

$$\frac{1}{\sigma}\left(\frac{d\sigma}{dp_T^Z}\right)^i = \frac{1}{\sum_{i=1}^n \sigma^i} \frac{\sigma^i}{\Delta p_T^{Z,i}} \tag{7.8}$$

where σ^i is the Born cross-section σ^i_Z, bare cross-section σ^i_{bare} or fiducial cross-section σ^i_{fid}. The normalized fiducial $\frac{1}{\sigma}\frac{\mathrm{d}\sigma}{\mathrm{d}p_T^Z}$ from bin-by-bin method are summarized in Table 7.1.

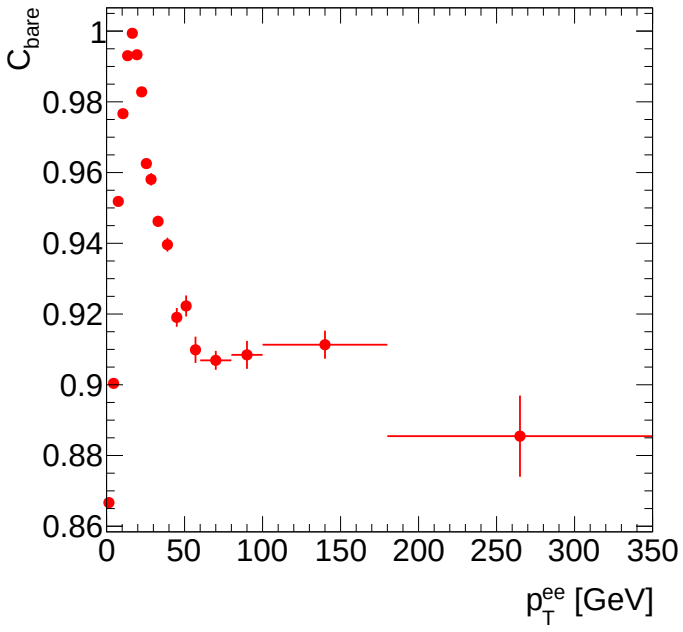

Figure 7.4: Nominal C_{bare} from the PYTHIA sample.

p_T^{ee} (GeV)	$\frac{1}{\sigma}\frac{d\sigma}{dp_T^Z}$ (1/GeV)	stat. (1/GeV)	$\frac{\text{stat.}}{\text{mean}}$ (%)
0 – 3	0.0348	0.0012	3.4
3 – 6	0.0585	0.0015	2.6
6 – 9	0.0461	0.0013	2.8
9 – 12	0.0343	0.0011	3.2
12 – 15	0.0293	0.0010	3.5
15 – 18	0.0204	0.0008	4.1
18 – 21	0.0164	0.0008	4.6
21 – 24	0.0132	0.0007	5.2
24 – 27	0.0108	0.0006	5.8
27 – 30	0.0102	0.0006	5.9
30 – 36	0.0072	0.0004	5.0
36 – 42	0.0049	0.0003	6.0
42 – 48	0.0037	0.0003	7.0
48 – 54	0.0033	0.0002	7.5
54 – 60	0.0021	0.0002	9.1
60 – 80	$1.2{\cdot}10^{-3}$	$8.1{\cdot}10^{-5}$	6.7
80 –100	$5.7{\cdot}10^{-4}$	$5.5{\cdot}10^{-5}$	9.7
100–180	$1.7{\cdot}10^{-4}$	$1.5{\cdot}10^{-5}$	8.7
180–350	$7.8{\cdot}10^{-6}$	$2.2{\cdot}10^{-6}$	28.7

Table 7.1: Summary of the fiducial $\frac{1}{\sigma}\frac{d\sigma}{dp_T^Z}$ from the bin-by-bin unfolding. The statistical uncertainty is calculated by propagating binomial errors from observed data.

7.3 The Regularized Matrix Unfolding

Regularized matrix unfolding takes into account the correlation between bins. So C is an 19×19 matrix with generally non-zero off-diagonal elements. The matrix which transforms a distribution at the truth level to the reconstruction level is usually called the Response Matrix and denoted as R. Suppose $\vec{x}$ and $\vec{y}$ are vectors of the fiducial and observed (after the background subtraction) differential cross-sections, so the transformation from the truth to reconstruction level can be expressed as

$$R\vec{x} = \vec{y}. \tag{7.9}$$

7.3.1 The Inverse of R

To calculate $\vec{x}$ from $\vec{y}$, the response matrix R has to be inverted. Since the response matrix is not always reversible, a regularized least square method [36] is employed to calculate regularized inverse $R^{\#}$.

The "least square" means instead of inverting a matrix, a $R^{\#}$ is calculated from the minimization

$$\chi^2(\vec{x}) = ||R\vec{x} - \vec{y}|| = \text{minimum} \tag{7.10}$$

where $\chi^2(\vec{x})$ is also called the residual of the least square minimization.

The "regularized" means a conditional term is added in the minimization process, which will smooth the unfolded distribution

$$\chi^2_\tau(\vec{x}) = ||R\vec{x} - \vec{y}|| + \tau||L\vec{x}|| = \text{minimum} \tag{7.11}$$

where τ is the regularization parameter and L is the conditional matrix. In this analysis, the continuity condition at the second derivative is required

$$x_i'' \propto x_{i-1} - 2x_i + x_{i+1} \Rightarrow L = \begin{pmatrix} 1 & -2 & 1 & 0 & ... & 0 & 0 & 0 \\ 0 & 1 & -2 & 1 & ... & 0 & 0 & 0 \\ \vdots & \vdots & \vdots & \vdots & \ddots & \vdots & \vdots & \vdots \\ 0 & 0 & 0 & 0 & ... & 1 & -2 & 1 \end{pmatrix}. \tag{7.12}$$

In the minimization process, the matrix H, error matrix P (the error for each bin is $\sqrt{P_{ii}}$) and correlation matrix ρ are calculated as

$$H_{ij} = \frac{\partial \chi^2_\tau(\vec{x})}{\partial x_i \partial x_j}, \tag{7.13}$$

$$P = (\frac{1}{2}H)^{-1}, \tag{7.14}$$

$$\rho_{ij} = \frac{P_{ij}}{\sqrt{P_{ii}P_{jj}}}. \tag{7.15}$$

A reliable $R^{\#}$ requires minimum $\chi^2_\tau(\vec{x})$ and τ [37]. The spline of $(\chi^2_\tau(\vec{x}), ||L\vec{x}||)$ is a "L-curve", where the best τ is at the turning point. The `TUnfold` program [38] is used to calculate $R^{\#}$ with the optimized τ. Once $R^{\#}$ is determined, the fiducial cross-section can be expressed as

$$\sigma^i_{\text{fid}} = \sum_{j=1}^{m} (R^{\#})^{ij} \frac{N^j_{\text{data}} - N^j_{\text{bkg}}}{L} \tag{7.16}$$

where

- $i = 1, 2, ..., n$ is the bin index of the generated distribution;
- $j = 1, 2, ..., m$ is the bin index of the measured distribution.

In the regularized unfolding method, the number of bins at the truth level must be greater than that at the reconstruction level $n > m$. This is because the degree of freedom of regularization is equal to $(m - n)$ [38]. In this thesis, the bin size at

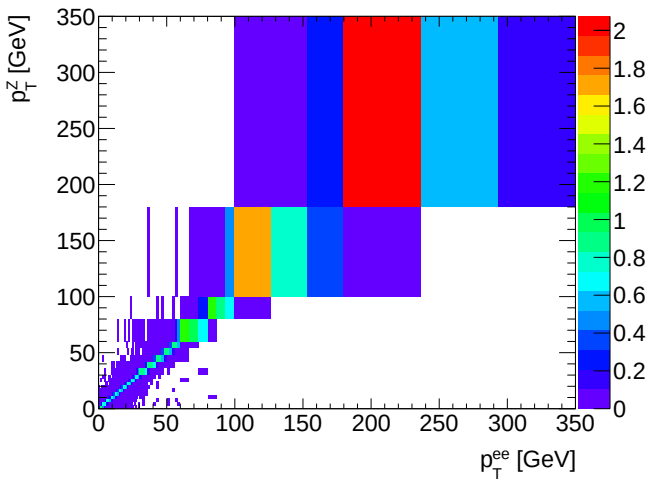

Figure 7.5: Response matrix (38×19) of the PYTHIA $Z \to ee$ MC. The x axis corresponds to the reconstruction level with 38 bins, while y axis corresponds to the truth level with 19 bins.

the truth level is one half of the bin size at the reconstruction level. So $m = 19$ and $n = 38$. Figure 7.5 shows the response matrix in the binning set of 38×19, which is calculated from the PYTHIA $Z \to ee$ sample with full statistics.

7.3.2 Closure Tests

A closure test is made using a pseudo-data from a sub-set of the PYTHIA $Z \to ee$ MC. The statistics of the pseudo-data are equal to 35 pb^{-1}. The L-curve of the closure test is shown in Figure 7.6.

The unfolding result is compared to the true p_T^Z of the pseudo-data and the MC with full statistics as shown in Figure 7.7(a) and 7.7(b).

Another test with pseudo-data is that folding p_T^Z back to the reconstruction level

$$R(R^{\#}\vec{x}) \approx \vec{y}. \tag{7.17}$$

The folding-back results are shown in Figure 7.8(a) and 7.8(b).

Both closure tests show that the matrix unfolding results have a good agreement with the predictions.

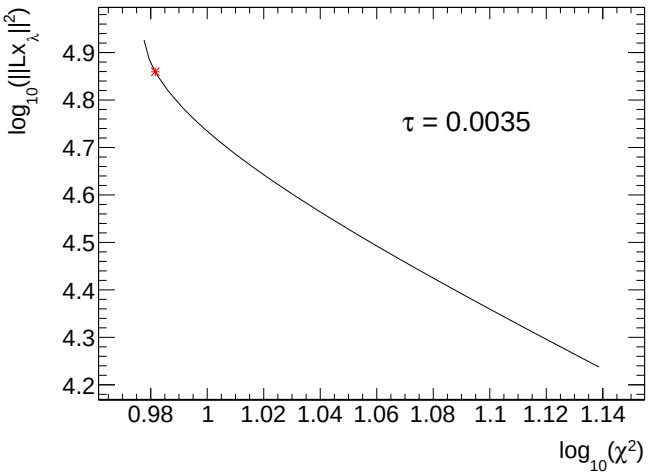

Figure 7.6: L-curve of the PYTHIA $Z \to ee$ MC.

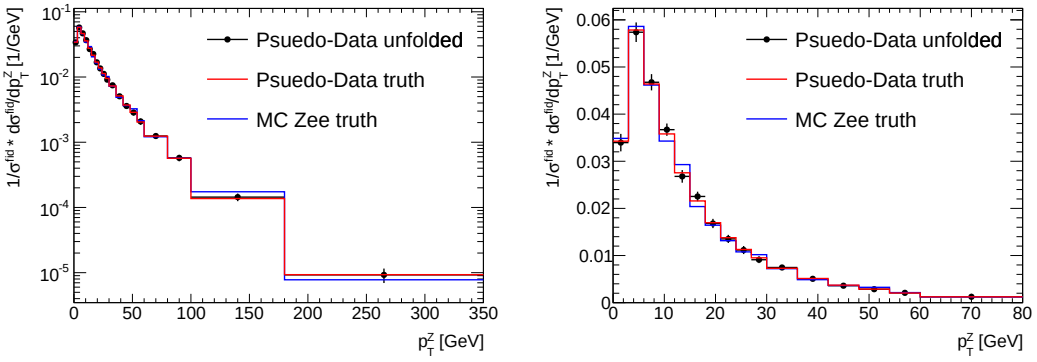

(a) (b)

Figure 7.7: MC closure test of the regularized matrix unfolding. The cross-section is unfolded in the fiducial volume.

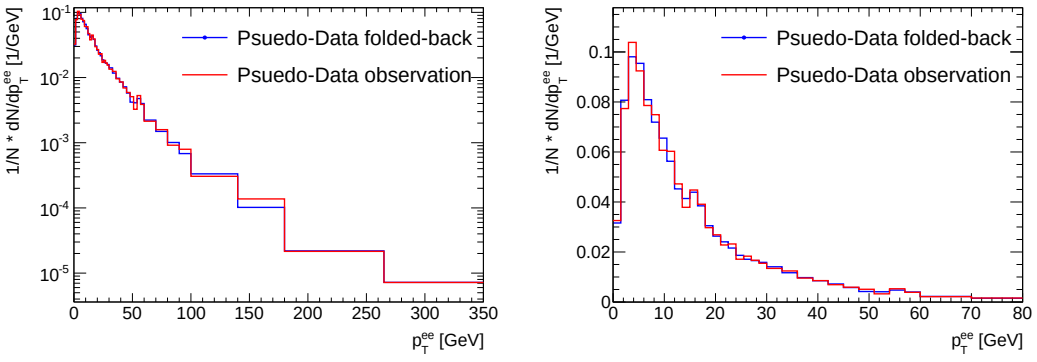

(a) (b)

Figure 7.8: MC closure test of the folding-back p_T^Z to the reconstruction level with 38 bins.

p_T^{ee} (GeV)	$\frac{1}{\sigma}\frac{d\sigma}{dp_T^Z}$ (1/GeV)	stat. (1/GeV)	$\frac{\text{stat.}}{\text{mean}}$ (%)
0 − 3	0.0347	0.0017	4.9
3 − 6	0.0597	0.0025	4.1
6 − 9	0.0463	0.0023	4.9
9 − 12	0.0330	0.0020	6.0
12 − 15	0.0317	0.0018	5.7
15 − 18	0.0196	0.0016	7.9
18 − 21	0.0172	0.0014	8.1
21 − 24	0.0119	0.0012	10.3
24 − 27	0.0110	0.0011	10.3
27 − 30	0.0102	0.0010	10.1
30 − 36	0.0070	0.0005	7.1
36 − 42	0.0049	0.0004	8.3
42 − 48	0.0036	0.0004	9.8
48 − 54	0.0032	0.0003	10.0
54 − 60	0.0021	0.0003	12.7
60 − 80	$1.1 \cdot 10^{-3}$	$9.0 \cdot 10^{-5}$	7.9
80 −100	$5.8 \cdot 10^{-4}$	$6.4 \cdot 10^{-5}$	11.1
100−180	$1.8 \cdot 10^{-4}$	$1.6 \cdot 10^{-5}$	9.3
180−350	$9.8 \cdot 10^{-6}$	$2.9 \cdot 10^{-6}$	29.7

Table 7.2: Summary of regularized matrix unfolding fiducial $\frac{1}{\sigma}\frac{d\sigma}{dp_T^Z}$. The statistical error is from five sources: correlated data, uncorrelated data, correlated matrix elements, uncorrelated matrix elements.

7.3.3 Unfolding Results

Regularized matrix unfolding results for 2010 data are summarized in Table 7.2. Four different statistical uncertainties are computed:

- Uncorrelated statistical uncertainty of data, which is the dominant uncertainty
- Uncorrelated statistical uncertainty of the response matrix R;
- Correlated statistical uncertainty of data;
- Correlated statistical uncertainty of the response matrix R.

p_T^{ee} (GeV)	Bin center (GeV)	$\bar{p}_T^Z$ (GeV)	Difference (%)
0 − 3	1.5	1.3	-10.3
3 − 6	4.5	4.8	6.0
6 − 9	7.5	7.5	-0.5
9 − 12	10.5	10.4	-0.6
12 − 15	13.5	13.5	-0.3
15 − 18	16.5	16.5	-0.1
18 − 21	19.5	19.5	-0.2
21 − 24	22.5	22.5	-0.1
24 − 27	25.5	25.5	-0.1
27 − 30	28.5	28.4	-0.2
30 − 36	33.0	32.9	-0.4
36 − 42	39.0	39.0	-0.1
42 − 48	45.0	44.9	-0.1
48 − 54	51.0	50.8	-0.3
54 − 60	57.0	56.9	-0.1
60 − 80	70.0	69.4	-0.9
80 −100	90.0	89.4	-0.7
100−180	140.0	132.3	-5.5
180−350	265.0	245.4	-7.4

Table 7.3: Corrected bin centers using the RESBOS MC.

7.4 The Bin Center Correction

The ith bin center $\bar{p}_T^{Z,i}$ is corrected according to the p_T^Z shape in each bin, so that the overall p_T^Z line-shape after the unfolding is consistent with the true distribution. The correction formula is

$$\bar{p}_T^{Z,i} = \arg\left\{ \frac{d\sigma(\bar{p}_T^{Z,i})}{dp_T^Z} = \frac{1}{\Delta p_T^{Z,i}} \cdot \int_{p_T^{Z,i,\mathrm{low}}}^{p_T^{Z,i,\mathrm{high}}} \frac{d\sigma(p_T^Z)}{dp_T^Z} dp_T^Z \right\}. \tag{7.18}$$

To extract the p_T^Z shape, each bin is divided into 10 sub-bins. Equation 7.18 is solved numerically for each bin as shown in Figure 7.9 and 7.10. The corrected bin centers are summarized in Table 7.3.

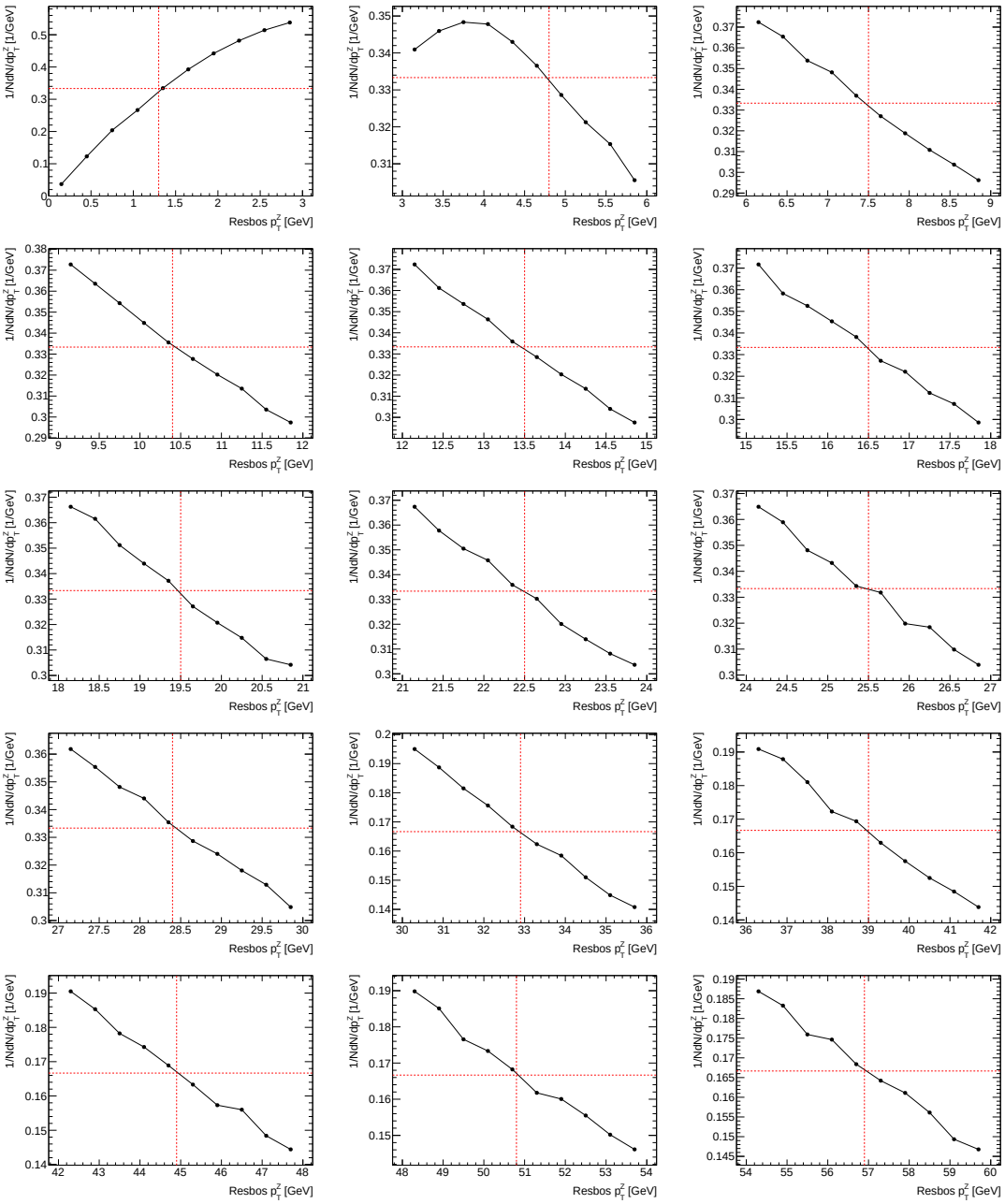

Figure 7.9: The numerical method to calculate the bin center with 10 sub-bins for bin 1 to 15.

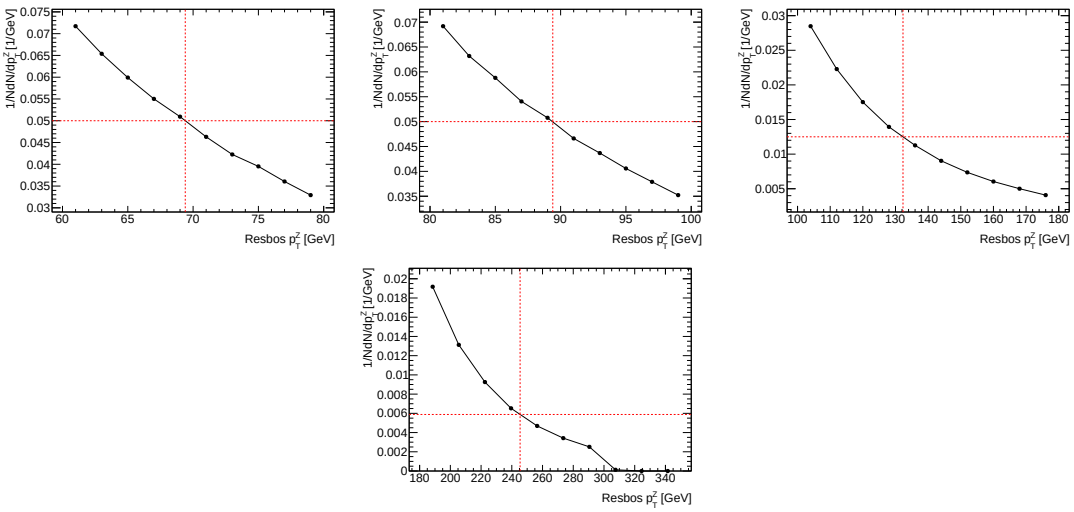

Figure 7.10: The numerical method to calculate the bin center with 10 sub-bins for bin 16 to 19.

CHAPTER VIII

Uncertainties

Uncertainties of $\frac{1}{\sigma}\frac{\mathrm{d}\sigma}{\mathrm{d}p_T^Z}$ measurements are studied in this chapter. Section 8.1 presents statistical uncertainties. Section 8.2 presents experimental systematic uncertainties. Section 8.3 presents theoretical systematic uncertainties. Section 8.4 summarizes all uncertainties from both bin-by-bin unfolding and regularized matrix unfolding.

8.1 Statistical Uncertainties

Statistical uncertainties of $\frac{1}{\sigma}\frac{\mathrm{d}\sigma}{\mathrm{d}p_T^Z}$ are caused by a limited number of events in both data and $Z \to ee$ MC samples. The total integrated luminosity of data is 35 pb^{-1}, while the corresponding luminosity of the $Z \to ee$ MC is about 1 fb^{-1}. Therefore, data statistical uncertainty dominates. Since there are strong correlations between bins after the normalization, propagating uncertainties of of N_{data} and C to $\frac{1}{\sigma}\frac{\mathrm{d}\sigma}{\mathrm{d}p_T^Z}$ through analytical formulas is often impractical. Therefore, ensemble MC test and bootstrap resampling are used to estimate statistical uncertainties caused by N_{data} and C, respectively.

8.1.1 The Data Statistical Uncertainty

500 ensemble MC tests to study the data statistical uncertainty and their results are shown in Figure 8.1 and 8.2. Ensemble tests procedures are

1. Randomly choose events from the PYTHIA $Z \to ee$ sample as pseudo-data until integrated luminosity reaches 35 pb^{-1};
2. Unfold the pseudo-data with the nominal C with using bin-by-bin method;
3. Repeat step (1) and (2) by 500 times and calculate statistical uncertainties.

The statistical uncertainties from three approaches are compared

- Root mean square (RMS) of the unfolding result of 500 ensemble tests;
- Standard deviation of the Gaussian fit to the unfolding result of 500 ensemble tests;
- Simple error propagation by ignoring correlations.

Data statistical uncertainties from three approaches are in good agreements as shown in Figure 8.3. Baseline results are calculated by the RMS approach due to its robustness.

8.1.2 The Monte Carlo Statistical Uncertainty

The statistical uncertainties of C can not be estimated by ensemble tests since the calculation of C uses full statistics of the $Z \to ee$ sample. Therefore, a bootstrap method [39], which is based on multiple resampling of $Z \to ee$ MC events, is used to evaluate statistical uncertainties of C. The bootstrap method constructs a number of resamples of the pseudo MC dataset each of which is obtained by random sampling with replacement from the original dataset.

Bootstrap resampling is implemented in the analysis as follows:

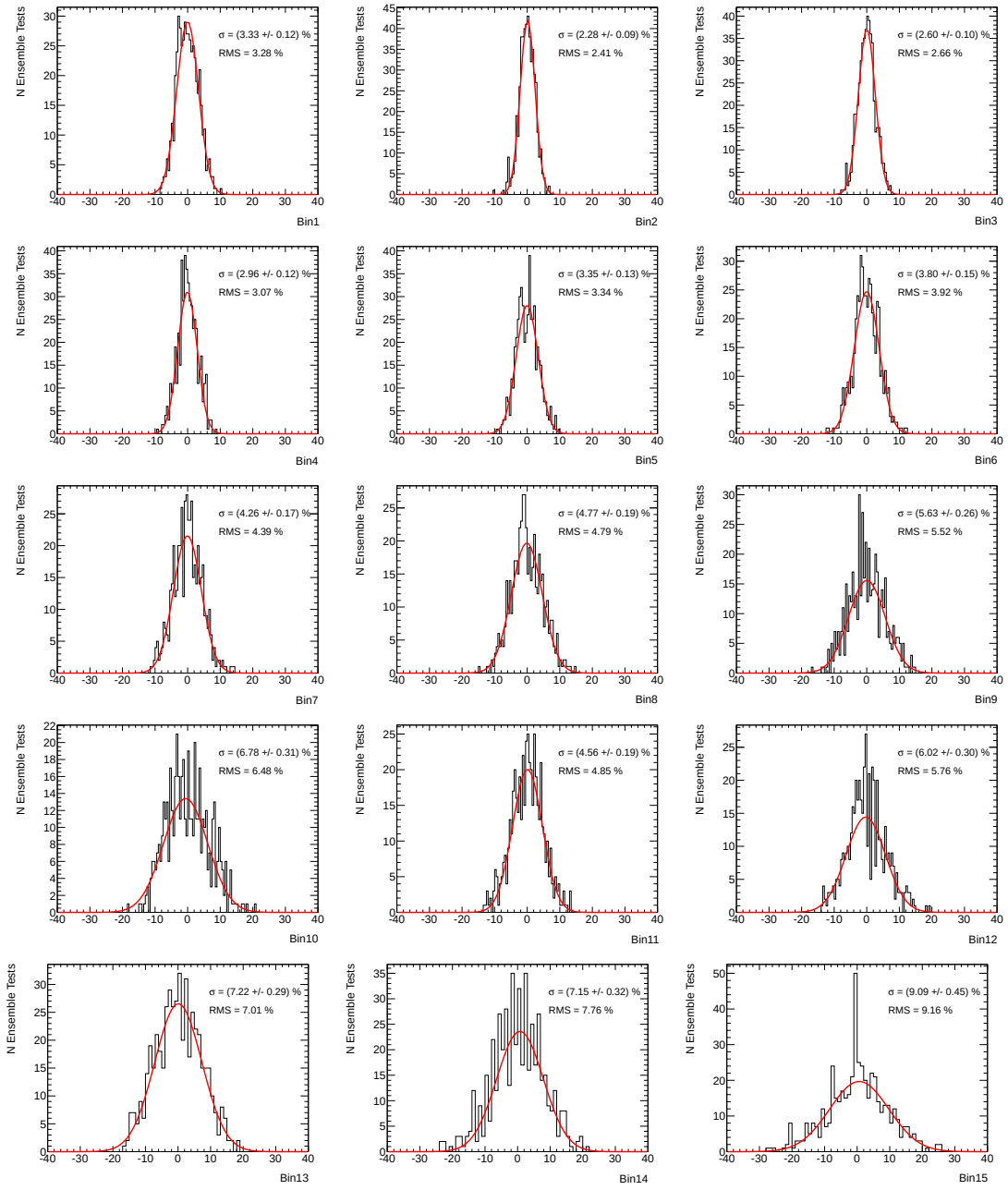

Figure 8.1: 500 ensemble tests to estimate data statistical uncertainty of the fiducial p_T^Z measurement for bin 1 to 15.

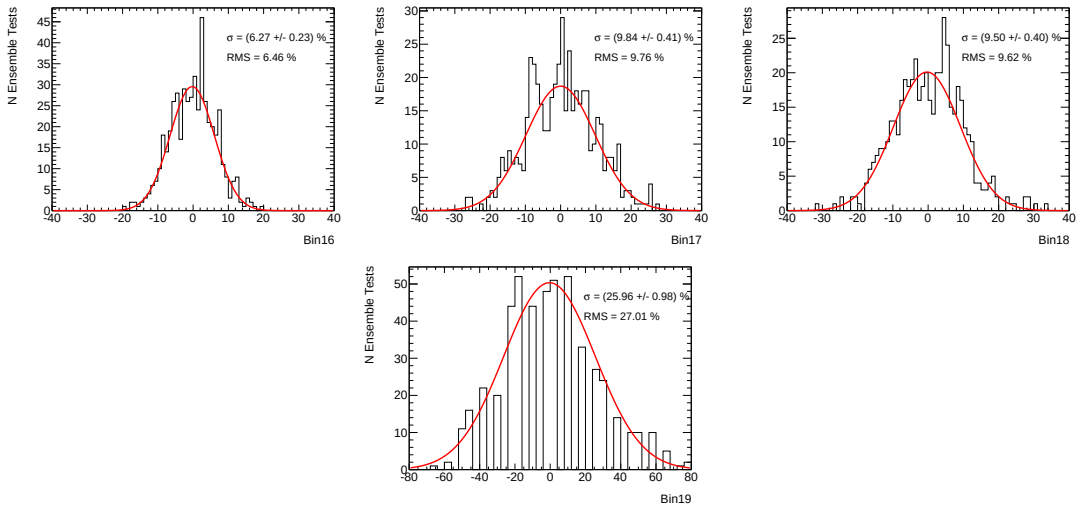

Figure 8.2: 500 ensemble tests to estimate data statistical uncertainty of the fiducial p_T^Z measurement for bin 16 to 19.

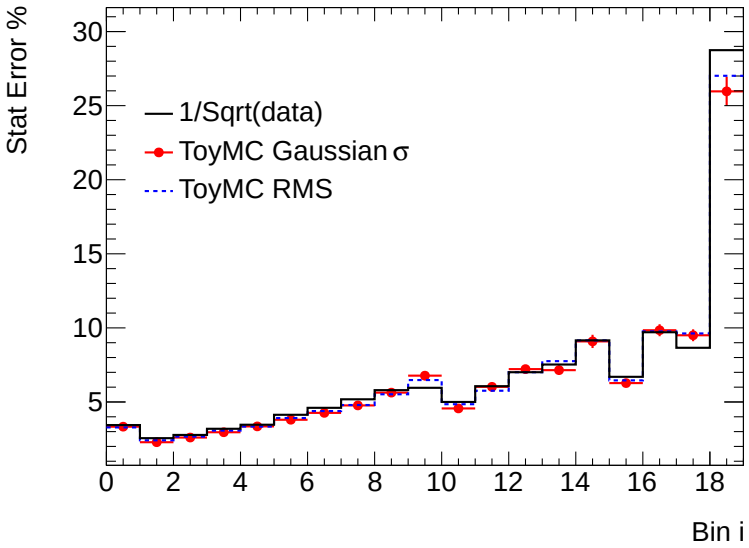

Figure 8.3: Comparisons of statistical uncertainties from three approaches: (1) Propagating Poisson uncertainties of observed data (black) (3) Standard deviation of the Gaussian fit (red) (3) Ensemble test RMS (blue).

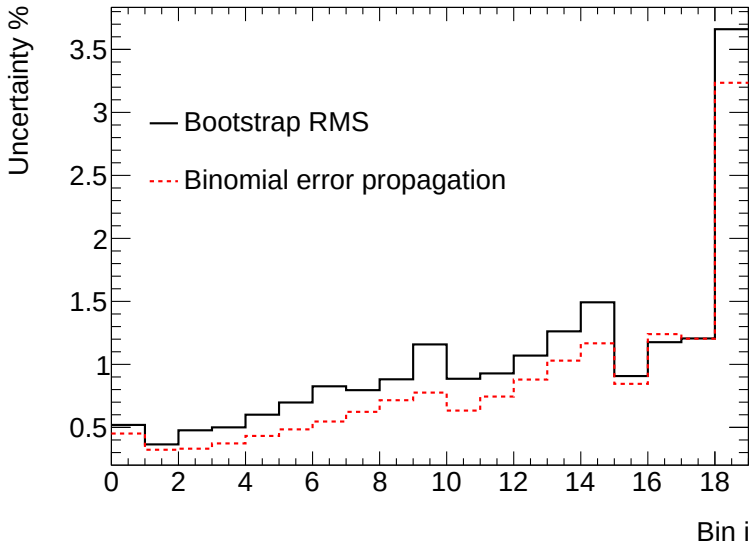

Figure 8.4: Bootstraping method to estimate statistical uncertainties of C. It is compared with results from propagating binomial uncertainties.

1. Assign a random weight `Poisson(1)` for each event;

2. Construct the new efficiency factor C and calculate the fiducial $\frac{1}{\sigma}\frac{\mathrm{d}\sigma}{\mathrm{d}p_T^Z}$;

3. Repeat step (1) and (2) 500 times and calculate the RMS of $\frac{1}{\sigma}\frac{\mathrm{d}\sigma}{\mathrm{d}p_T^Z}$ for each bin.

The default $Z \to ee$ sample has 10^6 events, so statistics of each resample will be approximately:

$$\sum_{i=0}^{i=10^6} \texttt{Poisson(1)} \approx 10^6. \tag{8.1}$$

Statistical uncertainties from the bootstrap method and simple binomial error propagation are compared in Figure 8.4. Since the simple error propagation ignores correlations between bins, its statistical uncertainties are underestimated.

8.2 Experimental Systematics

Experimental systematic uncertainties of $\frac{1}{\sigma}\frac{\mathrm{d}\sigma}{\mathrm{d}p_T^Z}$ arise from inefficiencies of dead OTX regions, misdealing of pileup, electron energy resolution and scale, the electron

identification efficiency and the background estimation.

To evaluate these systematic uncertainties, the correction C is determined either from a corrected or a particular MC sample, and are used to unfold the data. The deviation of $\frac{1}{\sigma}\frac{\mathrm{d}\sigma}{\mathrm{d}p_T^Z}$ from the central value is considered as the systematic uncertainty. To reduce the bias from statistical fluctuations, systematic uncertainties are determined from 100 bootstrap resamples.

For each resample n, the measured spectrum is unfolded and the relative deviation $\Delta(\frac{1}{\sigma}\frac{\mathrm{d}\sigma}{\mathrm{d}p_T^Z})$ of bin i is calculated

$$\Delta^i_{n,\mathrm{rel}}\left(\frac{1}{\sigma}\frac{\mathrm{d}\sigma}{\mathrm{d}p_T^Z}\right) = \frac{\left(\frac{1}{\sigma}\frac{\mathrm{d}\sigma}{\mathrm{d}p_T^Z}\right)^i_n - \left(\frac{1}{\sigma}\frac{\mathrm{d}\sigma}{\mathrm{d}p_T^Z}\right)^i_{\mathrm{nominal}}}{\left(\frac{1}{\sigma}\frac{\mathrm{d}\sigma}{\mathrm{d}p_T^Z}\right)^i_{\mathrm{nominal}}}. \tag{8.2}$$

Then, a Gaussian fit is applied on the distribution of $\Delta^i_{\mathrm{rel}}(\frac{1}{\sigma}\frac{\mathrm{d}\sigma}{\mathrm{d}p_T^Z})$ to extract the mean of relative deviations, $\bar{\Delta}^i_{\mathrm{rel}}(\frac{1}{\sigma}\frac{\mathrm{d}\sigma}{\mathrm{d}p_T^Z})$, which is quoted as the systematic uncertainty of bin i.

8.2.1 Modeling of Pileup

The uncertainty due to the modeling of pileup is estimated using the reference signal MC with and without applying the reweighting coefficients from Table 5.5 which correct the distribution of the number of primary vertices in MC to match that in the data. An uncertainty of $\approx 0.3\%$ is assigned due to pileup modeling as shown in Figure 8.5.

8.2.2 Dead OTX Regions

Multiple OTX maps are used during the 2010 data-taking periods. An average OTX map is made by weighting each OTX map to its integrated luminosity. Table 8.1 summarizes of the average efficiency correction factor C of these OTX maps. Based

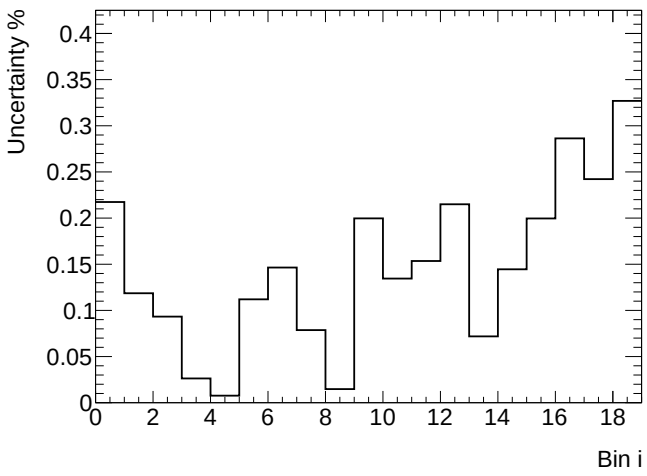

Figure 8.5: Systematic uncertainty due to the pileup-up.

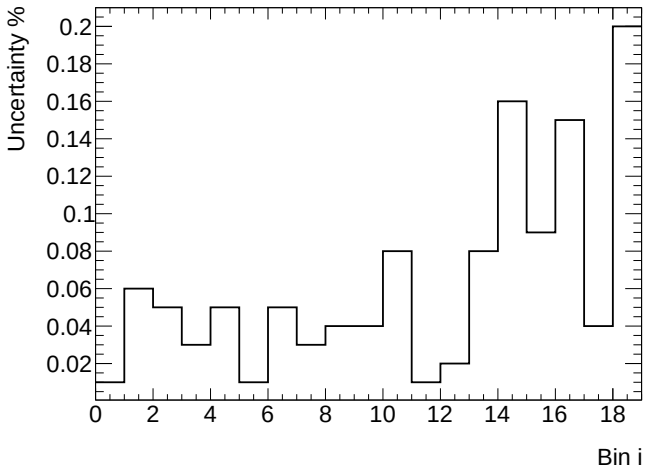

Figure 8.6: Systematic uncertainty due to the dead OTX regions

on the average OTX map, another ideal OTX map can be made by replicating the selected zone without holes in the detector [11]. The systematic uncertainty of the dead OTX is assumed to be the difference of unfolded results from ideal and real maps. This yields an uncertainty of less then 0.1% as shown in Figure 8.6.

8.2.3 The Electron Energy Scale and Resolution

The electron energy scale uncertainty is estimated by applying the correction plus or minus the error to data and comparing the unfolded results. The energy scale

Map Number	C	ΔC	Luminosity nb^{-1}
152166	0.6241	0.0346	9
155228	0.6251	0.0356	7
155760	0.6197	0.0302	2
158115	0.6151	0.0256	66
158707	0.6058	0.0163	28
159040	0.5993	0.0098	1088
161730	0.5962	0.0067	1836
165589	0.5962	0.0067	3537
166142	0.5949	0.0054	4416
166497	0.5892	-0.0003	3927
166658	0.5867	-0.0028	1883
167521	0.5859	-0.0036	18463
Average	0.5895	0.0000	35262

Table 8.1: The efficiency correction C_Z for 12 dead FEB maps in 2010. The map number is the first run number, since which the corresponding dead FEB map is applied. The average OTX maps is calculated based on luminosity weights and used in the unfolding.

variation leads to a shift in the p_{T} distribution. When enlarging the scale, a positive shift is seen in the first bins which then slowly decreases and turns negative. In total this yields an uncertainty between 2% to 4%. For the electron energy resolution uncertainty, the additional smearing which is applied to the MC sample to correct the energy resolution is varied by plus and minus the error. This results in a systematic uncertainty of less than 0.5%. The systematic uncertainties due to the electron energy scale and resolution are shown in Figure 8.7(a) and 8.7(b), respectively.

8.2.4 The Electron Identification Efficiency

To test the influence on the modeling of the electron identification efficiency, first the single electron scale factor, which is determined in few η bins, is varied within errors. The correction leads mostly to a global change of the number of selected events with a small deviation ($\approx 0.5\%$) after normalization. Since the correction factors are determined as a function of p_T^{ee}, it is also important to show that the data and MC

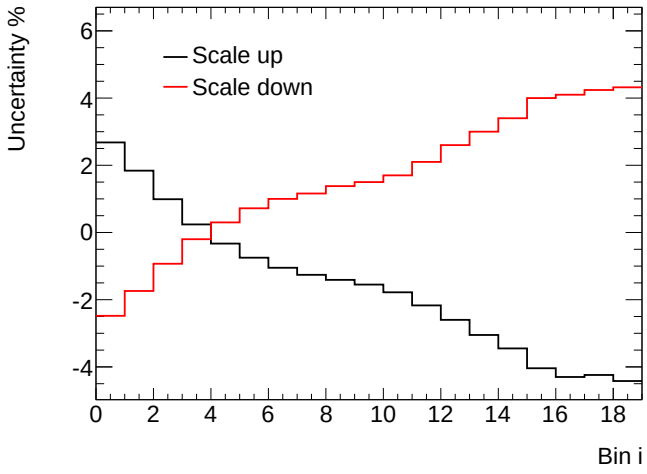

(a)

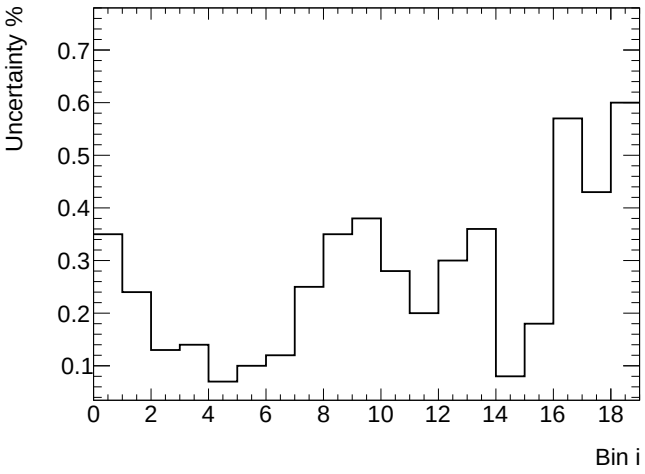

(b)

Figure 8.7: (a) Systematic uncertainties due to (a) the electron energy scale; (b) the electron energy resolution.

electron efficiencies agree as a function of p_T^{ee}.

The data and MC electron identification efficiencies versus p_T^{ee} from the tag-and-probe method are shown in Figure 8.8(a). The difference can not be covered by the systematic uncertainty of 0.5%. This is mainly because the Z boson recoil effect is smeared out when studying the electron efficiency as a function of electron η. Therefore, the remaining difference of the electron efficiency is considered as a systematic uncertainty. The resulting uncertainty is $\approx 0.7\%$ for the first bin and increases to $\approx 1.5\%$ for high p_T^{ee} bins as shown in Figure 8.8(b). Since this uncertainty only accounts for the modeling of a single electron, it has to be multiplied by two. Thus, an uncertainty between 1.4% and 3% is assigned based on fit to the data and MC difference. This is one of the dominant sources of systematic uncertainties.

8.2.5 The Background Estimation

The background estimation ($N^i_{\mathrm{Bkg,j}}$) and its error ($\Delta N^i_{\mathrm{Bkg,j}}$) for each bin i is given in Table 6.3. Instead of propagating the error to the normalized differential cross-section, 100 ensemble tests are made to evaluate the uncertainty due to the background estimation. For each test j, a Gaussian random number `Gaussian(0,1)` is generated and the new background $N^i_{\mathrm{Bkg,j}}$ is calculated as

$$N^i_{\mathrm{Bkg,j}} = N^i_{\mathrm{Bkg}} + \texttt{Gaussian}(0,1) \times \Delta N^i_{\mathrm{Bkg}}. \tag{8.3}$$

Then, the fiducial $\left(\frac{1}{\sigma}\frac{\mathrm{d}\sigma}{\mathrm{d}p_T^Z}\right)_j$ is calculated using $N^i_{\mathrm{Bkg,j}}$ and $\left(\frac{1}{\sigma}\frac{\mathrm{d}\sigma}{\mathrm{d}p_T^Z}\right)_j$ are fit by a Gaussian template whose standard deviation is assigned as the uncertainty due to the background estimation. The resulting uncertainty is less than 0.5% as shown in the Figure 8.9. In this way, the background errors over 19 bins are treated as completely correlated, so that the 0.5% is a conservative estimation.

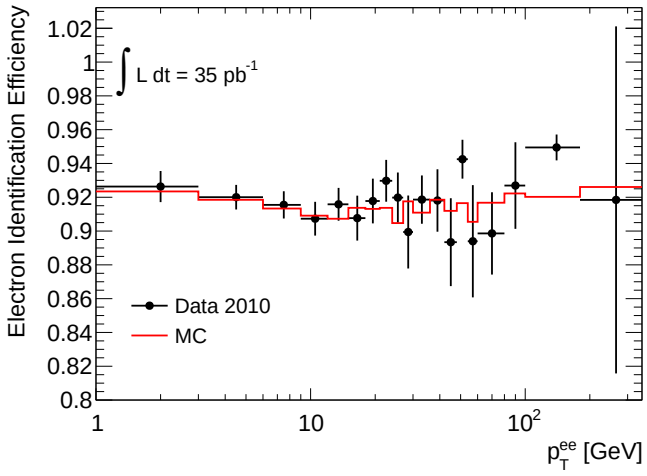

(a)

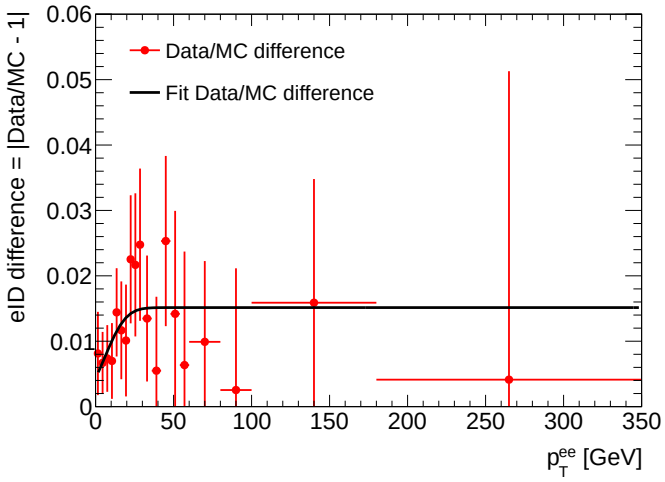

(b)

Figure 8.8: (a) Single medium electron ID efficiency versus the reconstructed p_T^{ee}. (b) Single electron ID uncertainty versus the reconstructed p_T^{ee}. A fit $f(x) = a/2 * (1 + \texttt{Erf}((x-b)/c)) + d$ is used to smooth the uncertainty.

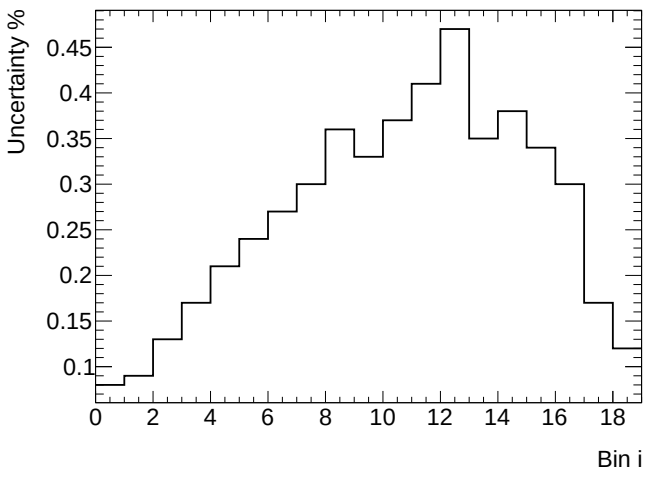

Figure 8.9: Systematic uncertainty due to the background contamination

8.3 Theoretical Systematic Uncertainties

Theoretical systematic uncertainties arise from the bias of the correction factor C, which depends on p_T^Z distributions and MC features, the parton density function (PDF) set used, crack region extrapolation and final state radiation (FSR) effects. They are evaluated by comparing results from different MC simulations and checked by the regularized unfolding method.

8.3.1 The p_T^Z Shape

Since the bin-by-bin unfolding method depends on the correct description of p_T^Z shape (the denominator used to calculate C), the bias of MC p_T^Z shapes has to be taken into account. The default PYTHIA sample, from which central values of C are calculated, is reweighted to another estimate of the true p_T^Z distribution, which is from RESBOS.

PYTHIA is reweighted to RESBOS by $(\log_{10}(p_T^Z), Y^Z)$ in which Z bosons are reconstructed by two electrons before QED FSR. The binning set is 100×50 for $-1.0 < \log_{10}(p_T^Z) < 2.5$ and $-5.0 < Y^Z < 5.0$. PYTHIA and RESBOS are generated with different statistics. Therefore, the reweigting map is the ratio of two normalized

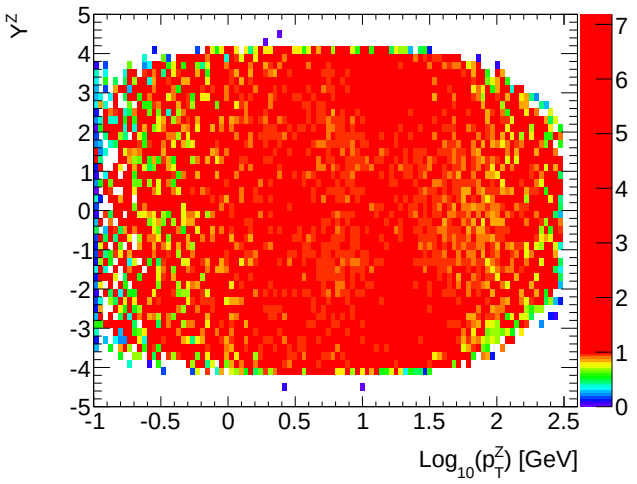

Figure 8.10: The ratio of Born level Z boson distribution from RESBOS to PYTHIA.

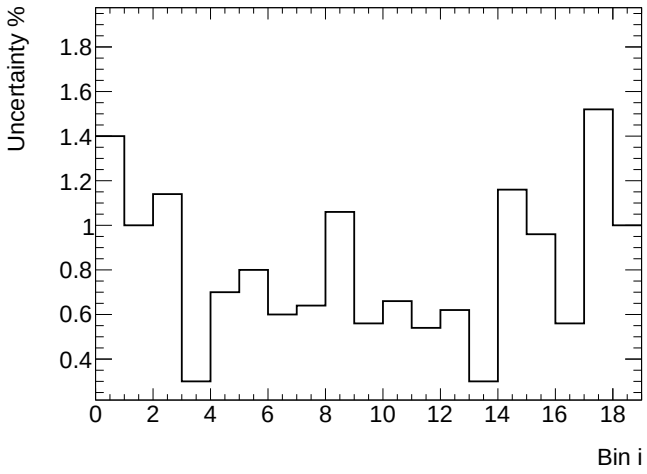

Figure 8.11: Systematic uncertainty due to the p_T^Z shape.

$(\log_{10}(p_T^Z), Y^Z)$ distributions as shown in Figure 8.10.

Then the C factor from the reweighted PYTHIA is used to unfold the data either with the bin-by-bin or the matrix method. The two unfolding $\frac{1}{\sigma}\frac{\mathrm{d}\sigma}{\mathrm{d}p_T^Z}$ are smoothed by 100 bootstrap resamples to eliminate the statistical fluctuation. The unfolding uncertainty due to the p_T^Z shape is shown in Figure 8.11.

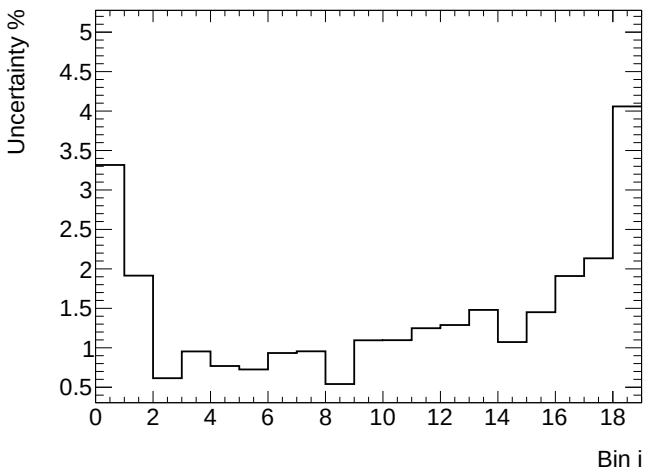

Figure 8.12: Systematic uncertainty due to different MC generator features.

8.3.2 Monte Carlo Features

Apart from the shape dependence of the unfolding procedure, the correction factors may also depend on other generator features, such as the parton shower model. To test the uncertainty associated with these features, correction factors are calculated with both PYTHIA and MC@NLO, where the MC@NLO spectrum is reweighted to PYTHIA to avoid double counting of shape effects. The difference of two spectra that are unfolded with these two sets of correction factors is taken as the systematic uncertainty associated with the generator as shown in Figure 8.12. Shape and generator uncertainties are combined to yield the total unfolding uncertainty, which is then smoothed with a linear function. The resulting uncertainties can be found in Figure 8.12.

8.3.3 The Parton Distribution Function

The default $Z \to ee$ PYTHIA sample is generated using the PDF set of CTEQ6.6. First, it is reweighted to the PDF set of MSTW2008. Then it is also reweighted to 40 eigenvectors PDF sets of MSTW2008 at the 90% confidence level. The maximum deviation of $\frac{1}{\sigma}\frac{\mathrm{d}\sigma}{\mathrm{d}p_T^Z}$ from different reweighting approaches is found to be around 0.1%

over 19 bins. The deviation is small because the fiducial cross-section is in the central region $|\eta| < 2.5$, where uncertainties of PDF sets are small.

A systematic uncertainty of 0.1% is assigned due to the potential bias of the PDF set.

8.3.4 The Crack Region Correction

The phase-space p_T^Z is changed from the reconstruction level ($|\eta^e| < 2.4$ and $|\eta| \notin (1.37, 1.52)$ to the truth level ($|\eta^e| < 2.4$) due to the crack region in the EM calorimeter. The extrapolation of the crack region may cause some bias which is not included in uncertainties of C studied before. This uncertainty is studied by comparing the difference of $\frac{1}{\sigma}\frac{\mathrm{d}\sigma}{\mathrm{d}p_T^Z}$ deviations with and without the crack region extrapolation from Pythia and Mc@nlo samples

$$\text{Uncertainty}^i = \left| \frac{\left(\frac{1}{\sigma}\frac{\mathrm{d}\sigma}{\mathrm{d}p_T^Z}\right)_{\text{crack}}^{\text{Pythia}} - \left(\frac{1}{\sigma}\frac{\mathrm{d}\sigma}{\mathrm{d}p_T^Z}\right)^{\text{Pythia}}}{\left(\frac{1}{\sigma}\frac{\mathrm{d}\sigma}{\mathrm{d}p_T^Z}\right)^{\text{Pythia}}} - \frac{\left(\frac{1}{\sigma}\frac{\mathrm{d}\sigma}{\mathrm{d}p_T^Z}\right)_{\text{crack}}^{\text{Mc@nlo}} - \left(\frac{1}{\sigma}\frac{\mathrm{d}\sigma}{\mathrm{d}p_T^Z}\right)^{\text{Mc@nlo}}}{\left(\frac{1}{\sigma}\frac{\mathrm{d}\sigma}{\mathrm{d}p_T^Z}\right)^{\text{Mc@nlo}}} \right|^i \tag{8.4}$$

where for ith bin

- $\left(\frac{1}{\sigma}\frac{\mathrm{d}\sigma}{\mathrm{d}p_T^Z}\right)_{\text{crack}}^{\text{Pythia}}$, Pythia result with $|\eta^e| < 2.4$ and $|\eta| \notin (1.37, 1.52)$ at the truth level;
- $\left(\frac{1}{\sigma}\frac{\mathrm{d}\sigma}{\mathrm{d}p_T^Z}\right)^{\text{Pythia}}$, Pythia result with $|\eta^e| < 2.4$ at the truth level;
- $\left(\frac{1}{\sigma}\frac{\mathrm{d}\sigma}{\mathrm{d}p_T^Z}\right)_{\text{crack}}^{\text{Mc@nlo}}$, Mc@nlo result with $|\eta^e| < 2.4$ and $|\eta| \notin (1.37, 1.52)$ at the truth level;
- $\left(\frac{1}{\sigma}\frac{\mathrm{d}\sigma}{\mathrm{d}p_T^Z}\right)^{\text{Pythia}}$, Mc@nlo result with $|\eta^e| < 2.4$ at the truth level.

A maximum deviation of 0.3% is found over 19 bins, which is used as the systematic uncertainty of the crack region correction.

8.3.5 The Final State Radiation

FSR uncertainties from single electron consist of

- different approximations used in PHOTOS [40] to calculate the FSR matrix element $\approx 0.1\%$;
- simulations of the interaction of the radiated photons with detector materials ≈ 0.2 [41] .

Therefore, a conservative uncertainty of 0.6% $(= (0.2\% + 0.1\%) \times 2)$ is assigned to $\frac{1}{\sigma}\frac{\mathrm{d}\sigma}{\mathrm{d}p_T^Z}$ for the potential bias caused by the FSR mis-modeling of two electrons.

8.4 Summary of Uncertainties

Figure 8.13(a) and 8.13(b) show the normalized fiducial cross-section p_T^{ee} spectrum from the bin-by-bin unfolding method and all the uncertainties for each bin are summarized in Table 8.3. The analysis is systematically limited up to about 9 GeV. The systematic errors are of similar order of magnitude as the statistical ones over the entire p_T^Z range. The dominant contributions are due to the energy scale and electron identification efficiency.

	Bin-by-bin			Matrix			Rel. diff.
p_{T}	$\frac{1}{\sigma^Z}\frac{d\sigma^Z}{dp_T^Z}$	Stat.	Syst.	$\frac{1}{\sigma^Z}\frac{d\sigma^Z}{dp_T^Z}$	Stat.	Syst.	
(GeV)	(1/ GeV)	(%)	(%)	(1/ GeV)	(%)	(%)	(%)
0 − 3	0.0348	3.4	4.1	0.0347	4.9	4.2	-0.35
3 − 6	0.0586	2.6	2.5	0.0597	4.1	2.6	1.76
6 − 9	0.0462	2.8	2.5	0.0463	4.9	2.8	0.32
9 − 12	0.0343	3.2	2.1	0.0330	6.0	2.1	-4.00
12 − 15	0.0293	3.5	3.0	0.0317	5.7	3.1	7.66
15 − 18	0.0204	4.1	2.7	0.0196	7.9	2.8	-4.24
18 − 21	0.0164	4.6	3.8	0.0172	8.1	4.2	4.42
21 − 24	0.0132	5.2	3.9	0.0119	10.3	4.1	-10.13
24 − 27	0.0108	5.8	5.5	0.0110	10.3	6.2	2.36
27 − 30	0.0102	6.0	3.7	0.0102	10.1	4.0	0.39
30 − 36	0.0072	5.0	4.3	0.0070	7.1	4.6	-3.67
36 − 42	0.0049	6.1	3.8	0.0049	8.3	4.3	0.16
42 − 48	0.0036	7.0	5.2	0.0036	9.8	5.5	-2.33
48 − 54	0.0033	7.5	5.2	0.0032	10.0	6.0	-2.26
54 − 60	0.0021	9.2	6.3	0.0021	12.7	7.0	-3.79
60 − 80	$1.2 \cdot 10^{-3}$	6.7	5.3	$1.1 \cdot 10^{-3}$	7.9	5.3	-6.12
80 −100	$5.7 \cdot 10^{-4}$	9.7	6.1	$5.8 \cdot 10^{-4}$	11.1	6.9	1.52
100−180	$1.7 \cdot 10^{-4}$	8.7	6.9	$1.8 \cdot 10^{-4}$	9.3	7.3	1.02
180−350	$7.8 \cdot 10^{-6}$	28.7	7.5	$9.8 \cdot 10^{-6}$	29.7	7.5	20.42

Table 8.2: The normalized p_T^Z distribution in the fiducial volume from the bin-by-bin and the regularized matrix unfolding method. The larger statistical uncertainties assigned to the matrix method result from the regularization. Within systematic errors and the additional statistical error, the results agree.

p_T^{ee}	$\frac{1}{\sigma}\frac{d\sigma}{dp_T^Z}$	stat.	syst.	Energy scale	reso.	eID	OTX	Pileup	unfold	MC stat.	FSR	Crack	PDF	Bkg.
(GeV)	(1/GeV)	(%)	(%)	(%)	(%)	(%)	(%)	(%)	(%)	(%)	(%)	(%)	(%)	(%)
0 – 3	0.0348	3.28	4.72	2.68	0.50	0.99	0.10	0.33	3.60	0.53	0.60	0.30	0.10	0.26
3 – 6	0.0585	2.41	3.25	1.84	0.50	1.25	0.10	0.33	2.16	0.37	0.60	0.30	0.10	0.29
6 – 9	0.0461	2.66	2.31	0.99	0.50	1.54	0.10	0.33	0.96	0.48	0.60	0.30	0.10	0.42
9 – 12	0.0343	3.07	2.33	0.24	0.50	1.82	0.10	0.33	1.00	0.50	0.60	0.30	0.10	0.55
12 – 15	0.0293	3.34	2.61	-0.33	0.50	2.10	0.10	0.33	1.04	0.60	0.60	0.30	0.10	0.65
15 – 18	0.0204	3.92	2.93	-0.75	0.50	2.35	0.10	0.33	1.08	0.70	0.60	0.30	0.10	0.77
18 – 21	0.0164	4.39	3.23	-1.05	0.50	2.57	0.10	0.33	1.11	0.82	0.60	0.30	0.10	0.84
21 – 24	0.0132	4.79	3.45	-1.26	0.50	2.75	0.10	0.33	1.15	0.79	0.60	0.30	0.10	0.92
24 – 27	0.0108	5.52	3.66	-1.41	0.50	2.90	0.10	0.33	1.19	0.87	0.60	0.30	0.10	1.10
27 – 30	0.0102	6.48	3.89	-1.55	0.50	3.01	0.10	0.33	1.23	1.15	0.60	0.30	0.10	1.00
30 – 36	0.0072	4.85	4.01	-1.78	0.50	3.11	0.10	0.33	1.28	0.88	0.60	0.30	0.10	1.15
36 – 42	0.0049	5.76	4.28	-2.17	0.50	3.18	0.10	0.33	1.36	0.92	0.60	0.30	0.10	1.24
42 – 48	0.0037	7.01	4.59	-2.60	0.50	3.21	0.10	0.33	1.43	1.06	0.60	0.30	0.10	1.39
48 – 54	0.0033	7.76	4.92	-3.05	0.50	3.21	0.10	0.33	1.51	1.25	0.60	0.30	0.10	1.04
54 – 60	0.0021	9.16	5.27	-3.45	0.50	3.21	0.10	0.33	1.58	1.48	0.60	0.30	0.10	1.11
60 – 80	$1.2 \cdot 10^{-3}$	6.5	5.6	-4.04	0.50	3.22	0.10	0.33	1.74	0.90	0.60	0.30	0.10	0.95
80 –100	$5.7 \cdot 10^{-4}$	9.8	5.9	-4.30	0.50	3.22	0.10	0.33	1.99	1.16	0.60	0.30	0.10	0.61
100–180	$1.7 \cdot 10^{-4}$	9.6	6.1	-4.24	0.50	3.22	0.10	0.33	2.62	1.19	0.60	0.30	0.10	0.21
180–350	$7.8 \cdot 10^{-6}$	27.0	7.8	-4.42	0.50	3.22	0.10	0.33	4.18	3.60	0.60	0.30	0.10	0.12

Table 8.3: Summary of the normalized p_T^Z distribution in the fiducial region.

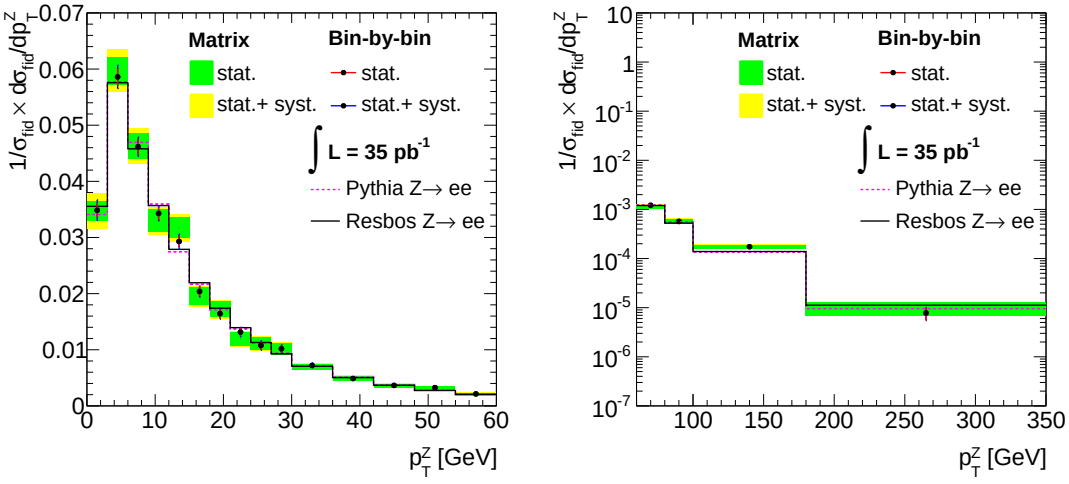

(a) (b)

Figure 8.13: Normalized p_T^Z distribution in the fiducial volume: (a) $0 < p_T^Z < 60$ GeV (b) and $60 < p_T^Z < 350$ GeV.

CHAPTER IX

Summary

The p_T^Z spectrum, $\frac{1}{\sigma}\frac{\mathrm{d}\sigma}{\mathrm{d}p_T^Z}$ is measured in the fiducial volume from the $Z \to ee$ decays which shows an agreement with the prediction from the PYTHIA generator. In addition to PYTHIA and MC@NLO, various generators of pQCD calculations predict the fiducial $\frac{1}{\sigma}\frac{\mathrm{d}\sigma}{\mathrm{d}p_T^Z}$ as introduced in Section 2.7.

FEWZ provides the fiducial $\frac{1}{\sigma}\frac{\mathrm{d}\sigma}{\mathrm{d}p_T^Z}$ using fixed order pQCD calculations up to the NNLO ($\mathcal{O}(\alpha_s^2)$), as well as the NLO ($\mathcal{O}(\alpha_s)$) with MSTW2008 PDF sets. The theoretical uncertainties of FEWZ predictions are estimated by

- Varying the renormalization and factorization scales around the nominal value ($\mu_R = \mu_F = M_Z$) with the constraint $0.5 < \mu_R/\mu_F < 2$;
- Varying the α_s within the range of 90% confidence level [12];
- Using the PDF eigenvectors sets at 90% confidence level.

The total theoretical uncertainty is $\approx 10\%$ and $\approx 8\%$ for the $\mathcal{O}(\alpha_s)$ and $\mathcal{O}(\alpha_s^2)$ predictions, respectively. The higher order correction is non-negligible for the p_T^Z distribution as indicated by substantial scale uncertainties. For $p_T^Z > 18$ GeV, the pQCD prediction receives a correction of $26-36\%$ from the NLO to the NNLO. With the higher order correction, the p_T^Z distribution measured from data still overshoots the NNLO prediction by $\approx 10\%$ which is covered by the scale uncertainties. This

deficit is observed at the Tevatron [42, 43] as well with a larger difference $15-20\%$. For $p_T^Z < 15$ GeV where the fixed order pQCD calculation is not adequate to describe the correct p_T^Z distribution, the discrepancy between data and FEWZ increases rapidly towards vanishing p_T^Z.

The measurement is also compared to NLO generators such as RESBOS and POWHEG. The RESBOS prediction combines resummed and fixed order pQCD calculations, while POWHEG has only fixed order pQCD calculation and is interfaced with HERWIG for the parton shower and fragmentation. Therefore, RESBOS prediction shows a better agreement with data than the POWHEG. However, the RESBOS prediction is slightly higher than the data for $10 < p_T^Z < 40$ GeV, and slightly lower for $p_T^Z > 40$ GeV. FEWZ and RESBOS use different PDF sets and it is verified that the difference caused by the PDF uncertainty is below 3% [44].

ALPGEN and SHERPA are the LO generators which are able to simulate the weak boson productions associated with up to five additional hard partons. The number of additional partons can be specified in the simulation. Therefore, they are able to provide a good description of $\frac{1}{\sigma}\frac{\mathrm{d}\sigma}{\mathrm{d}p_T^Z}$ in the high p_T^Z region with large statistics. The enhancement of the $\mathcal{O}(\alpha_s^2)$ calculation is included in the process of multiple parton radiations [17]. HERWIG is used for the parton shower and fragmentation and JIMMY is used for the underlying event simulations in ALPGEN and SHERPA. Over the whole p_T^Z region, ALPGEN and SHERPA predictions agree with the measurement from data very well. The fiducial $\frac{1}{\sigma}\frac{\mathrm{d}\sigma}{\mathrm{d}p_T^Z}$ of the data and various generators are summarized in Table 9.1. All the results are divided by the RESBOS prediction and the ratios are shown in Figure 9.1.

The fiducial $\frac{1}{\sigma}\frac{\mathrm{d}\sigma}{\mathrm{d}p_T^Z}$ is also measured in $Z \to \mu\mu$ decays using the similar strategies as the electron channel [44]. The corresponding integrated luminosity of $Z \to \mu\mu$ events is 40 pb^{-1}. The ratio of the fiducial $\frac{1}{\sigma}\frac{\mathrm{d}\sigma}{\mathrm{d}p_T^Z}$ between electron and muon channels is shown in Figure 9.2.

p_T^{ee} (GeV)	Data $\frac{1}{\sigma}\frac{d\sigma}{dp_T^Z}$ (1/GeV)	Data stat. (%)	Data syst. (%)	RESBOS $\frac{1}{\sigma}\frac{d\sigma}{dp_T^Z}$ (1/GeV)	FEWZ $\frac{1}{\sigma}\frac{d\sigma}{dp_T^Z}$ (1/GeV)	PYTHIA $\frac{1}{\sigma}\frac{d\sigma}{dp_T^Z}$ (1/GeV)	MC@NLO $\frac{1}{\sigma}\frac{d\sigma}{dp_T^Z}$ (1/GeV)	ALPGEN $\frac{1}{\sigma}\frac{d\sigma}{dp_T^Z}$ (1/GeV)	SHERPA $\frac{1}{\sigma}\frac{d\sigma}{dp_T^Z}$ (1/GeV)	POWHEG $\frac{1}{\sigma}\frac{d\sigma}{dp_T^Z}$ (1/GeV)
1 – 3	0.0348	3.28	4.72	0.0367	-	0.0341	0.0393	0.0352	0.0370	0.0298
3 – 6	0.0585	2.41	3.25	0.0591	-	0.0578	0.0599	0.0586	0.0622	0.0617
6 – 9	0.0461	2.66	2.31	0.0464	-	0.0469	0.0485	0.0488	0.0493	0.0530
9 – 12	0.0343	3.07	2.33	0.0359	0.0392	0.0359	0.0367	0.0372	0.0357	0.0393
12 – 15	0.0293	3.34	2.61	0.0280	0.0271	0.0275	0.0280	0.0284	0.0269	0.0291
15 – 18	0.0204	3.92	2.93	0.0219	0.0204	0.0216	0.0213	0.0219	0.0209	0.0221
18 – 21	0.0164	4.39	3.23	0.0174	0.0154	0.0171	0.0168	0.0171	0.0163	0.0170
21 – 24	0.0132	4.79	3.45	0.0139	0.0123	0.0137	0.0132	0.0133	0.0129	0.0134
24 – 27	0.0108	5.52	3.66	0.0112	0.0098	0.0112	0.0107	0.0106	0.0104	0.0109
27 – 30	0.0102	6.48	3.89	0.0092	0.0080	0.0094	0.0087	0.0085	0.0085	0.0091
30 – 36	0.0072	4.85	4.01	0.0070	0.0062	0.0071	0.0065	0.0064	0.0066	0.0068
36 – 42	0.0049	5.76	4.28	0.0049	0.0044	0.0052	0.0046	0.0045	0.0048	0.0047
42 – 48	0.0037	7.01	4.59	0.0035	0.0033	0.0037	0.0033	0.0034	0.0035	0.0034
48 – 54	0.0033	7.76	4.92	0.0026	0.0025	0.0029	0.0025	0.0026	0.0026	0.0025
54 – 60	0.0021	9.16	5.27	0.0019	0.0019	0.0021	0.0018	0.0020	0.0020	0.0019
60 – 80	$1.2 \cdot 10^{-3}$	6.5	5.6	$1.1 \cdot 10^{-3}$	$1.1 \cdot 10^{-3}$	$1.2 \cdot 10^{-3}$	$1.1 \cdot 10^{-3}$	$1.2 \cdot 10^{-3}$	$1.2 \cdot 10^{-3}$	$1.1 \cdot 10^{-3}$
80 –100	$5.7 \cdot 10^{-4}$	9.8	5.9	$4.7 \cdot 10^{-4}$	$5.1 \cdot 10^{-4}$	$5.6 \cdot 10^{-4}$	$4.2 \cdot 10^{-4}$	$5.4 \cdot 10^{-4}$	$5.2 \cdot 10^{-4}$	$4.6 \cdot 10^{-4}$
100–180	$1.7 \cdot 10^{-4}$	9.6	6.1	$1.1 \cdot 10^{-4}$	$1.3 \cdot 10^{-4}$	$1.4 \cdot 10^{-4}$	$0.9 \cdot 10^{-4}$	$1.4 \cdot 10^{-4}$	$1.2 \cdot 10^{-4}$	$1.0 \cdot 10^{-4}$
180–350	$7.8 \cdot 10^{-6}$	27.0	7.8	$7.3 \cdot 10^{-6}$	$10.8 \cdot 10^{-6}$	$9.5 \cdot 10^{-6}$	$6.4 \cdot 10^{-6}$	$11.6 \cdot 10^{-6}$	$6.2 \cdot 10^{-6}$	$5.7 \cdot 10^{-6}$

Table 9.1: Summary of the fiducial $\frac{1}{\sigma}\frac{d\sigma}{dp_T^Z}$ measured from the data and predicted by various MC generators. The FEWZ prediction is from the NNLO calculation and the first three bins are omitted due to the divergence of the pQCD calculation.

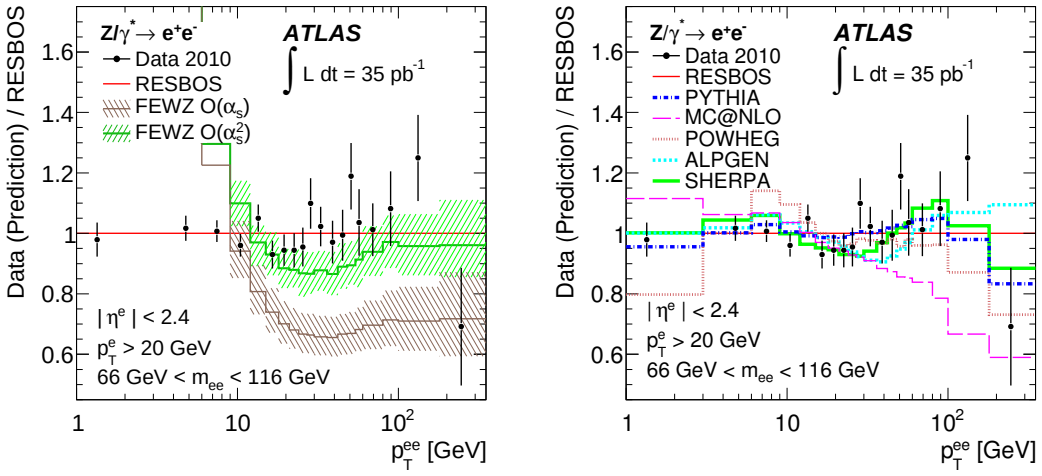

(a) (b)

Figure 9.1: Ratios of the measured fiducial $\frac{1}{\sigma}\frac{d\sigma}{dp_T^Z}$ and various predictions from $Z \to ee$ decays. (a) FEWZ predictions are shown with combined scale, α_s and PDF uncertainties; (b) the fiducial $\frac{1}{\sigma}\frac{d\sigma}{dp_T^Z}$ ratios of the data and various generators to the RESBOS. The data uncertainties are calculated by summing statistical and systematic uncertainties in quadrature. In the low p_T^Z region, the fixed order pQCD calculations from FEWZ diverge and are omitted.

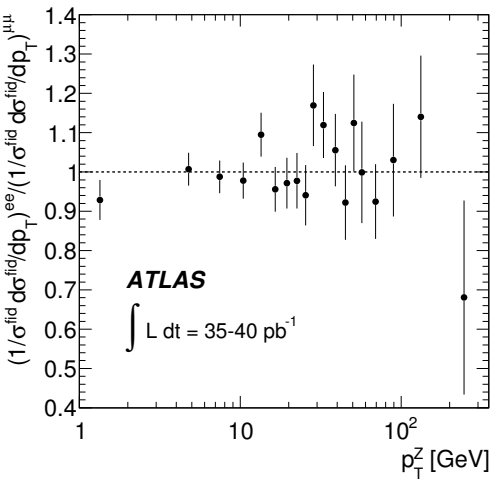

Figure 9.2: Ratio of the fiducial $\frac{1}{\sigma}\frac{\mathrm{d}\sigma}{\mathrm{d}p_T^Z}$ from $Z \to ee$ and $Z \to \mu\mu$ decays. The error bars include both statistical and systematic uncertainties. The systematic uncertainties due to the unfolding procedure and QED FSR are omitted.

The measured results from two channels are combined using a χ^2 minimization method which takes into account correlated systematic uncertainties [45]. The minimization yields a $\chi^2/\text{d.o.f.} = 17.0/19$ which indicates a good compatibility of electron and muon fiducial $\frac{1}{\sigma}\frac{\mathrm{d}\sigma}{\mathrm{d}p_T^Z}$. The combined fiducial $\frac{1}{\sigma}\frac{\mathrm{d}\sigma}{\mathrm{d}p_T^Z}$ of $Z \to \ell\ell$ ($\ell = e, \mu$) are shown in Figure 9.3.

In summary, this thesis measures the normalized transverse momentum spectrum $\frac{1}{\sigma}\frac{\mathrm{d}\sigma}{\mathrm{d}p_T^Z}$ in the fiducial volume of the ATLAS detector from $Z \to ee$ decays up to $p_T^Z = 350$ GeV produced in proton-proton collisions at $\sqrt{s} = 7$ TeV. The measured results are compared to predictions of various generators. RESBOS describes the $\frac{1}{\sigma}\frac{\mathrm{d}\sigma}{\mathrm{d}p_T^Z}$ well in the whole p_T^Z range. For $p_T^Z > 18$ GeV, FEWZ $\mathcal{O}(\alpha_s^2)$ prediction underestimates the $\frac{1}{\sigma}\frac{\mathrm{d}\sigma}{\mathrm{d}p_T^Z}$ by about 10%. Predictions from PYTHIA, ALPGEN and SHERPA are in good agreement with measurements from data. The $\frac{1}{\sigma}\frac{\mathrm{d}\sigma}{\mathrm{d}p_T^Z}$ from the electron decay channel is cross-checked with that from the muon decay channel and a very good compatibility is found. For $p_T^Z > 9$ GeV, the measurement is limited by statistical uncertainties rather than systematic uncertainties, which is expected to be improved with increasing luminosity.

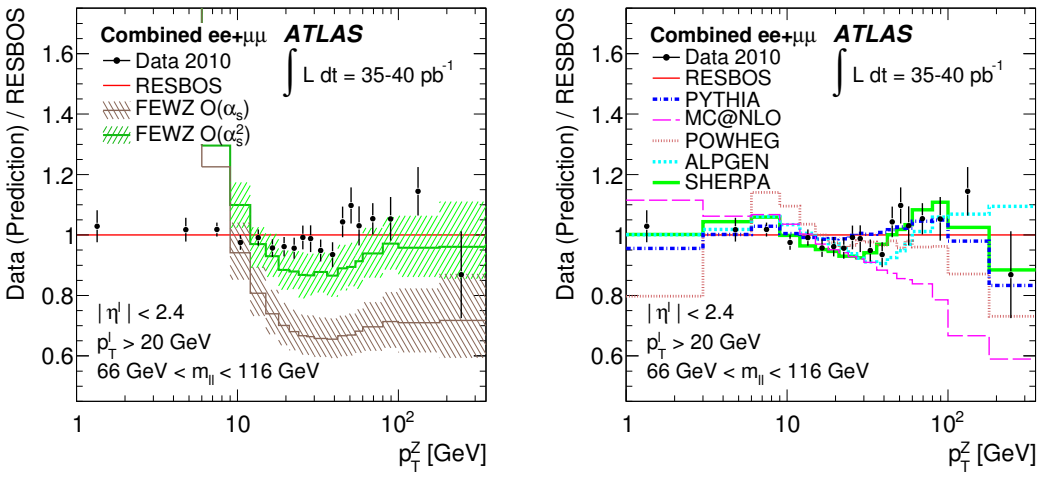

(a) (b)

Figure 9.3: Ratios of the measured fiducial $\frac{1}{\sigma}\frac{\mathrm{d}\sigma}{\mathrm{d}p_T^Z}$ and various predictions from $Z \to \ell\ell$ ($\ell = e, \mu$) decays. (a) FEWZ predictions are shown with combined scale, α_s and PDF uncertainties; (b) the fiducial $\frac{1}{\sigma}\frac{\mathrm{d}\sigma}{\mathrm{d}p_T^Z}$ ratios of the data and various generators to the RESBOS. The data are shown with combined statistical and systematic uncertainties. In the low p_T^Z region, the fixed order pQCD calculations from FEWZ diverge and are omitted.

BIBLIOGRAPHY

BIBLIOGRAPHY

[1] Pavel M. Nadolsky et al. Implications of CTEQ global analysis for collider observables. *Phys. Rev.*, D78:013004, 2008.

[2] ATLAS Collaboration. Double differential z,w cross sections and their ratios in the electron channels. Technical Report ATLAS-COM-2010-325, CERN, Geneva, Jun 2010.

[3] ATLAS Collaboration. Determination of the muon reconstruction efficiency in ATLAS at the Z resonance in proton-proton collisons at $\sqrt{s} = 7$ TeV. Technical Report ATLAS-CONF-2011-008, CERN, Geneva, Feb 2011.

[4] Peter Brockway Arnold and M. Hall Reno. The Complete Computation of High p(t) W and Z Production in 2nd Order QCD. *Nucl. Phys.*, B319:37, 1989.

[5] Richard J. Gonsalves, Jerzy Pawlowski, and Chung-Fai Wai. QCD radiative corrections to electroweak boson production at large transverse momentum in hadron collisions. *Phys. Rev.*, D40:2245, 1989.

[6] Victor Mukhamedovich Abazov et al. Measurement of the W boson mass. *Phys. Rev. Lett.*, 103:141801, 2009.

[7] K. Nakamura et al. (Particle Data Group). 2011 review of particle physics. *J. Phys.*, G 37:075021, Jan 2011.

[8] Gordon Kane. *Modern Elementary Particle Physics : The Fundamental Particles and Forces*. Addison-Wesley, updated edition, 1993.

[9] Mark Allen Srednicki. *Quantum Field Theory*. illustrated, reprint edition, 2007.

[10] R. Friedberg N. H. Christ and T. D. Lee. Random lattice field theory: General formulation. *Nuclear Physics B*, 202:89–125, Jul 1982.

[11] Georges Aad et al. Measurement of the $W \to \ell\nu$ and $Z/\gamma^* \to \ell\ell$ production cross sections in proton-proton collisions at $\sqrt{s} = 7$ TeV with the ATLAS detector. *JHEP*, 12:060, 2010.

[12] Kirill Melnikov and Frank Petriello. Electroweak gauge boson production at hadron colliders through $O(\alpha_s^2)$. *Phys. Rev.*, D74:114017, 2006.

[13] Georges Aad et al. Charged-particle multiplicities in pp interactions measured with the ATLAS detector at the LHC. *New J. Phys.*, 13:053033, 2011.

[14] Giuseppe Bozzi, Stefano Catani, Giancarlo Ferrera, Daniel de Florian, and Massimiliano Grazzini. Production of Drell–Yan lepton pairs in hadron collisions: transverse-momentum resummation at next-to- next-to-leading logarithmic accuracy. *Phys. Lett.*, B696:207, 2011.

[15] Stefano Frixione and Bryan R. Webber. Matching NLO QCD computations and parton shower simulations. *JHEP*, 06:029, 2002.

[16] R Jones and D Barberis. The atlas computing model. *J. Phys.: Conf. Ser*, 2008.

[17] Michelangelo L. Mangano, Mauro Moretti, Fulvio Piccinini, Roberto Pittau, and Antonio D. Polosa. ALPGEN, a generator for hard multiparton processes in hadronic collisions. *JHEP*, 07:001, 2003.

[18] T. Gleisberg et al. Event generation with SHERPA 1.1. *JHEP*, 02:007, 2009.

[19] Stefano Frixione, Paolo Nason, and Carlo Oleari. Matching NLO QCD computations with Parton Shower simulations: the POWHEG method. *JHEP*, 11:070, 2007.

[20] G. A. Ladinsky and C. P. Yuan. The Nonperturbative regime in QCD resummation for gauge boson production at hadron colliders. *Phys. Rev.*, D50:4239, 1994.

[21] Ryan Gavin, Ye Li, Frank Petriello, and Seth Quackenbush. FEWZ 2.0: A code for hadronic Z production at next-to- next-to-leading order. 2010.

[22] A. Sherstnev and R. S. Thorne. Parton Distributions for LO Generators. *Eur. Phys. J.*, C55:553, 2008.

[23] J. Pumplin et al. New generation of parton distributions with uncertainties from global QCD analysis. *JHEP*, 07:012, 2002.

[24] G. Corcella et al. HERWIG 6.5: an event generator for Hadron Emission Reactions With Interfering Gluons. *JHEP*, 0101:010, 2001.

[25] ATLAS Collaboration. First tuning of HERWIG/JIMMY to ATLAS data. *ATL-PHYS-PUB-2010-014*, 2010. http://cdsweb.cern.ch/record/1303025/files/ATL-PHYS-PUB-2010-014.pdf.

[26] G. Aad et al. The ATLAS Experiment at the CERN Large Hadron Collider. *JINST*, 3:S08003, 2008.

[27] M. Dittmar, F. Pauss, and D. Zürcher. Towards a precise parton luminosity determination at the cern lhc. *Phys. Rev. D*, 56(11):7284–7290, Dec 1997.

[28] Donald H. Perkins. *Introduction to High Energy Physics*. Addison-Wesley Publishing Company, Inc., third edition edition, 1986.

[29] J C Armitage1 *et.al.* Electron signals in the forward calorimeter prototype for atlas. *JINST*, 2, 2007.

[30] G. Aad et al. Expected Performance of the ATLAS Experiment - Detector, Trigger and Physics. 2009.

[31] G. Valencia S. Willenbrock1. On the definition of the z-boson mass. *Physics Letters B*, 259:376–376, 1991.

[32] ATLAS Collaboration. Expected electron performance in the atlas experiment. Technical Report ATLAS-CONF-2011-006, CERN, Geneva, Apr 2011.

[33] ATLAS Collaboration. Updated Luminosity Determination in pp Collisions at root(s)=7 TeV using the ATLAS Detector. Technical Report ATLAS-CONF-2011-011, CERN, Geneva, Mar 2011.

[34] S. Agostinelli et al. GEANT4: A simulation toolkit. *Nucl. Instrum. Meth.*, A506:250, 2003.

[35] ATLAS Collaboration. Observation of inclusive electrons in the ATLAS experiment at $\sqrt{s} = 7$ TeV. Technical Report ATLAS-CONF-2010-073, CERN, Geneva, Jul 2010.

[36] Volker Blobel. An unfolding method for high energy physics experiments, contribution to the conference on adcanced statistical techniques in particle physics. `arXiv:hep-ex/0208022v1`, Aug 2002.

[37] K Kunisch H W Engl and A Neubauer. Convergence rates for tikhonov regularisation of non-linear ill-posed problems. *Inverse Problems*, 5, Aug 1989.

[38] Tim Adye. Unfolding algorithms and tests using roounfold. `arXiv:1105.1160v1`, May 2011.

[39] B. Efron. Bootstrap Methods: Another Look at the Jackknife. *The Annals of Statistics*, Vol. 7, No.1:1, 1979.

[40] Piotr Golonka and Zbigniew Was. PHOTOS Monte Carlo: A Precision tool for QED corrections in Z and W decays. *Eur. Phys. J.*, C45:97, 2006.

[41] S. Jadach, B. F. L. Ward, and Z. Was. Coherent exclusive exponentiation for precision Monte Carlo calculations. *Phys. Rev.*, D63:113009, 2001.

[42] B. Abbott et al. Differential production cross-section of Z bosons as a function of transverse momentum at $\sqrt{s} = 1.8$ TeV. *Phys. Rev. Lett.*, 84:2792, 2000.

[43] V.M. Abazov et al. Measurement of the shape of the boson transverse momentum distribution in $p\bar{p}$ $Z/\gamma^* \to e^+e^-$+ X events produced at $\sqrt{s}$ = 1.96 TeV. *Phys. Rev. Lett.*, 100:102002, 2008.

[44] ATLAS Collaboration. A first measurement of the transverse momentum distribution of drell-yan lepton pairs at $\sqrt{(}s) = 7$ tev with atlas. Technical Report ATLAS-CONF-2011-233, CERN, Geneva, Mar 2011.

[45] F.D. Aaron et al. Measurement of the Inclusive ep Scattering Cross Section at Low Q^2 and x at HERA. *Eur. Phys. J.*, C63:625, 2009.